



Cyprus
University of
Technology

Faculty of Engineering
and Technology

Doctoral Dissertation

**NONLINEAR STRUCTURAL STABILITY
OF FUNCTIONALLY OPTIMIZED
SANDWICH STRUCTURES**

by

Christodoulos Georgiou

Limassol 2022

CYPRUS UNIVERSITY OF TECHNOLOGY
FACULTY OF ENGINEERING AND TECHNOLOGY
DEPARTMENT OF CIVIL ENGINEERING AND GEOMATICS

**NONLINEAR STRUCTURAL STABILITY
OF FUNCTIONALLY OPTIMIZED
SANDWICH STRUCTURES**

by

Christodoulos Georgiou

Limassol, 2022

REQUEST FOR APPROVAL

Doctor of Philosophy Dissertation

**NONLINEAR STRUCTURAL STABILITY
OF FUNCTIONALLY OPTIMIZED
SANDWICH STRUCTURES**

Presented by

Christodoulos Georgiou

Supervisor: Dr. Stylianos Yiatros, Associate Professor

Cyprus University of Technology

Signature:

Member of the committee: Dr. Athanasios Kolios, Professor

University of Strathclyde

Signature:

Member of the committee: Dr. Elia Tantele, Associate Professor

Cyprus University of Technology

Signature:

Cyprus University of Technology

April, 2022

Copyright

Copyright ©2022 of dissertation submission Christodoulos Georgiou

All rights reserved.

The approval of Doctoral Dissertation by the DEPARTMENT OF CIVIL ENGINEERING AND GEOMATICS does not imply necessarily the approval by the Department of views of the writer.

*To my wife Maria-Flora
and to my daughter Elisavet.*

Acknowledgments

Looking back at this work, I have become indebted to so many intelligent, patient and encouraging people who have helped me complete this thesis. Firstly, I would like to thank my PhD project supervisor Dr. Stylianos Yiatros, he has always offered me invaluable and guidance, both during undergraduate studies and through my PhD. I have always had the greatest respect for Stelios as an exceptional scientist and it has been a pleasure to work with him. Without his help, encouragement and guidance all these years, this thesis could have never been realized.

Finally, I wish to dedicate this thesis to the people who have been closest to me and without their continuous support in so many ways, the completion of this work would have been impossible. To my parents, whose sacrifices and continuous support gave up me the opportunity to pursue my dreams. Finally, to my wife, Maria-Flora, who has been by my side, living every single minute of it. Your love, support, understanding, patience, and all the sacrifices you went through for me through this PhD study are invaluable.

Abstract

Sandwich structures are an efficient form of construction but can suffer from nonlinear interaction phenomena that can erode their load carrying capacity. This interaction is triggered at a secondary bifurcation point and is manifested as a localized deformation wave in the most compressed face plate which destabilizes and drastically reduces its load carrying capacity. The current work advances some recent analytical work on mode interaction and localization in sandwich struts by extending and developing the model for different geometries and material parametric design.

In the first part, a nonlinear analytical model for investigating localized interactive buckling in simply supported, thin-face plate sandwich struts with weak cores, is extended to account for local deformations in both face plates, which have been observed in experiments and finite element simulations. The original model is based on the total potential energy principles with large displacement assumptions. It assumes Timoshenko shear deformable theory for the core and approximates the overall mode as a half-sine wave along the length of the strut while the local face plate displacements are initially unknown and are found as solutions of the governing equations. The extended model is able to capture measurable local face plate displacements in the less compressed face plate, beyond the secondary bifurcation which leads to localized interactive buckling, for the case where overall buckling is critical. Moreover, the allowance of local displacements in both face plates allows the extended model to predict the postbuckling behavior better in cases where local buckling is critical. The results from this model compare very well with nonlinear finite

element simulations with respect to both the equilibrium paths and panel deformations.

In the second part, two analytical model for interactive buckling in sandwich struts with cores made from a functionally graded material based on the total potential energy principles are presented. Each model is derived from a different shear deformation theory, namely Timoshenko Beam Theory (TBT) and Reddy-Bickford Theory (RBT). Parametric results from the analytical models are compared with geometrically nonlinear simulations using ANSYS general purpose finite element package. Good agreement is found, and this offers encouragement for more elaborate models to be devised that can account for face-core interface delamination, an area where functionally graded materials could offer mitigating design solutions.

Keywords - Mode interaction, Sandwich struts, Variational formulation, Interactive buckling, Postbuckling, Functionally graded material

Contents

Acknowledgements	ix
Abstract	x
List of Figures	xvii
List of Tables	xxv
Nomenclature	xxvii
1 Introduction	1
1.1 Buckling theory	4
1.1.1 Linear Buckling	4
1.1.2 Nonlinear buckling	7
1.1.3 Interactive buckling phenomena	11
1.1.4 Localization of buckling pattern due to interactive buckling	15
1.2 Outline of thesis	15
1.2.1 Sandwich structures applications and theory	15
1.2.2 Modelling localized buckling in sandwich struts with in-	
homogeneous deformations in both face plates	17
1.2.3 Modelling interactive buckling for FGM sandwich struts	18
1.2.4 Comparison of analytical models with finite element sim-	
ulations	18
1.2.5 Conclusions and future work	18

2	Sandwich structures applications and theory	19
2.1	Applications	19
2.2	Materials	23
2.2.1	Face plate materials	24
2.2.2	Sandwich core materials	24
2.3	Sandwich structures literature	27
2.4	Analytical modelling of sandwich struts	30
2.4.1	Critical load for overall buckling	30
2.4.2	Overall buckling	31
2.4.3	Bending theories	32
2.4.4	Bending Energy	35
2.4.5	Membrane Energy	35
2.4.6	Core Energy	37
2.4.7	Work Done	39
2.4.8	Total potential energy	40
2.4.9	Critical load	42
2.4.10	Solution of the fully nonlinear problem	42
2.4.11	The solution process	46
2.4.12	Solution strategy	47
2.4.13	TBT and RBT solutions from Wade et al (2010)	50
 3	 Modelling localized buckling in sandwich struts with inhomogeneous deformations in both face plates	 55
3.1	Analytical modelling	56
3.1.1	Strain energy	59
3.1.2	Bending energy	59
3.1.3	Membrane energy	60
3.1.4	Core strain energy	61
3.1.5	Work done by applied load	62

3.1.6	Total potential energy, critical load and equilibrium equations	63
3.2	Nonlinear stability analysis	65
3.2.1	Results	66
3.3	Conclusions	73
4	Modelling interactive buckling for FGM sandwich struts	75
4.1	Functionally graded core materials	76
4.2	Sandwich structures with FGMs	77
4.3	Analytical modelling	79
4.3.1	Strain energy	81
4.3.2	Total Potential Energy	83
4.3.3	Critical load	86
4.3.4	Governing Equations	87
4.3.5	The solution process	90
4.4	Results and discussion	91
4.4.1	Material and geometrical properties	91
4.4.2	Convex parametric study	93
4.4.3	Concave parametric study	99
4.5	Conclusions	104
5	Comparison of analytical models with finite element simulations	107
5.1	Finite element method	108
5.2	Buckling and postbuckling analysis	110
5.3	Errors	113
5.4	Modeling sandwich structures with Finite Element	114
5.4.1	Sandwich strut finite element models in the literature	115
5.4.2	Current model	117

5.5	Comparison of FE simulations with the mechanical models in Chapter 3	119
5.5.1	Conclusions	123
5.6	Comparison of FE simulations with mechanical results from Chapter 4	124
5.6.1	Conclusions	131
6	Discussion	133
6.1	Modelling localized buckling in sandwich struts with inhomogeneous deformations in both face plates	135
6.2	Modelling interactive buckling for FGM sandwich struts	136
7	General conclusions and further work	139
7.1	Conclusions	139
7.2	Originality	142
7.3	Further work	143
A	Non-Dimensionalization of system equations of Chapter 4	145
	References	151

List of Figures

1.1	A typical configuration for sandwich panels.	2
1.2	Interactive localized buckling exhibited in the more compressed face plate and local deformations within the less compressed faceplate as exhibited in (a) experimental work (Wadee 1999) and (b) FE simulations performed in ABAQUS (Wadee et al 2010).	3
1.3	(a) Euler's uniform elastica under axial load. (b) Linear solution to elastica problem.	5
1.4	Description of the rolling ball analogy. (a) Minimum point, (b) maximum point and (c) saddle point.	9
1.5	A graphical description of the elastic stability axioms. Every point along the equilibrium path is a stationary solution and that stable paths are associated with minima in the energy while unstable paths are associated with maxima.	10
1.6	A reticulated or triangulated column. (a) Unbuckled state and (b) the column has buckled in an overall mode, but also the bottom side has buckled in a local mode between the joints. . .	12

-
- 1.7 Augusti (1964) model and sketches of its typical equilibrium paths. (a) The initial configuration with rotational spring of stiffness c_1 and c_2 acting in the xz and the yz planes respectively. (b) The buckled configuration with generalized angular coordinated Q_1 and Q_2 representing the rotational deformation in the springs. Equilibrium paths for the cases where (c) $c_2 > c_1$ and (d) $c_1 = c_2$. Symbols C , B and S represent the critical buckling point, the higher buckling load point, and the secondary bifurcation point respectively. The equilibrium paths of the model with initial geometric imperfections are also shown to demonstrate the erosion in the ultimate load due to geometric imperfections. 13
- 1.8 Top: the response of a sandwich strut if the two principal buckling modes are treated separately. Bottom: the coupling of the two buckling modes leads to a secondary bifurcation and an unstable response. (a) The pre-buckling fundamental path associated with squatiushing; (b) overall mode post-buckling initiated at critical bifurcation C ; (c) local face plate post-buckling response which remains inactive and (d) the interactive buckling response being triggered at a secondary bifurcation S . Path (e) shows the equilibrium diagram after the introduction of an initial imperfection E_0 . Quantities E^C and E^S refer to the respective end shortening values at the critical and secondary bifurcations. 16
- 1.9 Link-spring (Hunt et al 1989) model illustrating the effect of localized and periodic deformation on the equilibrium path. . . . 17
- 2.1 Example for sandwich applications A380 (Herman et al 2005). . . 22

2.2	Overall view of the novel sandwich composite footbridge in civil engineering (Chróścielewski et al 2017).	22
2.3	Cellular material classification, where the cellular material with stochastic or periodic microstructures is configured as the cores of sandwich panel structures (Zhu et al 2010).	26
2.4	Schematic illustration of two-dimensional (2D) periodic core used triangular core (Quanjin et al 2021).	27
2.5	The sandwich panel in elevation and cross-section.	30
2.6	The three buckling modes. (a) Overall 'Euler' mode, (b) 'Hour-glass' symmetric mode and (c) 'snake' antisymmetric mode.	31
2.7	Modal descriptions. From top to bottom: Purely compressive; overall buckling sway mode $W(x)$; tilt mode $\theta(x)$; local displacement $u(x)$ and $w(x)$ becoming non-zero beyond the second bifurcation.	32
2.8	Outline of the bending theories. (a) TBT, and (b) RBT	34
2.9	Total endshortening contributions for work done; (a) pre-buckling endshortening; (b) endshortening from lateral displacement $W(x)$ due to overall buckling; (c) in-plane displacement $u(x, 0)$ from the interactive mode.	40
2.10	A graphical representation of the solution process. Point C is found through linear eigenvalue analysis q_s is then varied until the secondary bifurcation is reached and beyond that load P is varied down the postbuckling path. The quantity E^C refers to the value of end shortening at the critical load. Similarly E^S and q_s^S refer to the values of end shortening and amplitude of sway at the secondary bifurcation respectively.	48

2.11	A graphical representation of the equilibrium path showing a number of secondary bifurcations after the critical bifurcation at C . Each bifurcation S_i leads to a different localized solution for w but it is only the first secondary bifurcation that provides the minimum energy configuration.	49
2.12	An example of the use of continuation homotopy. At some point down the post-buckling path of a strut with $b1$, the load parameter P is fixed and b varied. When the desired depth is reached the process is paused and then restarted again after b is again fixed and P in increased to find the secondary bifurcation of the new geometric configuration.	50
2.13	Equilibrium paths Load versus normalized end shortening for strut of length 100mm. (a) Core depth $b = 5.08mm$ and (b) Core depth $b = 10mm$	51
2.14	(a)-(b) Cross-sectional deformation at $x = L/4$ from the end; (a) Core depth $b = 5.1mm$; (b) Core depth $b = 10.0mm$; (c) Shear strain distribution through the core depth.	52
2.15	The evolution of the local modes $w(x)$ for the two models for different stages in the unloading path. (a) $P/P^C = 0.9$ and (b) $P/P^C = 0.6$. In this case: $L = 100mm$ and $b = 5.08mm$	53
2.16	Definition of localized buckle wavelength λ and maximum wave heigh H	54
3.1	From top to bottom: Purely compressive displacement prior to buckling denoted by ΔL ; overall buckling mode $W(x)$; overall tilt mode $\theta(x)$; top face plate transverse $w_t(x)$ and in-plane $u_t(x)$ displacements and bottom face plate transverse $w_b(x)$ and in-plane $u_b(x)$ displacements.	58

3.2	Left: plotting p versus normalized end shortening (\mathcal{E}/L). Right: plotting amplitude of tilt q_t versus amplitude of sway q_s for struts of length $L = 100mm$ and different core depths. $b = 5.08mm$ for (a) and (b) and $b = 10.16mm$ for (c) and (d)	67
3.3	(a) Local mode evolution of face plates unloading for strut of length $L = 175mm$ and core depth $b = 5.08mm$. (a) w_t (b) w_b , (c) u_t and u_b	69
3.4	(a) The overall buckling on a $b = 5.08mm$ and $L = 100mm$ strut at $p = 0.7$. (b) A close look at midspan deformations. While the bottom face plate deformations are easily observed, the top face plate local deformations are not as clear but contribute to the flattening of the top face plate.	70
3.5	Both face plate local displacements for depth $b = 5.08mm$. Length $L = 125mm$ for (a-b) and $L = 175mm$ for (c-d). All are shown at $p = 0.7$	71
3.6	Equilibrium paths for struts with length $L = 100mm$ and core depth (a) $b = 16mm$, or (b) $b = 18mm$. The \mathcal{E}/L gap between the primary and secondary bifurcation points is 0.0024 and 0.0018 for $b = 18mm$	72
3.7	(a) Interactive mode deformation profile for strut of length $L = 100mm$ and core depth $b = 16mm$. (b) Local modes within the top and bottom face plate at $\mathcal{E}/L = 10\%$ within the interactive post-buckling range.	72

4.1	The variation in material properties through the depth of the core. (a)-(d) Convex: From left to right (a) $a_0 > 0, a_1 > 0$; (b) $a_0 > 0, a_2 > 0$; (c) $a_0 > 0, a_3 > 0$; (d) $a_0 > 0, a_4 > 0$. (e)-(h) Concave: From left to right (e) $a_0 > 0, a_1 < 0$; (f) $a_0 > 0, a_2 < 0$; (g) $a_0 > 0, a_3 < 0$; (h) $a_0 > 0, a_4 < 0$. When $a_1..a_4 = 0$ the distribution of material properties is constant through the depth of the strut.	81
4.2	(a)-(b) The variation in material properties through the depth of the core. (a) Convex parametric studies cases and (b) Concave parametric studies cases.	92
4.3	Left: plotting P versus normalized end shortening \mathcal{E}/L , Right: plotting amplitude of tilt q_t versus amplitude of sway q_s for struts of core depth $b = 5mm$. (a)-(b) TBT model and (c)-(d) RBT model.	94
4.4	Interactive buckling on a sandwich panel $100mm$ long and $6mm$ deep at 5% end shortening.	95
4.5	The evolution of the local modes (a),(c),(e),(g) $w(w)$ and (b),(d),(f),(h) $u(x)$ for the convex cases in the unloading path $\mathcal{E}/L = 5\%$. In this case: $L = 100mm$ and $b = 6mm$	97
4.6	Comparison of the critical loads and gap between critical and second bifurcation point from the two analytical model for different core depth. (a)-(b) TBT model, (c)-(d) RBT model. Convex parametric study.	99
4.7	Equilibrium paths for concave parametric study for length $100mm$ and depth $5mm$. (a) TBT model, (b) RBT model.	101
4.8	The evolution of the local modes $w(x)$ for the concave cases in the unloading path $\mathcal{E}/L = 5\%$. In this case: $L = 100mm$ and $b = 6mm$	102

4.9	Comparison of the critical loads and gap between critical and second bifurcation points from the two analytical model for different core depth. (a)-(b) TBT model, (c)-(d) RBT model. Concave parametric study.	104
5.1	A diagram exhibiting the two incremental methods on a post-critical bifurcation system. (a) Load control and (b) displacement control. Symbols indicate "○" large step load control, "●" small step load control and "◇" displacement control.	113
5.2	(a) Finite element sandwich panels, (b) The boundary conditions applied to the finite element model.	118
5.3	Comparison of equilibrium paths for different struts of Length $L = 100mm$ and core depths of: (a) $b = 5.08mm$, (b) $b = 7.63mm$, (c) $b = 16mm$ and (d) $b = 18mm$. (a) - (b) Overall buckling is critical; (c) - (d) Local buckling is critical.	121
5.4	Comparison of deformation profiles from the analytical model and FE simulations for strut of depth $b = 12.7mm$ and length $L = 100mm$ at $\mathcal{E}/L = 2/2\%$. (a) Total deformations; (b) bottom face plate local deformations w_b and (c) top face plate local deformations w_c	122
5.5	Comparison of deformation profiles from the analytical model and FE simulations for strut of depth $b = 16mm$ and length $L = 100mm$ at $p = 0.80$. (a) Total deformation; (b) bottom face plate local deformations w_b and (c) top face plate deformations w_t . Note that the FE results in (a) is possibly affected by the selected imperfection used to trigger buckling in the nonlinear analysis.	124
5.6	Plotting $P(N/mm)$ over the number of elements in the core thickness.	125

5.7	The variation in the core materials properties through its the depth of the core and the approximation used in the FE simulation for a sandwich strut. The same FE approximation used for the other gradation modes.	126
5.8	A schematic of the in-plane displacement due to overall buckling as this was seen in the finite element simulations at quarter length along the length of the strut (a) Convex parametric study; (b) Concave parametric study.	127
5.9	(a)&(c) Comparison of the critical loads from the two analytical models and FE simulations for different gradation patterns pattern. (b)&(d) The variation of the position of the secondary bifurcation for different gradation patterns.	129
5.10	Left: Convex case. Right: Concave case. Equilibrium paths for strut for length 100mm and depth 6mm. (a)-(b) TBT model, (c)-(d) RBT model, (e)-(f) FE model.	130

List of Tables

2.1	Rapid development of sandwich structure according to the history timeline (Quanjin et al 2021).	20
2.2	Mechanical properties of some common materials for face plates (Zenkert 1995).	24
4.1	$a_0 \dots a_4$ Material parameters. Note that E_C is the Young's modulus for the core center, E_{CE} is the Young's modulus for the core edge. Cases between C1.1-ve to C3.4-ve refers to concave distribution shape and C1.1-ex to C3.4-ex refers to convex distribution shape.	90
4.2	The critical load for overall buckling for core depth $b = 5mm$ with different convex FGM patterns.	93
4.3	The critical loads, end shortening and gap between critical and secondary bifurcations for core depth, $b = 6mm$ with convex FGM patterns for different cases.	98
4.4	The Critical load for overall buckling for core depth $b = 5mm$ with different concave FGM patterns.	100
4.5	The critical loads, endshortening and gab between critical and secondary bifurcation for core depth $b = 6mm$ with concave FGM patterns for different cases	103
5.1	Comparison of FE and analytical model results, i represents the number of half-sine waves present in the eigenmode.	120

5.2 Comparison the critical load of FE ana analytical models 127

Nomenclature

Abbreviations

FEM	Finite element method
FGM	Functional graded material
RBT	Reddy-Bickford beam theory model
TBT	Timoshenko beam theory model

Coordinates, Stress, Strains, Loads and Energy

$\gamma_{xy}, \gamma_{xz}, \gamma_{yz}$	Shear strain in planes xy, xz, yz respectively
\mathcal{E}	Total end shortening
\mathcal{E}^C	End shortening at critical bifurcation point
\mathcal{E}^S	End shortening at secondary bifurcation point
\mathcal{L}	Lagrangian
$\sigma_x, \sigma_y, \sigma_z$	Direct stress in directions x, y, z respectively
$\tau_{xy}, \tau_{xz}, \tau_{yz}$	Shear stress in planes xy, xz, yz respectively
$\varepsilon_x, \varepsilon_y, \varepsilon_z$	Direct strain in directions x, y, z respectively
P	External load
P^C	Critical buckling load
U_b	Strain energy of bending
U_c	Strain energy stored in the core
U_m	Strain energy stored in the membrane (face plates)
V	Total potential energy
x	Longitudinal direction
y	Transverse direction along core depth
z	Transverse direction along panel breadth

Finte Element Method

$[K_E]$	Material stiffness matrix
$[K_G]$	Geometric nonlinearities stiffness matrix
$[K_T]$	Tangent stiffness matrix
$[T]$	Geometric transformation matrix
Λ	Load factor
$\{d\}$	Set of deformations
$\{f\}$	Set of internal forces
$\{G\}$	Out-of-balance forces
$\{G\}$	Set of nodal displacement
$\{P\}$	Set of equivalent nodal forces

Geometry

$\phi = b/L$	Panel aspect ratio
b	Core depth
c	Panel Breadth
L	Panel Length
t	Face plate thickness

Interactive buckling

Δ	Pure compression strain
$u(x)$	In-plane displacement of more compressed face plate due to local buckling
$u_b(x)$	In-plane displacement of more compressed botton face plate due to local buckling
$u_c(x, y) = [(b - 2y)/2b]u(x)$	In-plane longitudinal displacement
$u_t(x)$	In-plane displacement of more compressed top face plate due to local buckling
$w(x)$	Local buckling on the compressed face plate
$w_b(x)$	Local buckling on the compressed bottom face plate
$w_c(x, y) = [(b - 2y)/2b]w(x)$	Transverse through-core displacement
$w_t(x)$	Local buckling on the compressed top face plate

Linear Mode

$\theta(x)$	Tilt component of overall buckling and / or bending
$\theta_R(x)$	Tilt component for RBT model
q_s	Amplitude of sway component of overall buckling
q_t	Amplitude of tilt component of overall buckling
u_R	In plane displacement for RBT model
u_T	In plane displacement for TBT model
$W(x)$	Sway component of overall buckling and / or bending

Material Properties

ν	Poisson's ratio of face plate
ν_x, ν_y	Directional orthotropic core Poisson's ratios
a_0, a_1, a_2, a_3, a_4	Inhomogeneity parameters for functionally graded materials
$C_x = E_x bc / [2(1 - \nu_x \nu_y)]$	Core axial strain energy coefficient
$C_y = E_y bc / [2(1 - \nu_x \nu_y)]$	Core transverse strain energy coefficient
$D = Etc/2$	Membrane energy coefficient
E	Young's Modulus of face plate
E_x, E_y	Directional orthotropic core Young's moduli
$EI = Ect^3 / [12(1 - \nu^2)]$	Flexural rigidity of one face plate
$G = G_c cb/2$	Core shear strain energy coefficient
G_c	Core shear modulus
$k = 2C_y/b^2$	Core linear transverse stiffness

Subscripts

R	Reddy-Bickford beam theory model
T	Timoshenko beam theory model

Chapter 1

Introduction

Sustainable design and construction has gradually become the mainstream in the structural engineering. Engineers are increasingly required to take full advantage of material resources to design efficient structural systems so as to minimize the adverse effects on the environment due to construction. The advances in material science and manufacturing technology brought forward many light weight and high performance materials for structural purpose (Ashby 1999). Moreover, better understanding of nonlinear mechanics (Thompson and Hunt 1973) as well as advances in computational mechanics and optimization theory (Rozvany 2009), have enabled structural forms to become increasingly slender. However, buckling instability is practically often the governing failure mode of such structures under compression (Timoshenko and Gere 1961; Bažant and Cedolin 2010).

Sandwich structures are one of the most popular and materially efficient structural forms. These structures consists of three main parts as illustrated in Figure 1.1. Two thin, stiff and strong face plates are separated by a thick light and weaker core (Zenkert 1995; Vinson 1999). In most cases the face plates carry the loading, both in-plane and bending, while the core resists

transverse shear loads. A sandwich structure operates in the same way as an I-beam with the difference that the core of a sandwich is of a different materials and is stretched across the breadth of the structure. Therefore, it has wide applications in engineering structures particularly where the self-weight of the structure is a key design constraint factor, such as astronautic, aeronautic, marine and civil engineering applications. A more detailed description of such applications of sandwich structures can be found in Chapter 2.

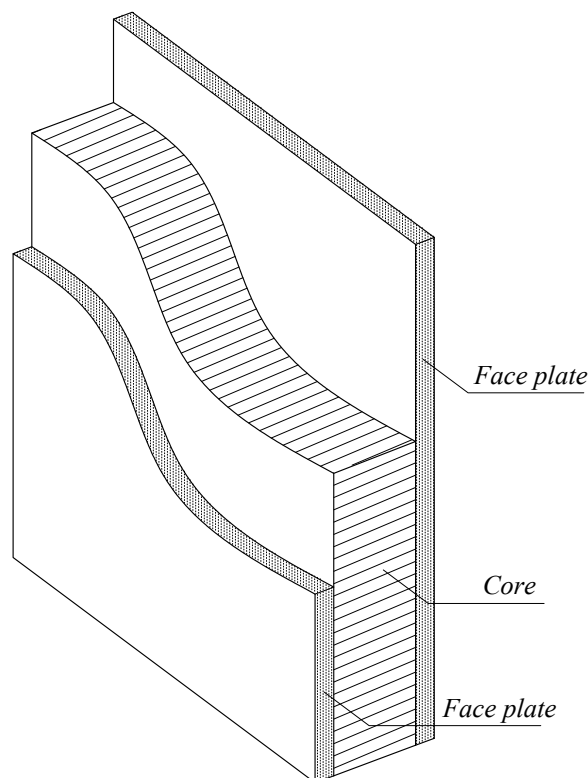


Figure 1.1: A typical configuration for sandwich panels.

The problem arising with very efficient and optimized structures such as sandwich panels, is that it can lead to more than one failure mode being triggered almost simultaneously, which reduce the load carrying capacity of the panels considerably. The buckling of sandwich structures is a familiar and an

extensively investigated problem. The two commonly observed modes of buckling are the long-wave overall buckling and the short-wave face plate wrinkling (Sokolinsky and Frostig 1999). Despite the apparent simplicity of the phenomenon, the prediction of the overall buckling loads is by no mean facile and unambiguous. The phenomenon of wrinkling has been the subject of numerous investigations (Goodier and Neou 1951; Goodier and Hsu 1954). Its is also known that these modes can interact, for example, when overall buckling occurs, localized wrinkling follows in the most compressed part of the facings (Hunt and Da Silva 1990; Hunt and Wadee 1998).

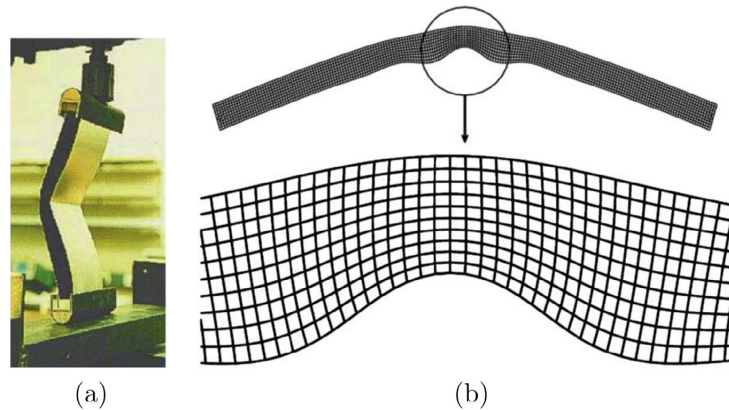


Figure 1.2: Interactive localized buckling exhibited in the more compressed face plate and local deformations within the less compressed faceplate as exhibited in (a) experimental work (Wadee 1999) and (b) FE simulations performed in ABAQUS (Wadee et al 2010).

The current research is a direct continuation of the work of Wadee and Hunt (1998) and Wadee et al (2010) on mode interaction and localization in simply supported sandwich panels. Firstly, the current work seeks to improve and increase the applicability of a previous model (Wadee and Hunt 1998) which considers localized that occurs solely at the more compressed face of the sandwich strut. The aim herein is to present an analytical model that investigates and accounts for local deformations on both face plates. Specifically for the case where overall buckling occurs first, it has been observed both

experimentally (Wadee 1999) and in Finite Element simulations (Wadee et al 2010) that smaller amplitude local deformations begin to appear practically immediately after the secondary bifurcation when local buckling within the other face plate has been triggered as shown in Figure 1.2.

Furthermore the investigation continues in a different direction where two nonlinear analytical models are extended to cater for functionally graded materials in the core. Using these models, the interactive buckling phenomenon is captured and investigated for different gradation patterns. The models have been compared with fully numerical finite element simulations created within the general purpose commercial package ANSYS (2019).

The thesis begins with a review of elastic structural stability theory, paying particular attention to nonlinear buckling phenomena, mode interaction and localized buckling, since these are all manifested in sandwich structures. The second part of the current chapter presents a brief overview of the legacy models (Hunt and Wadee 1998; Wadee et al 2010) which are extended and improved in the subsequent chapters.

1.1 Buckling theory

1.1.1 Linear Buckling

Buckling as a phenomenon has received extensive research and attention in engineering science across different scales. Many different techniques have been used to study buckling in various structures, including experimental, analytical and numerical methods, both in the geometrically linear and nonlinear range. Structures susceptible to buckling can be categorized as one dimensional, two dimensional, or three dimensional. Buckling can be caused by in-plane com-

pression loads, shear loads or torsional loads.

Structures respond differently to various types of loading. It is well-known that structures in tension are limited primarily by their material strength. On the other hand, structures in compression are also limited by their geometry since they might be susceptible to dynamic processes such as buckling. Buckling theory has origins going back to Euler's time (1744), who was the first to formalize the buckling phenomenon as applied to the elastica — a thin and incompressible strut — on simple supports, as shown in Figure 1.3, through the then newly devised method of the calculus of variations. Linearizing the elastica problem led to the following governing ordinary differential equation for the lateral deflection of the strut:

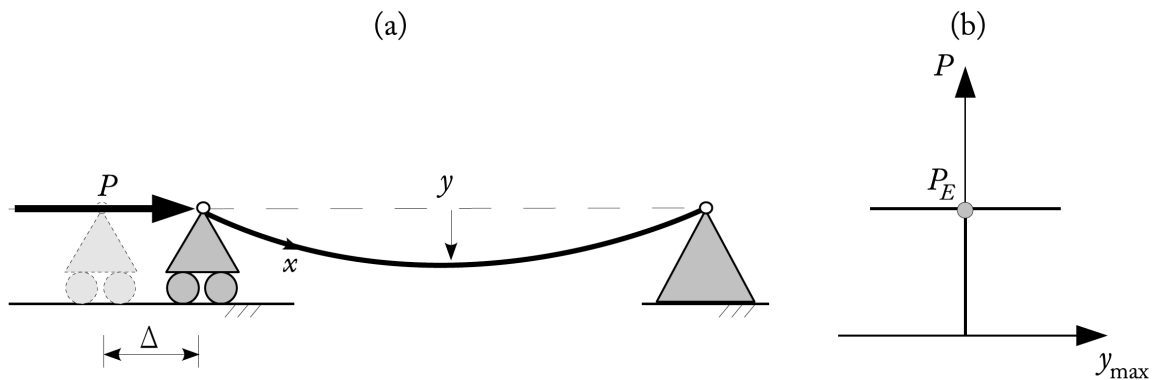


Figure 1.3: (a) Euler's uniform elastica under axial load. (b) Linear solution to elastica problem.

$$EI \frac{d^4 y}{dx^4} + P \frac{d^2 y}{dx^2} = 0, \quad (1.1)$$

where EI is the flexural rigidity of the strut, P is the axial load and y is the function describing the buckled profile of the strut. Integrating the differential equation twice and rearranging, the differential equation of bending is given:

$$Py + C_1 x + C_2 = -EI \frac{d^2 y}{dx^2}, \quad (1.2)$$

The quantity Py is the bending moment resulting from the load eccentricity due to buckling, and is related to the second derivative of lateral displacement, which is equal to the linear curvature term of the strut under small deflections. The constants of integration C_1 and C_2 vanish on the application of simply supported boundary conditions. The critical load P_n^C can be found for the buckling mode n , by solving the above equation:

$$P_n^C = n^2 \frac{EI\pi^2}{L^2}, \quad y = Q \sin \frac{n\pi x}{L}, \quad (1.3)$$

where n is an integer and Q is an indeterminate amplitude of buckling displacement. The lowest critical load which minimizes the potential energy of the strut is the one with the lowest nontrivial value of n (i.e. $n = 1$) leading to the so-called Euler load:

$$P_1^C = P_E = \frac{EI\pi^2}{L^2} \quad (1.4)$$

with its associated mode shape:

$$y = Q \sin \frac{\pi x}{L} \quad (1.5)$$

Even though Euler solved the full nonlinear equation for the elastica, he remains famous in structural engineering primarily for the linear critical load that bears his name. Several applications of linear buckling analysis for different structures are well-documented in Timoshenko and Gere (1961) providing critical loads and buckling mode shapes. The limit of linear buckling analysis can be seen by considering the equilibrium (load versus lateral displacement) path of the structure in Figure 1.3(b). The critical load is found at a bifurcation point, since a perfect and symmetric strut can buckle in more than one direction with equal probability, leading to a different postbuckling path and a loss in stiffness. Since linear theory predicts zero stiffness for the postbuckling response, the implication is that as long as structure remains elastic, the

structure will deflect indefinitely keeping its current load carrying capacity. For some structures, such as columns, the critical load can be a good estimate for their collapse load. However, this is not true for plates supported on their edges since they exhibit significantly positive postbuckling stiffness due to material stretching. On the other hand, in the presence of even very small imperfections, cylindrical shells, for example, will fail due to buckling instability well before the critical load is reached. It is therefore essential to account for the geometric nonlinearities in the formulation for postbuckling analysis. The importance of the postbuckling analysis in estimating the capacity of structures under compression is evident in the incorporation of its finding in design codes for practical structures (Wadee 2007).

1.1.2 Nonlinear buckling

When investigating the postbuckling response in structural problems, it is often more convenient to formulate the governing equations using total potential energy (V) as opposed to applying Newton's laws of motion to a free-body (Wadee 2007). The problem of interactive buckling in sandwich structures leads to large displacements which requires geometrically nonlinear analyses that can be computationally expensive if performed by the direct equilibrium method. This complicates the set of governing equations, raises their order, and adds new boundary conditions. Due to these complications, it may be more efficient to use energy methods in such analyses (Vinson 1999) as long as the loads are conservative. The potential energy methods are powerful tools for stability analysis and for interactive phenomena. The total potential energy V is the algebraic sum of the work done W ($W=-\Phi$) by the applied forces and the stored energies U :

$$V = U + W \tag{1.6}$$

The basis for using the total potential energy V in nonlinear analysis was pioneered principally by Koiter (Hutchinson and Koiter 1970), who presented the first general approach for modeling postbuckling behaviour. Koiter's post-buckling analysis was based on the principle of the minimization of the total potential energy which consists of the strain energy stored in the structure minus the work done by the applied loads. The potential energy is formulated as a continuous integral over the volume of the structure S such that:

$$V = \int \mathcal{L} \, dS. \quad (1.7)$$

The above equation using the calculus of variations the potential energy is stationary when its first variation δV is zero in a direct analogy with dynamical systems, leading to the differential equations of equilibrium. These equations describe the equilibrium states both before and after the critical bifurcations. Bifurcations are points on the equilibrium path where more than one path of equilibrium exists.

Along the same lines, applying the minimum potential energy principle using a discretized system, instead of a continuum, lead to a symmetric perturbation method for post-buckling (Thompson and Hunt 1973):

$$V = V(Q_1, Q_2, \dots, Q_n), \quad (1.8)$$

where the variables Q_i are generalized coordinates that define the displacement profile of the structure. This perturbation method can be explained using the rolling ball analogy for the stability of an equilibrium path as seen in Figure 1.4. If the ball in part (a) is displaced slightly from its original position of equilibrium, it will return to that position upon the removal of the disturbing force. A body that behaves in this manner is said to be in a state of stable equilibrium. In part (a), any slight displacement of the ball from its position

of equilibrium will raise the center of gravity. A certain amount of work is required to produce such a displacement. The ball in part (b), if it is disturbed slightly from its position of equilibrium, does not return but continues to move down from the original equilibrium position. The equilibrium of the ball in part (b) is called unstable equilibrium. In part (b), any slight displacement from the position of equilibrium will lower the center of gravity of the ball and consequently will decrease the potential energy of the ball. Thus in the case of stable equilibrium, the energy of the system is minimum (local), and in the case of unstable equilibrium it is a maximum (local). The ball in part (c), after being displaced slightly, neither returns to its original equilibrium position nor continues to move away upon removal of the disturbing force. This type of equilibrium is called neutral equilibrium. If the equilibrium is neutral, there is no change in energy during a displacement in the conservative force system. This discrete coordinate approach for structures under conservative loading, reduces some of the mathematical; it is based on two fundamental axioms (Thompson and Hunt 1973):

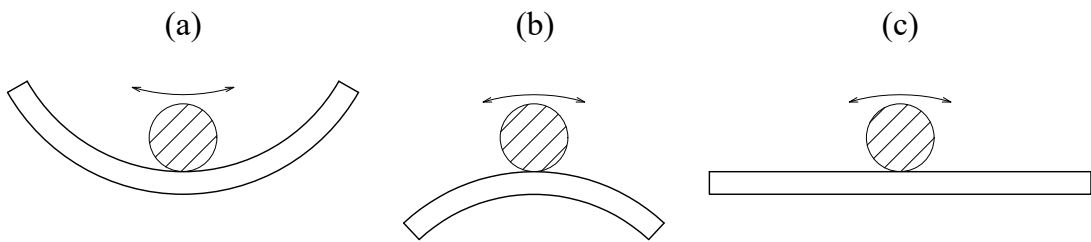


Figure 1.4: Description of the rolling ball analogy. (a) Minimum point, (b) maximum point and (c) saddle point.

Axiom 1 *A stationary value of the total potential energy with respect to the generalized coordinates is necessary and sufficient for the equilibrium of the system.*

Axiom 2 *A complete relative minimum of the total potential energy with re-*

spect to the generalized coordinates is necessary and sufficient for the stability of an equilibrium state.

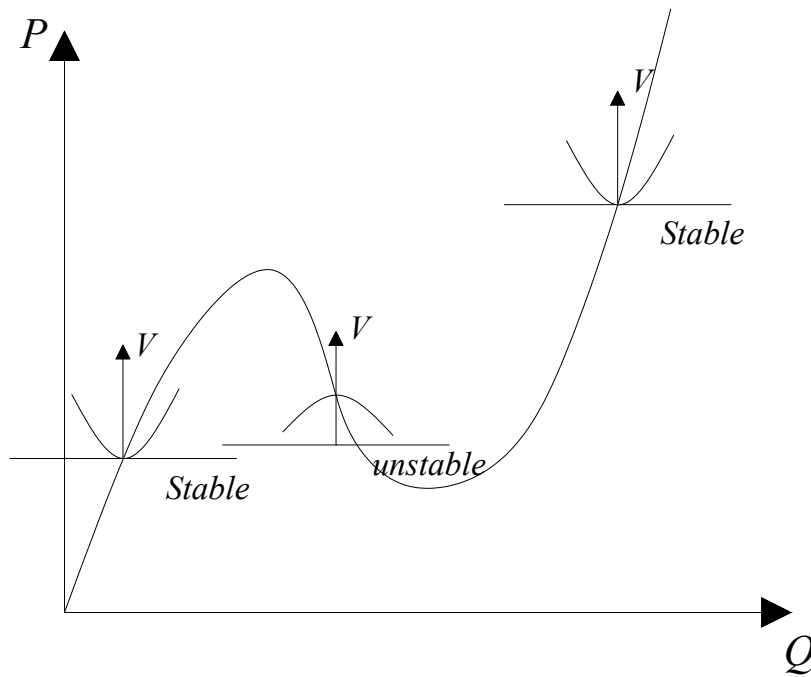


Figure 1.5: A graphical description of the elastic stability axioms. Every point along the equilibrium path is a stationary solution and that stable paths are associated with minima in the energy while unstable paths are associated with maxima.

A graphical representation of the two axioms can be seen in Figure 1.5. The axioms indicate that when the first derivative of V vanishes we have equilibrium and the second derivative of V in most cases defines the stability or otherwise of the equilibrium state. However, the interesting cases arise when the second derivative of V vanishes (these define critical equilibrium), where the structure first buckles ($P = P^C$). For example, if the total potential energy (V) for a single degree-of-freedom system is written as a Taylor series with Q being the generalized coordinate that defines the displacement profile of the structure and δ being a perturbation, we have:

$$V(Q + \delta) = V(Q) + \frac{dV}{dQ}\delta + \frac{1}{2!}\frac{d^2V}{dQ^2}\delta^2 + \dots + \frac{1}{n!}\frac{d^nV}{dQ^n}\delta^n. \quad (1.9)$$

Axiom 1 states that for equilibrium the first derivative of V vanishes ($\frac{dV}{dQ} = 0$), hence V is rewritten:

$$V(Q + \delta) - V(Q) = \frac{1}{2!}\frac{d^2V}{dQ^2}\delta^2 + \frac{1}{3!}\frac{d^3V}{dQ^3}\delta^3 \dots + \frac{1}{n!}\frac{d^nV}{dQ^n}\delta^n + \dots, \quad (1.10)$$

and this implies that the right-hand side of Equation (3.5) to be positive for V to be minimum and therefore the equilibrium state to be stable by Axiom 2, instead when the right-hand of Equation (3.5) is negative the equilibrium state to be unstable.

When the second derivative of V is zero ($\frac{d^2V}{dQ^2} = 0$) the determination of stability gets more complicated as it depends on higher than second derivatives of V . In this case there are more than one postbuckling path. Therefore, further information about the stability of the new equilibrium state, nonlinear buckling analysis (or postbuckling analysis) is required.

1.1.3 Interactive buckling phenomena

Mode interaction, also known as interactive buckling, is a phenomenon where at least two or more buckling modes are observed to be occurring simultaneously. An example of interactive buckling can be observed in reticulated columns. As seen in Figure 1.6, the column buckles in an overall, Euler-type, mode but at the same time the individual compression members on the lower side buckle between the joints. Other examples of interactive buckling under compression, include cylindrical shells, stiffened plates and also the interaction between lateral-torsional buckling and local buckling in beams. Nonlinear

buckling theory, allowed secondary instability, loads and equilibrium paths, to be identified, rather than just the fundamental path and the critical loads. These modes remain usually passive unless interactive buckling occurs.

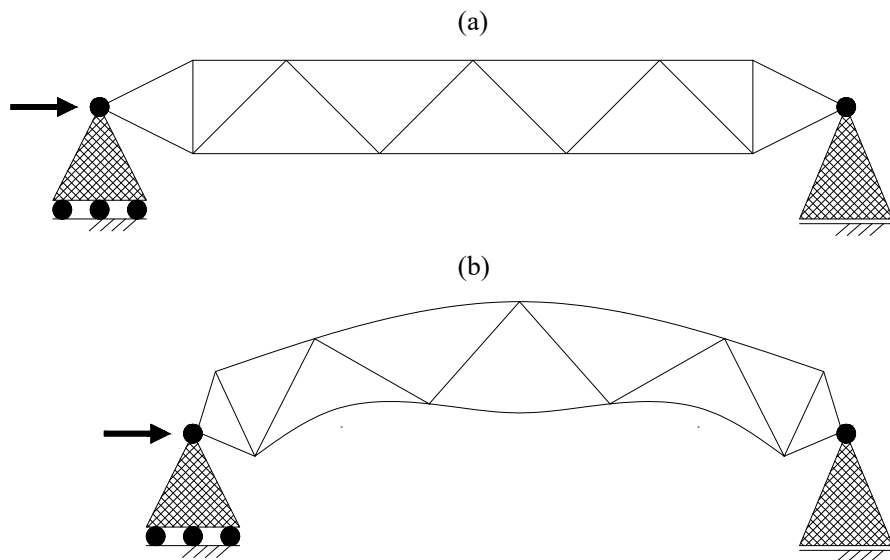


Figure 1.6: A reticulated or triangulated column. (a) Unbuckled state and (b) the column has buckled in an overall mode, but also the bottom side has buckled in a local mode between the joints.

One of the most famous models to portray interactive buckling is the 2-DOF Augusti model (1964), as shown in Figure 1.7, which is used to understand the interactivity of buckling modes that both have stable symmetric postbuckling paths when considered in isolation. The model is made up of a rigid cantilever with length L that is pinned at its base but restrained by two rotational springs with stiffnesses c_1 and c_2 that provide the structural integrity. The deflected profile of the cantilever is described by the angles spanned by the springs, Q_1 and Q_2 . The detailed energy formulation and the corresponding equilibrium path solution of the model can be found in Thompson and Hunt (1973).

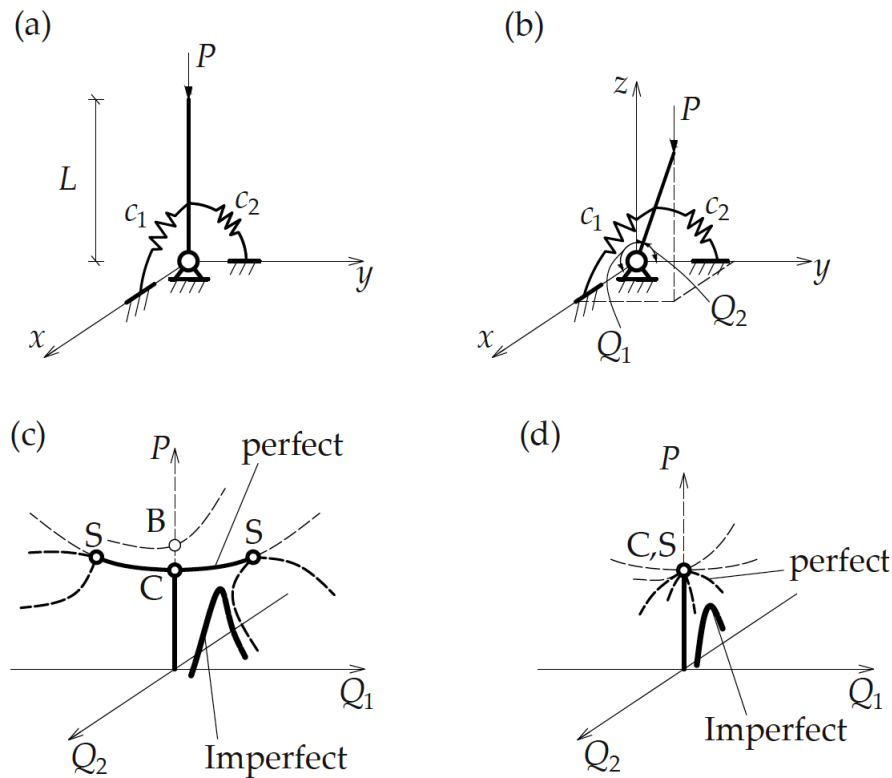


Figure 1.7: Augusti (1964) model and sketches of its typical equilibrium paths. (a) The initial configuration with rotational spring of stiffness c_1 and c_2 acting in the xz and the yz planes respectively. (b) The buckled configuration with generalized angular coordinated Q_1 and Q_2 representing the rotational deformation in the springs. Equilibrium paths for the cases where (c) $c_2 > c_1$ and (d) $c_1 = c_2$. Symbols C , B and S represent the critical buckling point, the higher buckling load point, and the secondary bifurcation point respectively. The equilibrium paths of the model with initial geometric imperfections are also shown to demonstrate the erosion in the ultimate load due to geometric imperfections.

Figure 1.7(c,d) present the sketched of the equilibrium of the Augusti model with $c_1 > c_2$ and $c_1 = c_2$ respectively. When Q_1 and Q_2 are triggered in isolation, i.e. the cantilever purely deflects either in the xz plane or the yz plane, the system exhibits symmetrically stable postbuckling behaviour. However, in realistic scenarios, there is an interaction between Q_1 and Q_2 since there is only finite restraint in the non-critical plane of deflection. For example, the cantilever initially remains undeflected in the fundamental path until P reaches the critical load $P^C = c_1/L$. After that, the cantilever starts to deflect in the direction Q_1 corresponding to the relatively smaller spring stiffness c_1 . When P reaches the buckling load at the secondary bifurcation point $P^S = (3c_1 + c_2)/4L$, the cantilever starts to deflect in Q_2 in addition to Q_1 , i.e. interactive buckling is triggered. The triggering of interactive buckling also leads to unstable post-buckling behaviour. From the perspective of energy, the unstable interactive buckling path requires less energy compared with the primary stable postbuckling path (Timoshenko and Gere 1961; Hunt et al 1989). In particular, when $c_1 = c_2$, the critical and secondary bifurcation points coincide, the postbuckling behaviour is highly unstable, as shown in Figure 1.7(d); the critical buckling load is followed by negative postbuckling stiffness and hence a reduction in the load-carrying capacity.

Mode interaction in sandwich panels which is pertinent to the scope of this thesis herein has been reported by Allen (1969) and Hunt (1986). While investigating sandwich panels under uniaxial compression, it was observed that even though the overall, Euler-type, mode had a largely neutrally stable postbuckling response and the local face plate buckling had a higher critical load with stable postbuckling, mode interaction would limit the neutral response of the energetically lowest mode causing a sudden loss of stability, as shown in Figure 1.8. This nonlinear interaction was initially attempted to be modelled using a periodic Rayleigh–Ritz approach by combining local modes of different

wavelengths in Hunt et al (1988). The method involved the superposition of three buckling modes, the overall Euler-type mode and the two local modes for the face plates with symmetric and antisymmetric waveforms about the panels neutral axis. The method sought to find the minimum energy buckling deformations where both face plates were allowed to buckle locally and the panel globally in combination.

1.1.4 Localization of buckling pattern due to interactive buckling

In contrast to the periodic buckling modes in the purely local buckling cases, interactive buckling also leads to the localization of the local mode, which has been widely observed in both analytical (Hunt and Wadee 1998; ?; Wadee et al 2010; Wadee and Farsi 2014) and experimental (Wadee and Garden 2012; Wadee 1999) studies on interactive buckling of sandwich panels and thin walled structures. Hunt et al (1989) adopted simplified rigid-link and springs systems to illustrate the mechanism of the formation of the localization pattern, as shown in Figure 1.9. If the postbuckling behaviour is stable, the localized pattern requires more energy to trigger and thus the practically observed postbuckling mode is periodic. If the postbuckling behaviour is unstable, the periodic pattern requires more energy to trigger and thus the postbuckling mode is localized. In such case buckling would cause loss of stiffness and strength and therefore would be unsafe.

1.2 Outline of thesis

A brief summary of the chapters in the thesis herein is given below.

1.2.1 Sandwich structures applications and theory

Chapter 2 comprises a literature review on sandwich structures buckling theory summarizing the latest developments in the field while providing deriva-

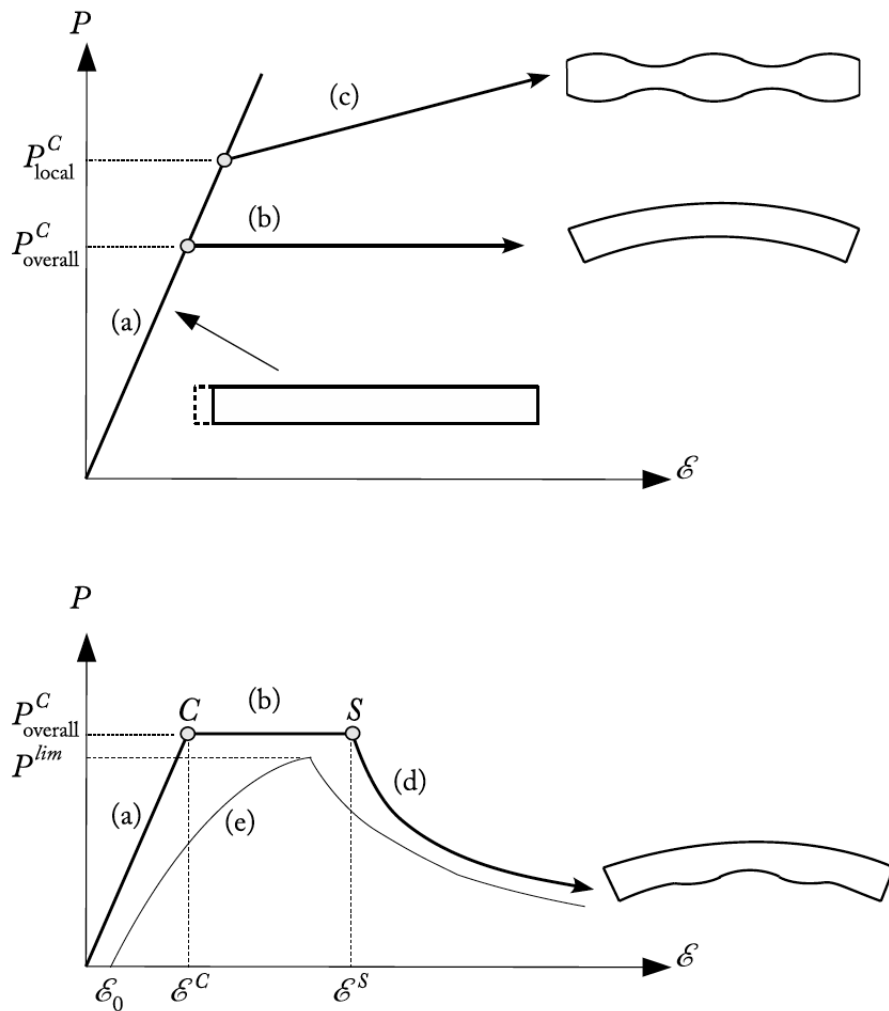


Figure 1.8: Top: the response of a sandwich strut if the two principal buckling modes are treated separately. Bottom: the coupling of the two buckling modes leads to a secondary bifurcation and an unstable response. (a) The pre-buckling fundamental path associated with squashing; (b) overall mode post-buckling initiated at critical bifurcation C ; (c) local face plate post-buckling response which remains inactive and (d) the interactive buckling response being triggered at a secondary bifurcation S . Path (e) shows the equilibrium diagram after the introduction of an initial imperfection E_0 . Quantities E^C and E^S refer to the respective end shortening values at the critical and secondary bifurcations.

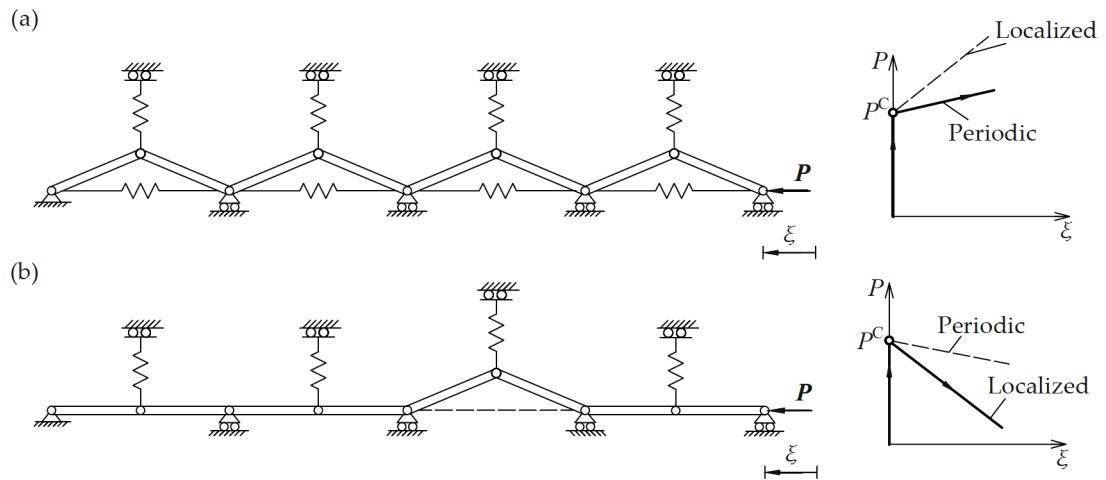


Figure 1.9: Link-spring (Hunt et al 1989) model illustrating the effect of localized and periodic deformation on the equilibrium path.

tions of the critical loads through classical eigenvalue analysis. It concludes with a detailed description of the analytical model for interactive buckling in sandwich struts by Wadee and Hunt (1998) which is utilized in Chapter 3 to investigate localized buckling in sandwich struts with inhomogeneous deformations in both face plates and Wadee et al (2010) which is utilized in Chapter 4 in order to investigate the nonlinear response of sandwich struts with core of graded properties and how different patterns of gradations can affect the response of nonlinear interactive phenomena.

1.2.2 Modelling localized buckling in sandwich struts with inhomogeneous deformations in both face plates

A new analytical model is developed in Chapter 3 in the footsteps of Wadee and Hunt (1998) which is based on a Timoshenko beam theory (TBT) (Timoshenko and Gere 1961) and is extended in order to investigate local deformations on both face plates during postbuckling. This chapter aims to capture these responses of different sandwich configurations and the results are

compared with the results obtained from Hunt and Wadee (1998).

1.2.3 Modelling interactive buckling for FGM sandwich struts

Functionally graded cores are increasingly becoming popular in sandwich construction. They are a step towards further optimization of sandwich panels to fulfil further functions. In Chapter 4, the initiation of interactive buckling in the presence of a functionally graded core is investigated by varying the Young's modulus of the core symmetrically across the depth of the strut for models using the Timoshenko and Reddy-Bickford beams theories. The two strut analytical models presented in Yiatros et al (2013) are updated to include the changes in the shear strain distribution in their total potential energy functional, with a focussed discussion on their validity in the light of the functionally graded distributions of the material properties.

1.2.4 Comparison of analytical models with finite element simulations

In Chapter 5, nonlinear finite element models for sandwich structures are developed in the commercial package ANSYS (2019). The modelling strategy, such as element types, meshing, strut modelling, boundary and loading conditions as well as geometric imperfection are introduced. Moreover, the analysis type, procedure and solution strategy are introduced. The developed finite element models are used to compare with the results from the analytical models in Chapter 3 and 4 in order to deduce the limits of validity and advantages that each model has to offer.

1.2.5 Conclusions and future work

The principal work conducted and discoveries are summarized in Chapter 6. The original contributions and practical significance is also explained and highlighted. The chapter concludes with recommendations for extending the current work and the potential application of the present methodology.

Chapter 2

Sandwich structures applications and theory

Advances in sandwich structures applications continue to rise due to improved manufacturing methods and emergence of new innovative materials and adhesion methods that either amplify the advantages of sandwich construction or mitigate their weaknesses. In this chapter a historical review of sandwich construction is presented, followed by a review of sandwich structures fabrication techniques and materials and concluding with a review of linear and nonlinear stability theory pertinent to sandwich struts.

2.1 Applications

The primary concept or definition of sandwich structure dates back to Fairbairn in 1849, as proposed by Noor et al (1996). The plywood sandwich structure was firstly used in the Mosquito night bomber of World War II in England (Rayjade and Rao 2015). Feichtinger (Vinson 2005) had further stated the concept of sandwich construction originated with the faces made of reinforced plastics and low-density core. In 1944, the first scientific paper con-

cerning sandwich construction was published, which studied sandwich panels subjected to the in-plane compressive loads. Meanwhile, many research publications on sandwich structures emanating from the U.S Forest Products Laboratory used the wood products. In 1992, it was noted that the aircraft engine utilized some honeycomb and increasingly applied 46% honeycomb structure of the wetted surface of the newer Boeing 757/767. Composite sandwich bridge deck panels were used to replace the conventional bridges, which highlighted the lightweight and corrosion resistance of composite sandwich construction. For the past 10 years, different properties of sandwich structures have been investigated with various loading conditions. It is found that sandwich structures have been widely used in numerous applications such as aircraft, transportation and infrastructure (Vinson 2001; Takeda et al 2007). The rapid historic development of sandwich structures is briefly shown in Table 2.1.

1849s	•	The concept of sandwich construction
1924s	•	Polymer sandwich construction
1943s	•	Fabricated BT-15 fuselage
1944s	•	First research paper on sandwich panels
1951s	•	U.S. Forest Products Laboratory (USFPL)
1966s	•	First sandwich structure book
1975s	•	Naval ship hulls
1989s	•	First international conference on sandwich constructions
1992s	•	Boeing 757/767
1999s	•	Journal of sandwich structures and materials
2005s	•	Composite sandwich bridge deck
2008s	•	Wind blades
2009 - 2019s	•	Mechanical properties of sandwich structure under various loading
Future	•	Other potential applications and development of sandwich structure

Table 2.1: Rapid development of sandwich structure according to the history timeline (Quanjin et al 2021).

The sandwich structures with lightweight concept are used in many modern industrial sectors. Here, we list some recent examples of application areas including aerospace, automotive, marine and civil engineering. To briefly highlight and understand the recent and potential applications of sandwich structures.

Vibration tests of lightweight satellite structures using lattice core sandwich panels were studied, which found that the satellite structure could endure vibration loads during rocket launching (Zhang et al 2018). Sandwich panels with unidirectional corrugated and tubular reinforcements were fabricated and investigated subjected to soft body high velocity impact as used in bird strike tests (Vignjevic et al 2019). The proposed reinforced sandwich panels improved the impact resistance performance with the desired augmented strength and stiffness in one direction, which has promising potential in aerospace area. The rigid-foldable morphing sandwich structures of Miura rigid origami pattern were examined, and the alternative mechanism improved stability and locking capabilities (Gattas and You 2015). The Whipple shield of sandwich panels was developed to protect the unmanned spacecraft from much smaller orbital debris, which offered better performance in the single-purpose orbital debris shields category (Cherniaev and Telichev 2017). The concept of a Non-ablative Lightweight Thermal Protection System (NALTPS) was proposed for Mars exploration mission, which consists of carbon/carbon composite, insulator tiles and honeycomb core sandwich panel (Suzuki et al 2017).

In aerospace applications, lightweight sandwich structures have been successfully developed in the aircraft structure (Zhu et al 2018). Some potential applications where extensive use of sandwich panels include the Concorde supersonic airliner and the General Dynamics F-111, the second case involving honeycomb sandwich panels for the canard and vertical fin (Bannink et al

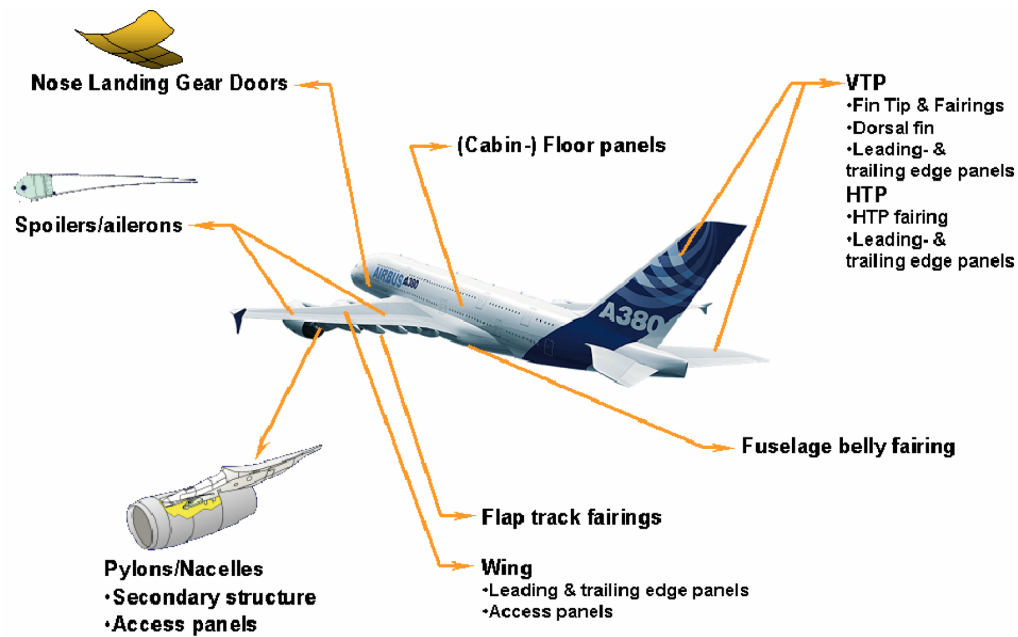


Figure 2.1: Example for sandwich applications A380 (Herman et al 2005).

1978). In the currently evolving technical progress, the two commercial aviation manufacturers Airbus and Boeing have been moving towards an extensive use of composite sandwich panels (Marsh 2005). The commercial aircraft from Airbus, figure 2.1 gives an overview of composite sandwich applications in the A380 aircraft, such as for secondary structures in pylons that connect the engines to the wings, for access, leading and trailing edge panels wings, for the fuselage belly fairing and vertical tail plane as well as for cabin floor panels (Herman et al 2005).

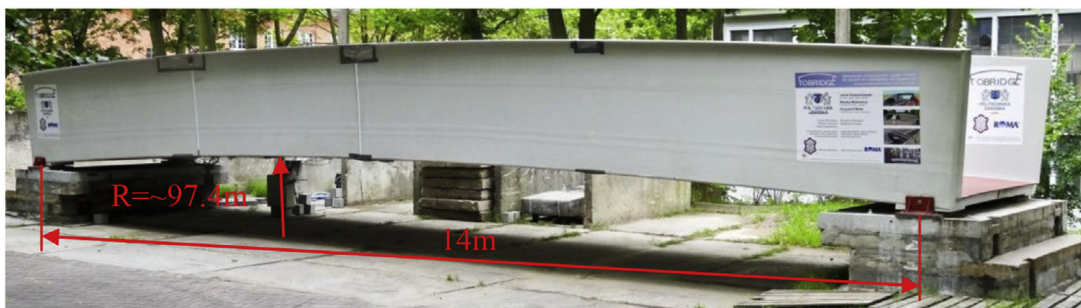


Figure 2.2: Overall view of the novel sandwich composite footbridge in civil engineering (Chróścielewski et al 2017).

Sandwich structures have also found their way into civil engineering projects such as bridge decks, wall and roof claddings for building because of their low cost and thermal performance. For example, can be found in the design of offshore, bridge, nuclear and defence structures mainly as a composite of steel and unreinforced concrete (Narayanan et al 1994; Bowerman et al 2002). Polystyrene/cement mixed cores and thin cement sheet facing sandwich panels were fabricated and studied on insulation and weatherproofing properties, which can be used for almost building applications such as roofs, walls and floors (Tabatabaiefar et al 2017). The novel sandwich footbridge was built and tested under in situ static loading, which was an example of practical applications in civil engineering (Chróścielewski et al 2017), as illustrated in Figure 2.2. Last, but certainly not least, with energy demand rising, the development of technologies for renewable forms of energy has seen the increase in popularity of wind turbines and the use of sandwich composites for the spar of the blades. A sandwich spar can allow the increase of the length of the blades to a point where the height of the tower of the turbine becomes the critical constraint, leading to greater energy output by the turbine (Norlin and Reutelöv 2002; Berggreen et al 2007). Composite sandwich panels are also utilized for the skins of the blades (Brøndsted et al 2005; Østergaard 2008) to reduce the weight even further without a significant loss in stiffness.

2.2 Materials

A wide range of materials can be used for sandwich facings and cores. Every different combination of these components results with sandwich constructions having different mechanical responses. It is important for a sandwich structure to address adequately the attributes of its working environment. There are several different methods for producing structural sandwich panels such as wet lay up, prepreg lay up, adhesive bonding, liquid moulding and

continuous lamination. An excellent review of all these methods can be found in Karlsson and Åström (1997).

2.2.1 Face plate materials

Aluminium alloys, graphite-epoxy, carbon-epoxy, glass-epoxy, and glass-vinyl ester are widely used as face plates materials (Zenkert 1995). Aluminium alloys are most common facing material in sandwich structures. The energy absorption characteristics of metal sheets sandwich structure and aluminium sandwich structure were contrasted with glass fiber-reinforced plastic sheets sandwich structures in the study of Liu et al (2017). High strength carbon fiber/epoxy composite prepreg are used as face plates of composite sandwich panels in the study of Kong et al (2014). FRP including CFRP and glass fiber-reinforced polymer (GFRP) are used to improve the bending characteristics (Prabhu et al 2019). Bao et al (2018) tested the strength of composite sandwich panels with face plates made of carbon/epoxy fabric and carbon/epoxy unidirectional prepreg. Table 2.2 lists mechanical properties of some typical face plate materials.

Face Material	Density (kg/m^3)	Longitudinal modulus (GPa)	Transverse modulus (GPa)	Young's modulus (GPa)	Shear modulus (MPa)	Poisson's ratio
USN [0]	1540	130	10.5	—	5.06	0.28
USN [90]	1540	51.7	51.7	—	19.94	0.30
Aluminium Alloy	2700	72	72	—	27	—
Stycast epoxy resin	1200	2.1	2.1	—	0.81	—
FRP	1200	—	—	43.8	24.8	0.33

Table 2.2: Mechanical properties of some common materials for face plates (Zenkert 1995).

2.2.2 Sandwich core materials

The other main component of the sandwich structures is the core material

(Quanjin et al 2021). Various types of core design on sandwich structure have been proposed to develop the lightweight structures on stiffness, strength and energy-absorbing characteristics. The mechanical properties of sandwich core structures depend on three factors, which are the relative density of the core structure, the properties of the initial used material and geometry of the core materials (Ashby 2006).

In order to improve the mechanical properties of sandwich structures, many types of cellular core structures were proposed and developed, which are generally defined as cellular structures. Cellular structures can be classified as the stochastic cells and periodic cells (Zhu et al 2010). A hierarchical description of cellular materials classification is shown in Figure 2.3. For stochastic structures, metal and polymeric foams are introduced, as open-cell and closed-cell types. For periodic structures, the cell unit is repeated in the array, which can fabricate the two-dimensional (2D) and three-dimensional (3D) core structures.

Sandwich structures with cellular foam cores are classified into two main types, which are metal and polymeric foams. Metallic and polymeric foams have been used extensively as filled-based material, which offers a positive effect on the energy absorption capability of sandwich panels. Metallic foams could be fabricated with one of three methods: foaming by injecting gas into the liquid metal, foaming of melts with blowing agents and foaming of powder compacts. Polymeric foams are manufactured by injecting the gas into liquid polymer and solidifying through the cross-linking or cooling. The metallic foam offers a higher density than the polymeric foam, which leads to excellent energy absorption features at a higher strength level compared to polymeric foam. Polymeric materials such as Polyvinyl chloride (PVC), Polyurethane (PU), metallic (such as aluminium), and biomaterial foams (such as balsa

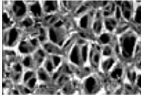


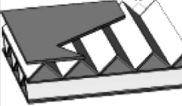



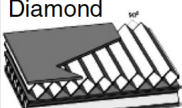

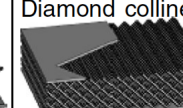




Cellular materials					
Stochastic		Periodic			
Open cell	Closed cell	2D		3D (lattice)	
		Honeycombs	Prismatic	Truss	Textile
		Hexagonal 	Triangular 	Tetrahedral 	Diamond textile 
		Square 	Diamond 	Pyramidal 	Diamond collinear 
		Triangular 	Navtruss 	3D kagome 	Square textile 

Figure 2.3: Cellular material classification, where the cellular material with stochastic or periodic microstructures is configured as the cores of sandwich panel structures (Zhu et al 2010).

wood) are considered as sandwich cellular foam materials.

Two-dimensional periodic cores can be briefly classified into two types of core structures, which are honeycomb core and prismatic core (Xiong et al 2019). The honeycomb core is made of two sheets that form the edge of the unit cell. It is placed perpendicular to the face plate to design a two-dimensional structural core like triangular (Kim and Christensen 2000), square, and circular geometries (Foo et al 2008). For prismatic core, the core is rotated 90° on the horizontal direction (y -axis), which forms the core structure with open channels in single direction (x -axis) and the closed-cell structure in another direction (y -axis). Therefore, prismatic core sandwich structure can provide better cross-flow of air and humidity compared with the closed-channel honeycomb core. Figure 2.4 exhibits the schematic illustration between honeycomb and prismatic core, which is helpful to understand corresponding core geometrical concepts.

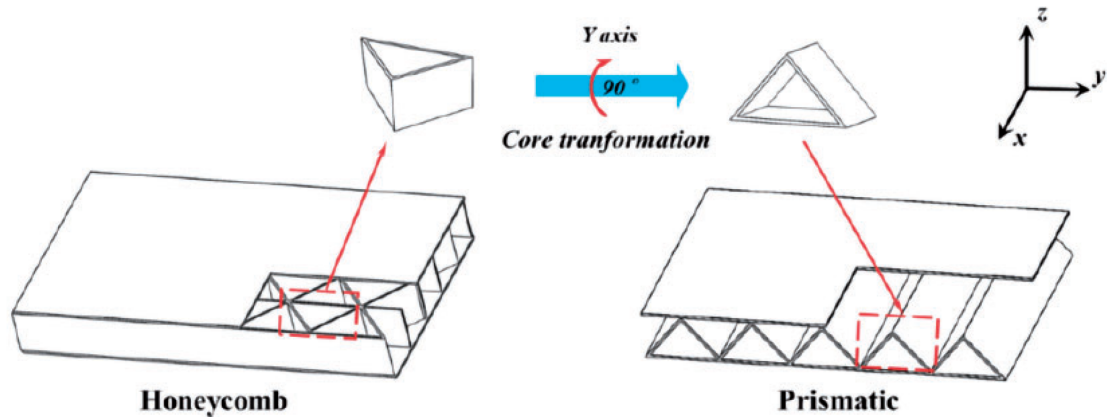


Figure 2.4: Schematic illustration of two-dimensional (2D) periodic core used triangular core (Quanjin et al 2021).

Three-dimensional periodic core is developed based on the geometrical concept of the two-dimensional periodic core. From the core structural perspective, the two-dimensional periodic core enhances the core cavity space through vertical direction (Z-axis), which forms the double 3D open channels. Compared with 2D open channel, the 3D open channel provides the potential core cavity to insert cellular foams, which offers an excellent impact and noise resistance response. For a three-dimensional core, various typical core structures have been summarized and mentioned, such as lattice core, folded core, egg-box core and contoured-core.

2.3 Sandwich structures literature

A considerable amount of literature exists on sandwich structures as they are used in a large number of applications. Research into the theoretical analysis of sandwich structures began following World War II and is summarized in the two classical books of Plantema (1966) and Allen (1969) who gathered all important theoretical knowledge in the subject, including the projects of Reissner (1948) and Goodier (1946) for sandwich structures in aerospace tech-

nology. Zenkert (1995) published a comprehensive book building upon the previous publications and reviewing the latest updates in the field. This book included design guidelines, a discussion of new materials available for sandwich panels and advice on the use of finite element packages to model structural sandwich panels.

Many useful theoretical analyses have been conducted in the past to analyze the global and local buckling of sandwich beam. Many of these studies have been conducted by Frostig and his collaborators on sandwich panels with transversely flexible cores. Frostig and Baruch (1990) investigated bending in sandwich panels and developed an analytical model from two-dimensional equilibrium and compatibility. The flexibility of the core assumed in the analysis, released the assumption of the so-called engineer's bending theory of normal planes in bending. Léotoing et al (2002) and Frostig et al (1992), assumed the core as a linear elastic foundation, and applied a higher-order shear deformation theory for sandwich panels, investigating buckling and localized effects from lateral loads (Frostig and Baruch 1993). The induced cross-sectional nonlinear displacements were not prescribed but solved from the elasticity equations. In both cases, a note of warning is given for the development of localized peeling stresses at the face-core interface that might cause depending, also known as delamination (Frostig 1992). Delamination reduces the local stiffness of the structure leading to destabilization of the panel well below its design load. In the analysis of Allen (1969) and Niu and Talreja (1999), the core is assumed to be elastic isotropic material. They suggested a unified expression for the wrinkling stress of the possible deformation modes expressed through a case parameter, when the beam is pinned at each end.

The buckling mode interaction and localization in terms of the nonlinear postbuckling response has been investigated by many researchers using vari-

ous types of elastic foundation along with presumed sinusoidal modes (Zenkert 1995). Goodier and Hsu (1954) dealt with buckling of an infinitely long sandwich plate and showed that the nonsinusoidal modes, in which the deformation is confined to end zones of the plate, may occur with critical loads that are about one-half of those predicted on the basis of the sinusoidal mode. Hunt et al (1988) investigated mode interaction in sandwich panels for two buckling modes of different scales, which comprised overall Euler-type buckling and wrinkling of the face plates. The initial works concerned a geometrically nonlinear model where the two face plates were modelled as struts and the core as a series longitudinal springs (Hunt 1986). This was followed by a subsequent formulation of a sandwich panel where the core was modelled as an elastic solid in conjunction with the Rayleigh-Ritz method; again the formulation was geometrically nonlinear and considered axial compression (Hunt et al 1988), bending (Hunt and Da Silva 1990), and orthotropic core materials (Da Silva and Hunt 1990).

A number of experimental studies have also been performed to investigate compression response. Fleck and Sridhar (2002) tested various sandwich columns made of different combination of materials and having different geometrical properties. They observed different failure modes depending on the material properties of the core and geometrical properties of the column. Fagerberg (2004) uncovered a transition in the failure mode by examining sandwich beams of different core stiffnesses. He postulated that the transition from wrinkling to pure compression failure (squashing) of the face plate occurs when the modulus of the core is sufficient to support the face plate, in effect a sandwich beam with a high ratio of E_c/E_f , where E_c is the core Young's modulus and E_f the face plate Young's modulus. Wadee (1999) experimental work was focused on capturing of the interactive buckling localization in sandwich panels and achieved good correlation with the localized buckle wavelength and

collapse loads from previous analytical works.

2.4 Analytical modelling of sandwich struts

As mentioned previously, there now follows the detailed derivation of the model presented by Hunt and Wadee (1998). Firstly, the panel reviewed. A sandwich panel of length L and breadth c is considered. The core depth is b and the face plates are of thickness t . The core material properties are assumed to be orthotropic with quantities E_x and E_y corresponding to the Young's moduli of the core in the longitudinal and transverse directions respectively, whereas the Young's modulus for the isotropic face plates is denoted by E . Similarly, Poisson's ratios are denoted by ν_x and ν_y for the core and ν for the face plates. The shear modulus of the core is G_c and since the face plates are assumed to be thin, the shear modulus for the face plates is neglected. The panel is simply supported on the knife edge support at one end with a pinned roller support at the other end. The axial load is assumed to be applied along the neutral axis of the sandwich panel through a rigid plate that spreads the load evenly through the depth of the panel as indicated in Figure 2.5. It is worth emphasizing that the long edges are unsupported, hence the panel modelled is effectively a strut.

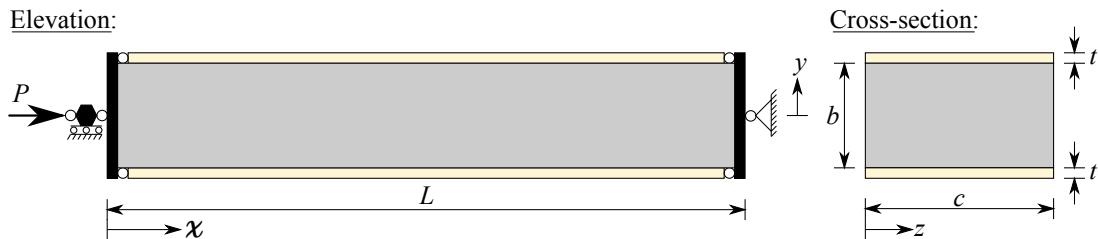


Figure 2.5: The sandwich panel in elevation and cross-section.

2.4.1 Critical load for overall buckling

From Hunt (1986) and Hunt et al (1988) three buckling modes are identified for sandwich panels and are shown in Figure 2.6. The first mode, Figure

2.6(a), is the overall or global ‘Euler-type’ buckling mode, the second, Figure 2.6(b), is a local buckling mode of the face plates where the waveform is symmetric about the longitudinal axis of the panel and is referred to as the ‘hourglass’ mode. The third mode, Figure 2.6(c), referred to as ‘snake’ is a local mode again with waveforms that are antisymmetric about the longitudinal axis. Under compression, depending on the materials and geometry of the panel, the mode with the lowest critical load would become critical and dominate the initial post-buckling response. The ‘snake’ mode can never be critical since it is purely a higher frequency phenomenon akin to the overall mode. Since the current study considers interactive buckling is usually triggered after overall-type buckling, the critical load primary importance is the overall (Euler) buckling load.

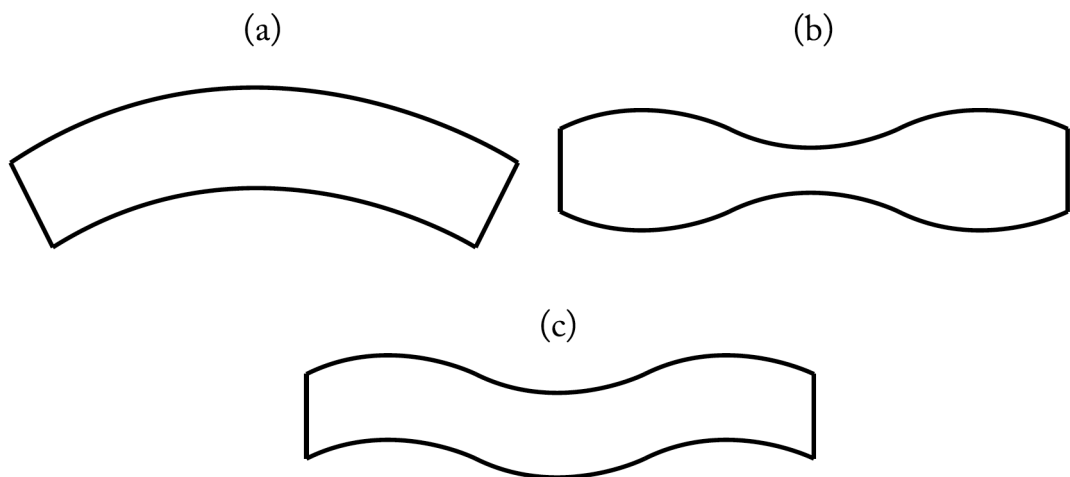


Figure 2.6: The three buckling modes. (a) Overall ‘Euler’ mode, (b) ‘Hourglass’ symmetric mode and (c) ‘snake’ antisymmetric mode.

2.4.2 Overall buckling

The overall buckling mode can be broken into two degrees of freedom; sway and tilt (Allen 1969; Hunt et al 1988). Decomposing the components of the deflection of the neutral axis into functions $W(x)$ and $\theta(x)$ for the overall Euler mode:

$$W(x) = q_s L \sin \frac{\pi x}{L}, \quad \theta(x) = q_t \pi \cos \frac{\pi x}{L} \quad (2.1)$$

where q_s and q_t are the generalized coordinates representing the magnitudes of the sway and tilt components respectively, as seen in the Figure (2.7). The potential energy is then assembled; this comprises the strain energy stored in the structure minus the work done by the applied load. The strain energy of the panels can be broken down into contributions from bending and membrane strains in the face plates, while strain energy contributions in the core come from direct strain and shear.

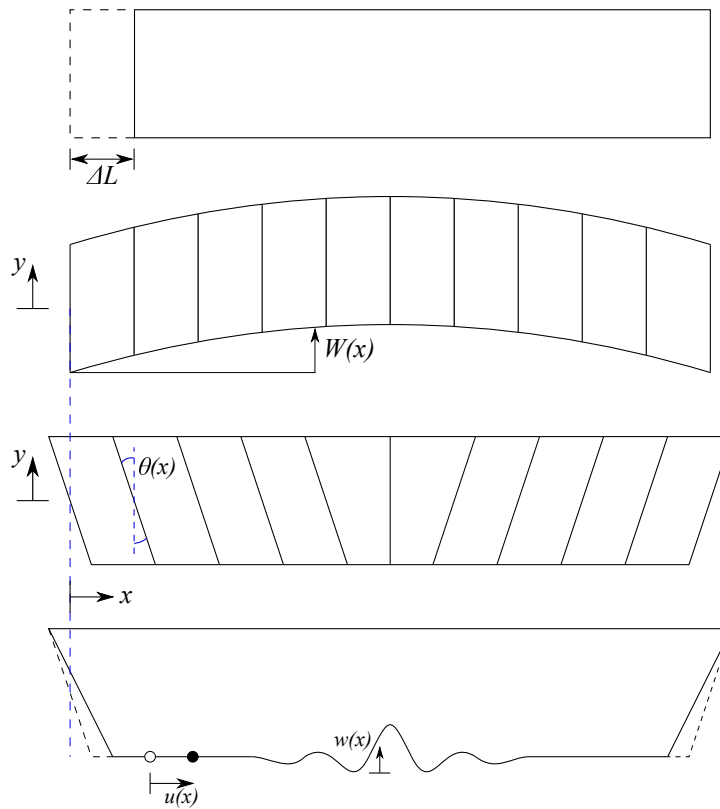


Figure 2.7: Modal descriptions. From top to bottom: Purely compressive; overall buckling sway mode $W(x)$; tilt mode $\theta(x)$; local displacement $u(x)$ and $w(x)$ becoming non-zero beyond the second bifurcation.

2.4.3 Bending theories

A bending theory provides the connection between the applied loads and

the consequent kinematics of the beam. The classical and best-known beam theory is Euler-Bernoulli theory (EBT), which is stated below:

$$M = EI\kappa, \quad (2.2)$$

where M is the applied moment, E is the Young's modulus, I is the second moment of area and κ is the curvature. This can be approximated as the total second derivative of deflection W such that:

$$\kappa = -\frac{d^2W}{dx^2}. \quad (2.3)$$

By integrating the above equation twice and applying the correct boundary conditions the deflected shape of the beam can be found as a function of the induced bending moment, its flexural rigidity and length. The theory's principal assumptions are that "plane section remain plane" and that "shear strains are negligible", leading to a linear distribution of direct stresses (σ) increasing from the neutral axis towards the extreme fibres of the beam:

$$\frac{M}{I} = \frac{\sigma}{y} = -E\frac{d^2W}{dx^2}, \quad (2.4)$$

where y measures the distance from the neutral axis.

A number of refined bending theories have been proposed over the years to overcome the limitations of classical models. Two different shear deformable bending theories considered here (Figure 2.8), that allow the development of shear strains within the sandwich core, these being essential in capturing buckling mode interaction and localization. The first model is based on the Timoshenko Beam Theory (TBT), which assumes a constant shear strain distribution across the core (Timoshenko and Woinowsky-Krieger 1959), and second model is based on third-order Reddy-Bickford Theory (RBT), which assumes a higher order shear strain distribution across the sandwich core (Reddy 1984;

Reddy 1990) which has a quadratic distribution of shear strain; the maximum being at the neutral axis and reducing to zero at the extreme fibres of the cross-section..

$$u_c(x, y) = \left(\frac{b - 2y}{2b} \right) u(x), \quad w_c(x, y) = \left(\frac{b - 2y}{2b} \right) w(x) \quad (2.5)$$

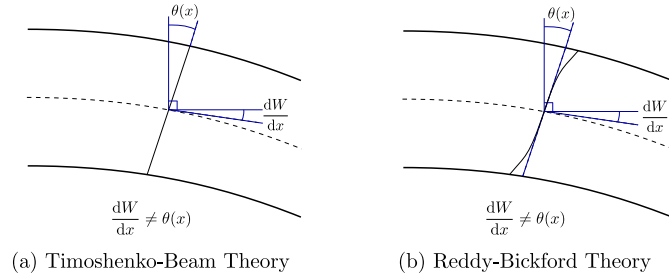


Figure 2.8: Outline of the bending theories. (a) TBT, and (b) RBT

The deformation fields of each model are concerned, the vertical deflections $W(x)$ are the same, whereas the difference lies in overall in-plane deflection u_g :

$$u_{g,T}(x, y) = -y\theta(x), \quad u_{g,R}(x, y) = -y \left[\theta(x) + \frac{4y^3}{3b^2} \left(\frac{\partial^2 W}{\partial x^2} - \theta(x) \right) \right] \quad (2.6)$$

where T and R subscripts to the TBT and RBT models, respectively. A Total Potential Energy approach (Thompson and Hunt 1973) is followed to arrive at the equilibrium equations for the strut. The system's Total Potential Energy comprises the strain energy stored in the sandwich panel minus the work done by the loads, integrated over the volume of the structure. The strain energy has three components of which two are for the face plates in terms of bending energy, U_b and membrane energy, U_m . The third component concerns the strain energy stored in the core and consists of contributions from axial, transverse and shear strains U_c . The work done by the loads include the usual component from the axial load P . Assuming plane stress condition, the potential energy of the strut is readily integrated over the breadth of the strut. The derivation

of the Total Potential Energy is given below for both models.

2.4.4 Bending Energy

The bending energy components provide the resistance to bending and arise from the deflection induced by a moment M and its associated curvature k about the neutral axis of both face plates, coupled with local bending of the bottom face plates. Linear curvature expressions suffice, giving:

$$U_b = \frac{1}{2} \int_0^L M k \, dx \quad (2.7)$$

where, the moment M described in terms of the strut's flexural rigidity and the curvature. However, the strain energy under bending can be obtained as the integral production of the plate rigidity EI and curvature. The expression is the same for the both TBT and RBT models:

$$U_b = \frac{1}{2} EI \int_0^L \left(2\dot{w}(x)^2 + \ddot{w}_b(x)^2 \right) dx \quad (2.8)$$

where, $EI = Ect^3/12(1 - \nu^2)$ is equivalent to the assuming plane stress of a single face plate. The dots over the symbols denote differentiation with respect to x .

2.4.5 Membrane Energy

The membrane energy consists of the strain energy developed in the face plates under axial compression and tension. Considering that the sandwich panel buckles upwards, the displacement components for the top face plate are given as the axial tensile strain minus the squash term. On the other hand, the bottom face plate contributes to the compressive strain, the squash component and some extra contributions from von Kàrmàn large-deflection plate theory added to account for any deviation from the overall mode. Since the two models have different in-plane deformation fields in the overall mode,

the displacement functions will be different. For TBT:

$$u_{x,T}^t(x) = -\frac{1}{2}b\theta(x) - \Delta x \quad (2.9a)$$

$$u_{x,T}^b(x) = \frac{1}{2}b\theta(x) - \Delta x + u(x) \quad (2.9b)$$

$$u_{y,T}^b(x) = w(x) \quad (2.9c)$$

For RBT, some extra terms introduced :

$$u_{x,R}^t(x) = -\frac{1}{2}b\theta(x) + \frac{b}{6}\left(\frac{\partial W}{\partial x} - \theta(x)\right) - \Delta x \quad (2.10a)$$

$$u_{x,R}^b(x) = \frac{1}{2}b\theta(x) + \frac{b}{6}\left(\frac{\partial W}{\partial x} - \theta(x)\right) - \Delta x + u(x) \quad (2.10b)$$

$$u_{y,R}^b(x) = w(x) \quad (2.10c)$$

From Hooke's law, the strain energy is the integral of the product of the stress-strain relationship. Since the plates are long and thin, both transverse and shear stresses are neglected. The out-of-plane stresses are also neglected since the plates are free to expand in the z-direction, eliminating Poisson's ratio effects. Hence, the axial stress, σ , can be formulated in terms of the Young's modulus and axial strain, ε .

$$\begin{aligned} U_m &= \frac{1}{2} \int_0^L \int_{-t/2}^{t/2} \left[\int_{-b/2-t}^{-b/2} \sigma_{xb} \varepsilon_{xb} \, dy + \int_{b/2}^{b/2+t} \sigma_{xt} \varepsilon_{xt} \, dy \right] dz dx \\ &= D \int_0^L (\varepsilon_{xb}^2 + \varepsilon_{xt}^2) \, dx \end{aligned} \quad (2.11)$$

where $D = Etc/2$ and subscripts xt , xb represents the axial properties of the top and bottom face plates. The axial strain in each plate is the sum of the strain from the initial compression and subsequent buckling, while the bottom face adds as extra contributions the corresponding strains du/dx and $\frac{1}{2}(dw/dx)^2$, terms familiar from standard von Kàrmàn large-deflection plate

theory:

$$\varepsilon_{xt} = \frac{\partial u_x^t}{\partial x} \quad (2.12a)$$

$$\varepsilon_{xb} = \frac{\partial u_x^b}{\partial x} + \frac{1}{2} \left(\frac{\partial u_y^b}{\partial x} \right)^2 \quad (2.12b)$$

2.4.6 Core Energy

The core provides all the transverse and shear resistance but only some of the longitudinal resistance, most of which comes from the faces. The displacement field inside the core includes contributions from the elastic end shortening, the overall sway and tilt buckling modes and the localized displacements. To match the assumed displacements $w(x)$ and $u(x)$ on the bottom face and zero in the top face of Figure (3.3) displacements $w_c(x, y)$ and $u_c(x, y)$ must vary through the core Equation (2.5). The TBT displacement field inside the core given as:

$$u_{x,T}^c(x, y) = -y\theta(x) + u_c(x, y) - \Delta x \quad (2.13a)$$

$$u_{y,T}^c(x, y) = W(x) + w_c(x, y) + \nu_x \Delta y \quad (2.13b)$$

For RBT deformation field is given as:

$$u_{x,R}^c(x, y) = -y \left[\theta(x) + \frac{4y^3}{3b^2} \left(\frac{\partial W}{\partial x} - \theta(x) \right) \right] + u_c(x, y) - \Delta x \quad (2.14a)$$

$$u_{y,R}^c(x, y) = W(x) + w_c(x, y) + \nu_x \Delta y \quad (2.14b)$$

The core is modeled as a linear elastic solid and strain energy stored can be formulated as below:

$$U_c = \frac{1}{2} \int_0^L \int_{-b/2}^{b/2} \int_0^c (\sigma_x \varepsilon_x + \sigma_y \varepsilon_y + \sigma_z \varepsilon_z + \tau_{xy} \gamma_{xy} + \tau_{xz} \gamma_{xz} + \tau_{yz} \gamma_{yz}) dz dy dx \quad (2.15)$$

where, τ and γ denote shear stress and strain respectively. The formulation is reduced by allowing the strut to be free in the z -direction reducing the formulation to a state of plane stress where $\sigma_z = \tau_{xz} = \tau_{yz} = 0$, hence:

$$U_c = \frac{1}{2} \int_0^L \int_{-b/2}^{b/2} \int_0^c (\sigma_x \varepsilon_x + \sigma_y \varepsilon_y + \tau_{xy} \gamma_{xy}) dz dy dx \quad (2.16)$$

For orthotropic materials with the plane stress conditions the constitutive relationships given as:

$$\begin{pmatrix} \varepsilon_x \\ \varepsilon_y \\ \gamma_{xy} \end{pmatrix} = \begin{bmatrix} 1/E_x & -\nu_y/E_y & 0 \\ -\nu_x/E_x & 1/E_y & 0 \\ 0 & 0 & 1/G_c \end{bmatrix} \begin{pmatrix} \sigma_x \\ \sigma_y \\ \tau_{xy} \end{pmatrix} \quad (2.17)$$

Upon rearrangement, the stresses can be expressed again in terms of the material properties and strains such that:

$$\sigma_x = \frac{E_x}{1 - \nu_x \nu_y} (\varepsilon_x + \nu_y \varepsilon_y) \quad (2.18)$$

$$\sigma_y = \frac{E_y}{1 - \nu_x \nu_y} (\varepsilon_y + \nu_x \varepsilon_x) \quad (2.19)$$

$$\tau_{xy} = G_c \gamma_{xy} \quad (2.20)$$

This can now be substituted back into Equation (2.16) for the strain energy in the core, taking into advantage of the reciprocal relationship of the constitutive law $E_x \nu_y = E_y \nu_x$:

$$U_c = \frac{1}{2} \int_0^L \int_{-b/2}^{b/2} \int_0^c \left[\frac{1}{1 - \nu_x \nu_y} \left(E_x \varepsilon_x^2 + E_y \varepsilon_y^2 + 2E_y \varepsilon_x \varepsilon_y \right) + G_c \gamma_{xy}^2 \right] dz dy dx \quad (2.21)$$

The expression for the axial strain in the core is similar to the one for the face plates and includes contributions from the initial compression and subsequent buckling. On the other hand, the transverse strain ε_y accounts for the Poisson's ratio effect, the pure compression.

$$\varepsilon_x(x, y) = -y\dot{\theta}(x) - \Delta + \frac{\partial u_c}{\partial x} + \frac{1}{2} \left(\frac{\partial w_c}{\partial x} \right)^2 \quad (2.22)$$

$$\varepsilon_y(x, y) = \nu_x \Delta + \frac{\partial w_c}{\partial y} \quad (2.23)$$

The shear strain consists of the difference between the slope of the deflected neutral axis and cross-sectional plane:

$$\gamma_{xy} = \frac{\partial W}{\partial x} + \frac{\partial u_g}{\partial x} + \frac{\partial w_c}{\partial x} + \frac{\partial u_c}{\partial y} \quad (2.24)$$

2.4.7 Work Done

The work done by the external force is the product of the applied load P , time the total displacement \mathcal{E} at the point of application. For kinematic variable in our model the work done by external force has the form:

$$P\mathcal{E} = P \int_0^L \left(\Delta + \frac{1}{2} \dot{W}^2 - \frac{1}{2} \dot{u} \right) dx \quad (2.25)$$

where the first term is due to the uniform compressive strain Δ (Figure 2.9a) which gives the prebuckling endshortening. The second term is the contribution from the overall buckling lateral displacement W (Figure 2.9b). The last term are the contributions of the localized displacements components of the bottom face plate (Figure 2.9c).

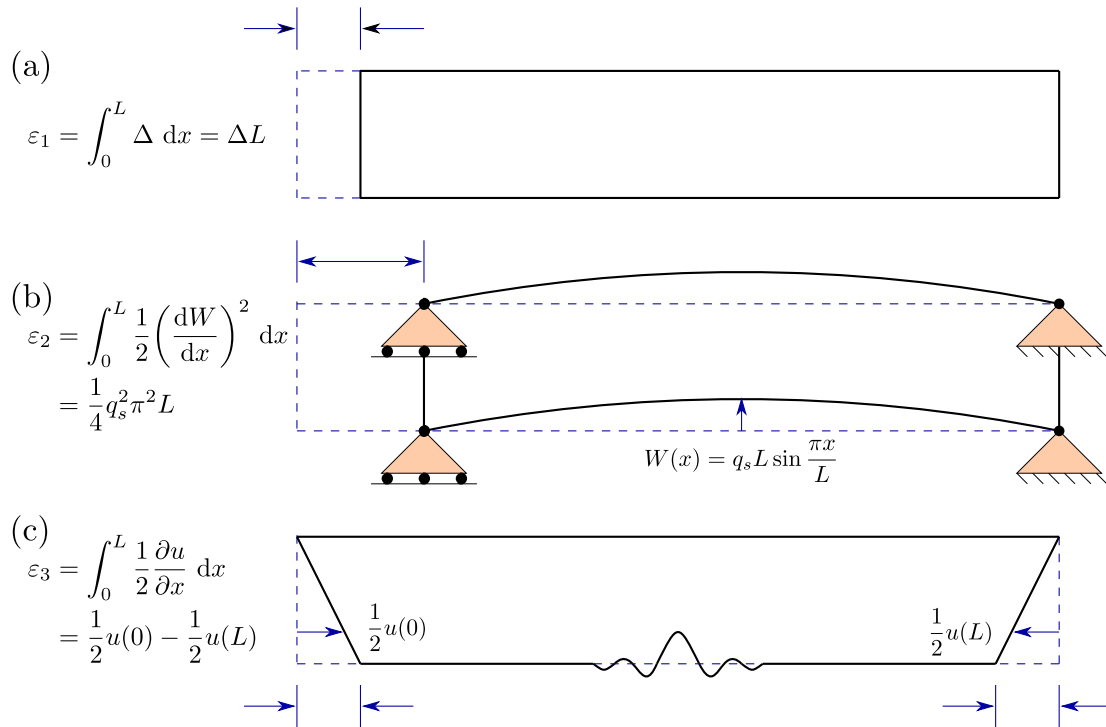


Figure 2.9: Total endshortening contributions for work done; (a) pre-buckling endshortening; (b) endshortening from lateral displacement $W(x)$ due to overall buckling; (c) in-plane displacement $u(x, 0)$ from the interactive mode.

2.4.8 Total potential energy

The total potential energy V , of the strut is obtained by summing all the energy contributions as:

$$\begin{aligned}
V_T &= U_b + U_m + U_c - P\mathcal{E} \\
&= \int_0^L \left\{ G \left[(q_s - q_t)^2 \pi^2 \cos^2 \frac{\pi x}{L} + (q_s - q_t) \pi \cos \frac{\pi x}{L} \left(\dot{w} - \frac{2u}{b} \right) + \frac{u^2}{b^2} + \frac{\dot{w}^2}{3} \right. \right. \\
&\quad \left. \left. - \frac{u\dot{w}}{b} \right] + D \left[2\Delta^2 + \frac{\dot{w}^4}{4} + q_t^2 \frac{b^2 \pi^4}{2L^2} \sin^2 \frac{\pi x}{L} + \dot{u}^2 + \dot{u}\dot{w}^2 - \left(2\Delta \right. \right. \right. \\
&\quad \left. \left. + q_t \frac{b\pi^2}{L} \sin \frac{\pi x}{L} \right) \left(\dot{u} + \frac{\dot{w}^2}{2} \right) \right] + C_x \left[\frac{\dot{w}^4}{20} + \frac{\dot{u}^2}{3} + \frac{\dot{u}\dot{w}^2}{4} - \Delta \left(\dot{u} + \frac{\dot{w}^2}{3} - \Delta \right) \right. \\
&\quad \left. + \frac{q_t b}{12L} \pi^2 \sin \frac{\pi x}{L} \left(q_t \frac{b}{L} \pi^2 \sin \frac{\pi x}{L} - 2\dot{u} - \dot{w}^2 \right) \right] + C_y \left[\nu_x^2 \Delta \left(\dot{u} + \frac{\dot{w}^2}{3} - \Delta \right) \right. \\
&\quad \left. - \nu_x \frac{w}{b} \left(\frac{\dot{w}^2}{3} + \dot{u} \right) \right] + kw^2 + \frac{1}{2} EI \left(\ddot{w}^2 + 2q_s^2 \frac{\pi^4}{L^2} \sin^2 \frac{\pi x}{L} \right) \\
&\quad \left. - P \left(\frac{1}{2} q_s^2 \pi^2 \cos^2 \frac{\pi x}{L} - \frac{1}{2} \dot{u} + \Delta \right) \right\} dx.
\end{aligned} \tag{2.26}$$

$$\begin{aligned}
V_R &= U_b + U_{m,R} + U_{c,R} - P\mathcal{E} \\
&= \int_0^L \left\{ D \left[(2q_t + q_s)^2 \frac{b^2 \pi^4}{18L^2} \sin^2 \frac{\pi x}{L} - (2q_t + q_s) \frac{b\pi^2}{6L} \sin \frac{\pi x}{L} (\dot{w}^2 + 2\dot{u}) + 2\Delta^2 \right. \right. \\
&\quad \left. \left. + \frac{1}{4} \dot{w}^4 + \dot{u}\dot{w}^2 - 2\dot{u}\Delta - \dot{w}^2\Delta + \dot{u}^2 \right] + \frac{EI}{2} \left(q_s^2 \frac{2\pi^4}{L^2} \sin^2 \frac{\pi x}{L} + \ddot{w}^2 \right) \right. \\
&\quad \left. + \frac{C_x}{1260} \left[(5q_s^2 + 32q_s q_t + 68q_t^2) \frac{b^2 \pi^4}{L^2} \sin^2 \frac{\pi x}{L} + 315\dot{u}\dot{w}^2 + 420(\dot{u}^2 - \dot{w}^2\Delta) \right. \right. \\
&\quad \left. \left. - 21(q_s + 4q_t) \frac{b\pi^2}{L} \sin \frac{\pi x}{L} (\dot{w}^2 + 2\dot{u}) + 1260(\Delta^2 - \Delta\dot{u}) + 63\dot{w}^4 \right] \right. \\
&\quad \left. + C_y \nu_x \left[\nu_x \Delta \left(\dot{u} + \frac{1}{3} \dot{w}^2 - \Delta \right) - \frac{\dot{u}w}{b} - \frac{1}{3b} w\dot{w}^2 \right] + \frac{1}{2} kw^2 \right. \\
&\quad \left. + G \left[(q_s - q_t)^2 \frac{8\pi^2}{15} \cos^2 \frac{\pi x}{L} + (q_s - q_t) \frac{2\pi}{3} \left(\dot{w} - \frac{2u}{b} \right) \cos \frac{\pi x}{L} + \frac{1}{3} \dot{w}^2 \right. \right. \\
&\quad \left. \left. \frac{u\dot{w}}{b} + \frac{u^2}{b^2} \right] - P \left(\Delta + q_s^2 \frac{\pi^2}{2} \cos^2 \frac{\pi x}{L} - \frac{1}{2} \dot{u} \right) \right\} dx.
\end{aligned} \tag{2.27}$$

For clarity, some material and geometric constants have been grouped for TBT and RBT models as:

$$EI = \frac{Ect^3}{12(1-\nu^2)}, \quad D = \frac{Etc}{2}, \quad C_x = \frac{E_xbc}{2(1-\nu_x\nu_y)}, \quad C_y = \frac{E_ybc}{2(1-\nu_x\nu_y)}, \quad (2.28)$$

$$G = \frac{G_cbc}{2}, \quad k = \frac{2C_y}{b^2} \text{ and } \phi = \frac{b}{L}$$

2.4.9 Critical load

The critical load for overall buckling is found when the Hessian matrix of the buckling generalized coordinates q_s and q_t becomes singular. This occurs when the determinant of the 2x2 matrix of the second derivatives of the Total Potential Energy V_{ij}^C is equal to zero, where:

$$V_{ij}^C = \begin{vmatrix} V_{ss}^C & V_{st}^C \\ V_{ts}^C & V_{tt}^C \end{vmatrix} = \begin{vmatrix} \frac{\partial^2 V}{\partial q_s^2} |C & \frac{\partial^2 V}{\partial q_s \partial q_t} |C \\ \frac{\partial^2 V}{\partial q_t \partial q_s} |C & \frac{\partial^2 V}{\partial q_t^2} |C \end{vmatrix} = 0. \quad (2.29)$$

Solving Equation 2.29 and setting $w(x)$ and $u(x)$ to zero enables the critical load, P^C to be obtained for TBT and RBT, thus:

$$P_T^C = \frac{2}{\pi^2 EI} L^2 + 2G\phi^2\pi^2 \left[\frac{D + C_x/6}{2G + \phi^2\pi^2(D + C_x/6)} \right], \quad (2.30)$$

$$P_R^C = \frac{2}{\pi^2 EI} L^2 + \frac{840G\pi^2\phi^2(C_x + 6D) + C_x\pi^4\phi^4(C_x + 20D)}{30(168G + 17C_x\phi^2\pi^2 + 70D\phi^2\pi^2)}. \quad (2.31)$$

The first part of the equations 2.30 and 2.31 is the same for the both models since it corresponds to the contribution of the two individual face plates buckling about their minor (weak) axis of bending. The main difference in the two models is the second part of expression and attributed to the presence of the sway mode in the in-plane displacement field of the cross-section.

2.4.10 Solution of the fully nonlinear problem

The equilibrium equations are obtained by treating the potential energy

function V as a Langrangian and minimizing it via variational principles (Fox 1987; Hunt and Wadee 1998). This leads to two non-autonomous nonlinear ordinary differential equations (ODEs), a fourth order ODE in w and second order ODE in u . The minimization process also results in a set of physical boundary conditions for w that are satisfied by assuming simple supports at the ends while for u the conditions are satisfied by considering the applied stresses at the ends. More details on the variational principles can be found in the description in Chapter 4. Presenting the Total Potential Energy as an integral of a Langrangian, for TBT:

$$V = \int_0^L \mathcal{L}(\ddot{w}, \dot{w}, w, \ddot{u}, \dot{u}, u) dx. \quad (2.32)$$

For equilibrium to be satisfied, the potential energy of the loaded sandwich strut must be stationary with respect to x . It is therefore required for the first variation δV to vanish:

$$\delta V = \int_0^L \left[\frac{\partial \mathcal{L}}{\partial \ddot{w}} \delta \ddot{w} + \frac{\partial \mathcal{L}}{\partial \dot{w}} \delta \dot{w} + \frac{\partial \mathcal{L}}{\partial w} \delta w + \frac{\partial \mathcal{L}}{\partial \ddot{u}} \delta \ddot{u} + \frac{\partial \mathcal{L}}{\partial \dot{u}} \delta \dot{u} + \frac{\partial \mathcal{L}}{\partial u} \delta u \right] dx = 0. \quad (2.33)$$

Integrating the first variation of V by parts reveals a set of boundary conditions and two integrals over the length of the sandwich panel in δw and δu :

$$\begin{aligned} \delta V = & \left[\frac{\partial \mathcal{L}}{\partial \ddot{w}} \delta \dot{w} + \left\{ \frac{\partial \mathcal{L}}{\partial \dot{w}} - \frac{d}{dx} \left(\frac{\partial \mathcal{L}}{\partial \ddot{w}} \right) \right\} \delta w + \frac{\partial \mathcal{L}}{\partial \dot{u}} \delta u \right]_0^L \\ & + \int_0^L \left\{ \left[\frac{d^2}{dx^2} \left(\frac{\partial \mathcal{L}}{\partial \ddot{w}} \right) - \frac{d}{dx} \left(\frac{\partial \mathcal{L}}{\partial \dot{w}} \right) + \frac{\partial \mathcal{L}}{\partial w} \right] \delta w \right. \\ & \left. + \left[\frac{\partial \mathcal{L}}{\partial \dot{u}} - \frac{d}{dx} \left(\frac{\partial \mathcal{L}}{\partial \ddot{u}} \right) \right] \delta u \right\} dx = 0. \end{aligned} \quad (2.34)$$

With the assumption of simple supports at the ends of the buckled faces, the physical boundary conditions

$$w(0) = \ddot{w}(0) = w(L) = \ddot{w}(L) = 0, \quad (2.35)$$

eliminate the first two terms in square brackets. Similarly, matching the applied stress at the ends,

$$\dot{u}(0) \left(2D + \frac{2C_x}{3} \right) + \dot{w}^2(0) \left(D + \frac{C_x}{4} \right) - \Delta(2D + C_x - C_y \nu_x^2) + \frac{P}{2} = 0, \quad (2.36)$$

and a similar condition exists for $x = L$. For $\delta V = 0$ this leaves the integrand, which also must vanish to give the equations:

$$\begin{aligned} EI\ddot{w}(x) = & D \left[2\dot{u}\ddot{w} + 2\dot{u}\dot{w} + 3\dot{w}^2\ddot{w} - q_t\phi\pi^2 \left(\sin \frac{\pi x}{L}\ddot{w} + \frac{\pi}{L} \cos \frac{\pi x}{L}\dot{w} \right) - 2\Delta\ddot{w} \right] \\ & + C_x \left[\left(\frac{1}{2}\ddot{u}\dot{w} + \frac{1}{2}\dot{u}\ddot{w} + \frac{3}{5}\dot{w}^2\ddot{w} \right) - q_t \frac{\phi\pi^2}{6} \left(\sin \frac{\pi x}{L}\ddot{w} + \frac{\pi}{L} \cos \frac{\pi x}{L}\dot{w} \right) - \frac{2}{3}\Delta\ddot{w} \right] \\ & + \frac{C_y\nu_x}{b} \left[\dot{u} - \frac{1}{3}\dot{w}^2 - \frac{2}{3}w\ddot{w} + \frac{2}{3}\nu_x\Delta b\ddot{w} \right] \\ & + G \left[\frac{2}{3}\ddot{w} - \frac{\dot{u}}{b} - (q_s - q_t) \frac{\pi^2}{L} \sin \frac{\pi x}{L} \right] - kw, \end{aligned} \quad (2.37)$$

$$\begin{aligned} 2\dot{u} \left(D + \frac{C_x}{3} \right) = & \frac{2G}{b} \left(\frac{u}{b} - \frac{\dot{w}}{2} \right) - 2 \left(D + \frac{C_x}{4} \right) \dot{w}\ddot{w} + \frac{C_y\nu_x}{b} \dot{w} \\ & + \frac{2\pi}{b} \cos \frac{\pi x}{L} \left[\left(D + \frac{C_x}{6} \right) \frac{\pi^2\phi^2}{2} q_t - G(q_s - q_t) \right]. \end{aligned} \quad (2.38)$$

As well as δV being zero for any δw and δu , for equilibrium, V must also be stationary with respect to the generalized coordinates, q_s , q_t and Δ , which reveals three integral constraints equal to zero.

$$P = \frac{2\pi^2 EI}{L^2} + \frac{2G}{q_s} \left[(q_s - q_t) + \frac{1}{\pi L} \int_0^L \cos \frac{\pi x}{L} \left(\dot{w} - \frac{2u}{b} \right) dx \right], \quad (2.39)$$

$$\begin{aligned} & \frac{G\pi}{2\phi}(q_t - q_s) + \left(\frac{C_x}{6} + D\right) \frac{\phi\pi^3}{4} q_t \\ & - \frac{1}{L} \int_0^L \left[\left(D + \frac{C_x}{6}\right) \frac{\pi}{2} \sin \frac{\pi x}{L} \left(\dot{u} + \frac{\dot{w}^2}{2}\right) + \frac{G}{2\phi} \cos \frac{\pi x}{L} \left(\dot{w} - \frac{2u}{b}\right) \right] dx = 0. \end{aligned} \quad (2.40)$$

$$\frac{P}{2} = \Delta(2D + C_x - C_y\nu_x^2) - \frac{1}{2L} \int_0^L \left[D(2\dot{u} + \dot{w}^2) + (C_x - C_y\nu_x^2) \left(\dot{u} + \frac{\dot{w}^2}{3}\right) \right] dx \quad (2.41)$$

The same set of equations for RBT are given below.

$$\begin{aligned} EI\ddot{w}(x) = & -D \left\{ 2\Delta\ddot{w}(x) + (2q_t + q_s) \frac{\phi\pi^2}{3} \left(\sin\left(\frac{\pi x}{L}\right)\ddot{w} + \frac{\pi}{L} \cos\left(\frac{\pi x}{L}\right)\dot{w} \right) \right. \\ & \left. - (2\dot{u}\ddot{w} + 2\ddot{u}\dot{w} + 3\dot{w}^2\ddot{w}) \right\} - C_x \left\{ \frac{2}{3}\Delta\ddot{w} - \frac{3}{5}\dot{w}^2\ddot{w} \right. \\ & \left. + (q_s + 4q_t) \frac{\phi\pi^2}{30} \left(\sin\left(\frac{\pi x}{L}\right)\ddot{w} + \frac{\pi}{L} \cos\left(\frac{\pi x}{L}\right)\dot{w} \right) - \frac{1}{2}(\dot{w} + \ddot{w}\dot{u}) \right\} \\ & - kw - \frac{C_y}{b}\nu_x \left\{ \frac{2}{3}\ddot{w}(w - \nu_x\Delta b) - \left(\dot{u} - \frac{1}{3}\dot{w}^2\right) \right\} \\ & - G \left\{ (q_s - q_t) \frac{2\pi^2}{3L} \sin\left(\frac{\pi x}{L}\right) + \frac{\dot{u}}{b} - \frac{2}{3}\ddot{w} \right\}, \end{aligned} \quad (2.42)$$

$$\begin{aligned} 2\ddot{u} \left(D + \frac{C_x}{3} \right) = & \frac{C_y}{b}\nu_x\dot{w} - D \left\{ 2\dot{w}\ddot{w} - \frac{\phi\pi^3}{3L}(q_s + 2q_t) \cos\left(\frac{\pi x}{L}\right) \right\} \\ & - C_x \left\{ \frac{1}{2}\dot{w}\ddot{w} - \frac{\phi\pi^3}{30L}(q_s + 4q_t) \cos\left(\frac{\pi x}{L}\right) \right\} \\ & - \frac{G}{b} \left\{ \dot{w} + \frac{4\pi}{3}(q_s - q_t) \cos\left(\frac{\pi x}{L}\right) - \frac{2u}{b} \right\}, \end{aligned} \quad (2.43)$$

$$\begin{aligned} P = & \frac{2\pi^2 EI}{L^2} + \frac{16G}{15} \left(1 - \frac{q_t}{q_s} \right) + \frac{D\phi^2\pi^2}{9} \left(1 + \frac{2q_t}{q_s} \right) + \frac{C_x\phi^2\pi^2}{126} \left(1 + \frac{16q_t}{15q_s} \right) \\ & + \frac{1}{q_s L} \int_0^L \left\{ \frac{4G}{3\pi} \cos\left(\frac{\pi x}{L}\right) \left(\dot{w} - \frac{2\dot{u}}{b}\right) - \frac{\phi}{15}(C_x + 10D) \sin\left(\frac{\pi x}{L}\right) \left(\dot{u} + \frac{\dot{w}^2}{2}\right) \right\} dx, \end{aligned} \quad (2.44)$$

$$\begin{aligned} & \frac{4G\pi}{15\phi} (q_t - q_s) + \frac{\phi\pi^3}{630} [q_s (35D + 4C_x) + q_t (70D + 17C_x)] \\ & - \frac{1}{L} \int_0^L \left[\left(D + \frac{C_x}{5} \right) \frac{\pi}{3} \sin \frac{\pi x}{L} \left(\dot{u} + \frac{1}{2} \dot{w}^2 \right) + \frac{G}{3\phi} \cos \frac{\pi x}{L} \left(\dot{w} - \frac{2u}{b} \right) \right] dx = 0. \end{aligned} \quad (2.45)$$

$$\dot{u}(0) \left(2D + \frac{2C_x}{3} \right) + \dot{w}^2(0) \left(D + \frac{C_x}{4} \right) - \Delta(2D + C_x - C_y \nu_x^2) + \frac{P}{2} = 0. \quad (2.46)$$

2.4.11 The solution process

Having formulated the necessary equations, in order to establish the non-trivial interactive modes, the system of governing ordinary differential equations, integral constraints and boundary conditions was non-dimensionalized and solved numerically using AUTO07p (Doedel et al 2012).

AUTO07p is a piece of numerical continuation and bifurcation software primarily for autonomous differential equations. It has very powerful solver which is well-known for its capability to locate bifurcations and trace multiple branching paths as model parameters are varied. AUTO07p utilizes numerous numerical techniques to trace solutions of given problem, such as the current one, which comprises nonlinear non-autonomous ordinary differential equations subject to boundary conditions and integral constraints. Initially the problem is discretized by the method of orthogonal collocation (de Boor and Swartz 1973). The principal numerical continuation technique used by the solver is the modified Newton-Rapson method which is used in a predictor-corrector mode. The solver begins at an initial point in the solution space and estimates a solution which is then corrected iteratively using the above convergence method until the actual solution is found. Beyond folds and limit points, where modified Newton-Rapson fails, the pseudo-arc continuation method is utilized in conjunction with Newton's method (Riks 1972; Riks 1979) since it

allows the continuation beyond these features in the solution space. This is particularly important for the current work since one of the reasons for solving the fully nonlinear equations is to trace the resulting post-buckling equilibrium paths.

Despite its merit in tracing postbuckling paths, it is not possible for the pseudo-arclength method to identify bifurcations in the solution space (Crisfiels 1981; Crisfiels and Wills 1988), whose discovery and location are vital for the current problem under study. This is where the real strength of the solver comes into play since it can locate bifurcations by recognising that the rank of the system of equation's Jacobian reduces by at least one at the location of a bifurcation (Doedel et al 2012). From there, upon the evaluation of the Jacobian, the different post-bifurcation (postbuckling) paths can be traced by finding the solution of the roots of the algebraic bifurcation equation (Keller 1977). Another useful feature of the software is that it allows branch switching at bifurcations where more than one feasible paths are available. This feature has been widely used in the analysis that follows. To conclude, even though the detection of limit points and bifurcations are considered sufficient for the current study, the software can also identify other critical points such as folds, Hopf bifurcations, period doubling bifurcations and torus bifurcations (Glendinning 1994), which shows the wide applicability of the package as a numerical solver for nonlinear problems.

2.4.12 Solution strategy

The two ODEs are solved subject to the three integral constraints, therefore there are four parameters that are free to vary. These comprise the load P , and the three generalized coordinates: the squash strain, the amplitude of sway q_s and amplitude of tilt q_t . One of the parameters is named as the leading parameter and that is varied with the rest of the free parameters being

calculated at the end of each step. The solver is not initiated from the unloaded stage but rather from the primary bifurcation which is located at load P^C and end shortening over length C in the solution space (point C in Figure 2.10) since this is already known from the eigenvalue analysis. Both the load and the squash parameters are normalized against the critical values of P and respectively. Initially, a small perturbation in q_s is applied from the primary bifurcation and the sway parameter, as the leading parameter, is varied by small increments until the secondary bifurcation is reached (S in Figure 2.10).

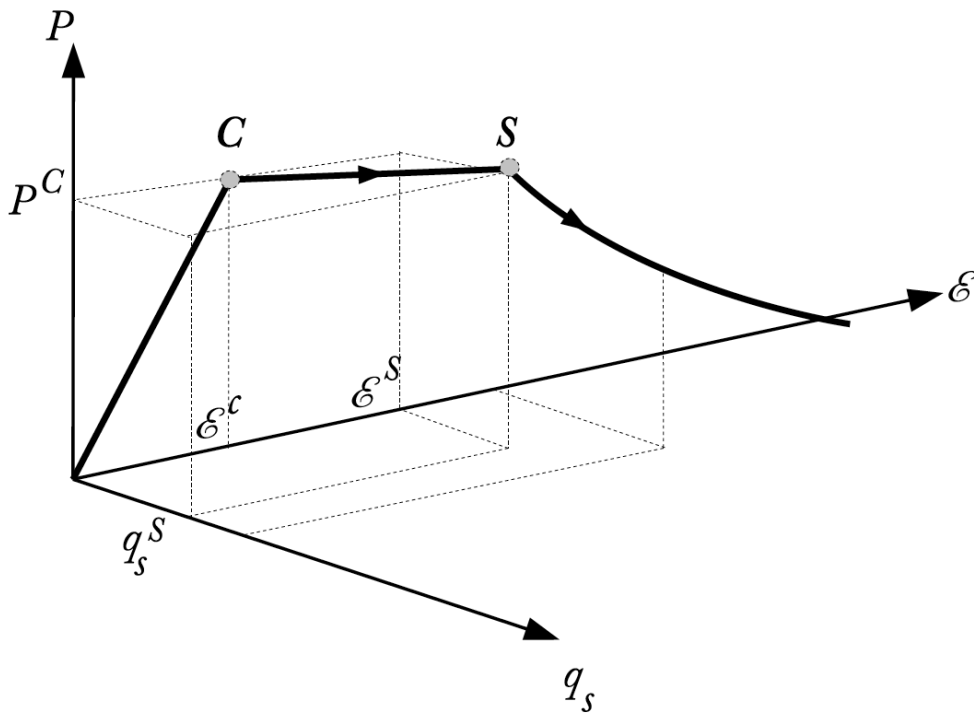


Figure 2.10: A graphical representation of the solution process. Point C is found through linear eigenvalue analysis q_s is then varied until the secondary bifurcation is reached and beyond that load P is varied down the postbuckling path. The quantity E^C refers to the value of end shortening at the critical load. Similarly E^S and q_s^S refer to the values of end shortening and amplitude of sway at the secondary bifurcation respectively.

From experience with the TBT model and initial runs with the RBT model the localized postbuckling solution that minimizes V is the one whose bifurcation occurs first, leading to a symmetric localized wave mode that is maximum

at midspan (Wadee 2000). At this stage, care has to be taken to capture the correct secondary bifurcation which leads to a postbuckling mode that minimizes V_R , as shown in Figure 2.11. When the secondary bifurcation is located, the solver is paused and P becomes the leading parameter which is reduced as the postbuckling path develops. The procedure is halted when a sufficient loss of load bearing capacity or excessive end shortening is reached.

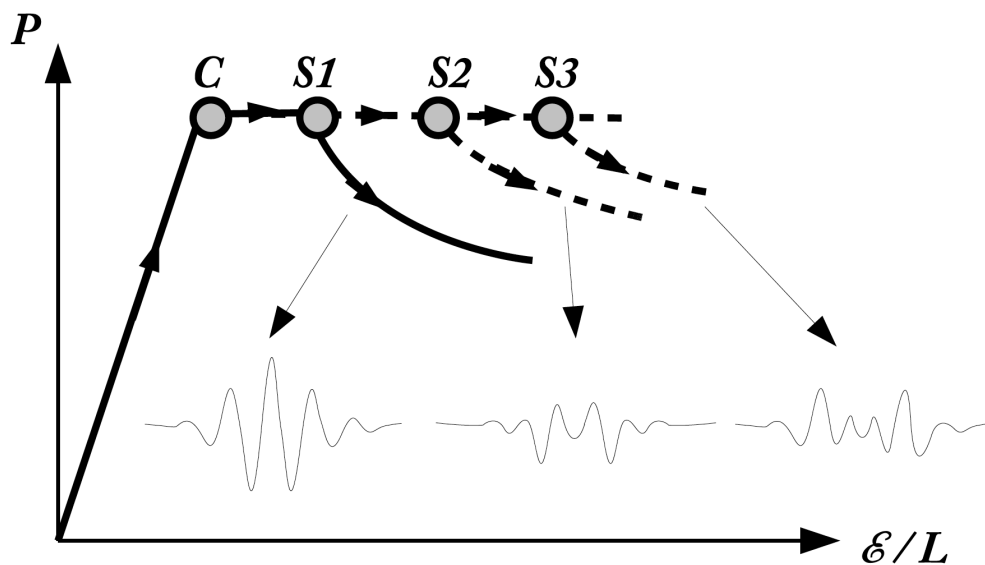


Figure 2.11: A graphical representation of the equilibrium path showing a number of secondary bifurcations after the critical bifurcation at C . Each bifurcation S_i leads to a different localized solution for w but it is only the first secondary bifurcation that provides the minimum energy configuration.

Once the postbuckling path of a strut is determined, the process can be restarted from any point along the path. Since there are only three integral constraints, any four parameters not just the load and the three generalized coordinates can be varied by utilizing numerical continuation on homotopy (Doedel et al 2012), where at any point along the solution path, another path might be traced by replacing one of the free parameters by one that was fixed during the previous computation. For example, the process can be restarted for a given strut by fixing the load parameter at a given value and varying

the depth of the strut b instead with the three generalized coordinates. A new path is then traced which has a constant load over the critical load ratio, but varies in the depth of the core (Figure 2.12). The new path can be continued again by fixing the depth for different cases and then varying the load parameter instead, the secondary bifurcations of the new configurations can be easily found. Homotopy has been widely used during the parametric studies of this thesis and has played a major part in reducing the analysis time, especially when searching for the secondary bifurcation.

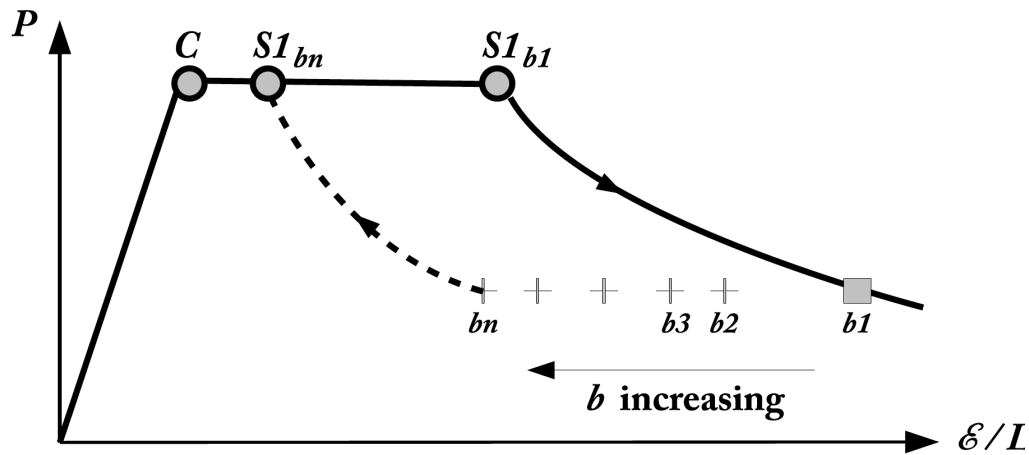


Figure 2.12: An example of the use of continuation homotopy. At some point down the post-buckling path of a strut with b_1 , the load parameter P is fixed and b varied. When the desired depth is reached the process is paused and then restarted again after b is again fixed and P is increased to find the secondary bifurcation of the new geometric configuration.

2.4.13 TBT and RBT solutions from Wadee et al (2010)

The set of equations was solved using the numerical continuation software AUTO (Doedel et al 2012) which allowed the identification of the secondary bifurcation and traced the localized solutions for the postbuckling response. The properties for the sandwich strut are given below and are in accordance with Wadee et al (2010) as a practical configuration for a strut in order to

understand the previous models reported in the literature.

Face plate Young's modulus	: $E = 68947.57 \text{ MPa}$
Face plate Poisson's ratio	: $\nu = 0.3$
Core Young's modulus	: $E_c = 198.57 \text{ MPa}$
Core Poisson's ratio	: $\nu_c = 0.2$
Core shear modulus	: $G_c = 82.74 \text{ Nmm}^{-2}$
Face plate thickness	: $t = 0.50 \text{ mm}$
Core thickness	: $b = 5.08 \text{ and } 10.00 \text{ mm}$
Length of the structure	: $L = 100.0 \text{ mm}$

It is important to note that the sandwich breadth c eliminated from the governing equations without any loss in accuracy. Hence, the breadth c has been taken to be unity and the dimensional axial forces are given as a force per unit width (N/mm) in the results below. In addition the materials are considered to be linear elastic for the ranges of strain of this study.

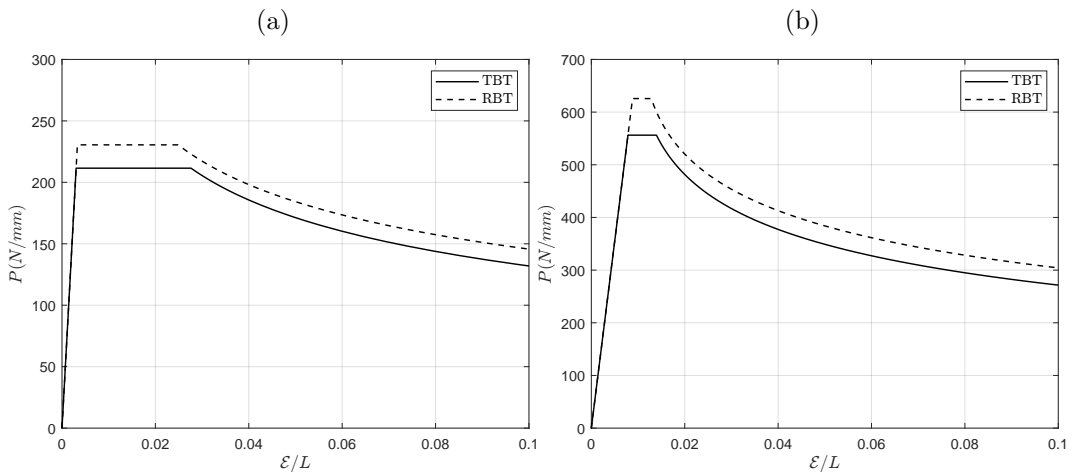


Figure 2.13: Equilibrium paths Load versus normalized end shortening for strut of length 100mm. (a) Core depth $b = 5.08 \text{ mm}$ and (b) Core depth $b = 10 \text{ mm}$.

The equilibrium paths for load versus endshortening for TBT and RBT model are shown in Figure 2.13 for core depth $b = 5.08 \text{ mm}$ and $b = 10 \text{ mm}$.

From these results it is evident that the two models are well correlated with minor differences in the initial stiffness. The first observation is that the RBT model predicts the secondary bifurcation before TBT model, which can be attributed to greater flexibility in shear deformability and leads indirectly to a larger axial stress in the face plates, which exceeds the compressive stress needed to trigger local buckling at midspan significantly earlier than the equivalent TBT model, as shown in Figure 2.14(c), close to the secondary bifurcation.

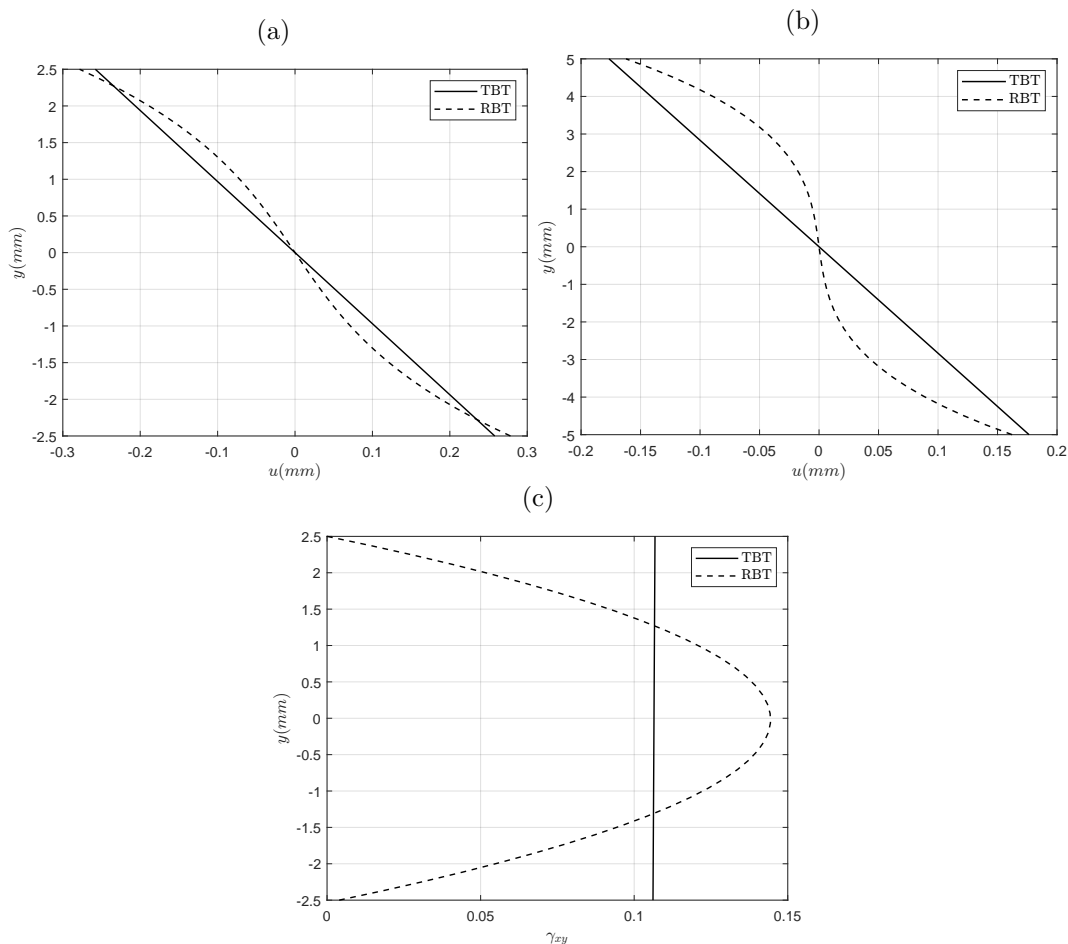


Figure 2.14: (a)-(b) Cross-sectional deformation at $x = L/4$ from the end; (a) Core depth $b = 5.1\text{mm}$; (b) Core depth $b = 10.0\text{mm}$; (c) Shear strain distribution through the core depth.

Hence, the RBT model having zero shear strain (Figure 2.14(c)) at the edges of the core might not be entirely accurate since the zero shear strain

condition applies to the outermost edge of the face plates. It is though a good approximation for the thin face plates, especially where the centroid of the faces plates is taken at the edge of the core. The Reddy-Bickford Theory is more suitable for sandwich panels with deeper cores since it better accounts for local nonlinear deformations of the cross-sectional planes in the neighborhood of the extreme fibres, which can be seen in physical experiments (Wadee 1999). When the core depth is $b = 10mm$, the effect of the higher order deformation is also increased as shown in Figure 2.14(b), hence the assumption of plane sections remaining plane is less likely to hold even approximately. This is also applicable for softer cores where the axial stresses are principally concentrated at the much stiffer extreme fibers and comparatively less strain energy is stored in the core.

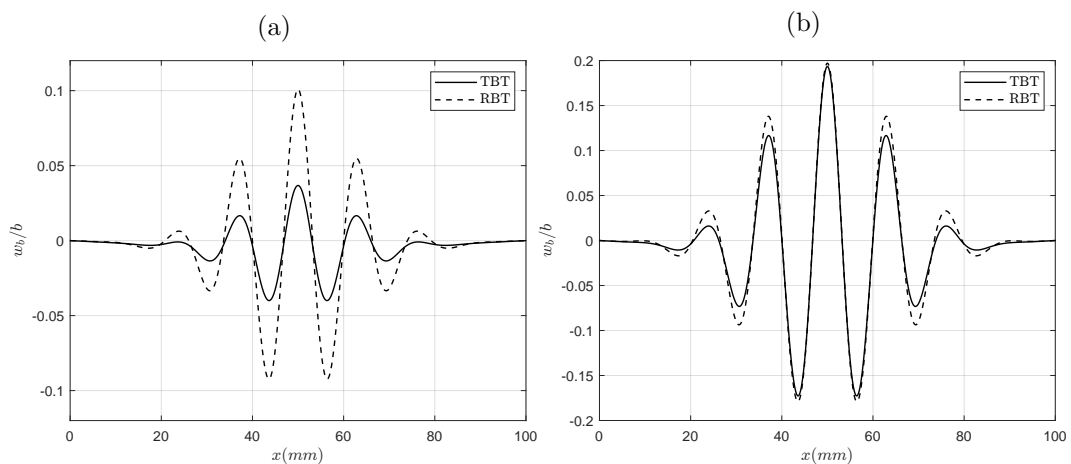


Figure 2.15: The evolution of the local modes $w(x)$ for the two models for different stages in the unloading path. (a) $P/P^C = 0.9$ and (b) $P/P^C = 0.6$. In this case: $L = 100mm$ and $b = 5.08mm$

In addition, the modes of the two analytical models are compared at different stages in the postbuckling path, as presented in Figure 2.15. During the early stages of postbuckling, both the amplitude and the so-called "wavelength of localization" λ —the distance between the first extrema on either side of midspan (Figure 2.16) (Wadee 1999)—are smaller for TBT compared

to the equivalent values for RBT. However, as the path evolves the difference in the modes from the two models is reduced since both wavelength and the maximum amplitudes of w converge. An explanation for the results of the two models converging at the advanced postbuckling state is probably due to the effect of the large amount of lateral deflection, attributed to the overall buckling, which then dominates the behaviour. The growth of the sway amplitude q_s reduces the relative effect of the nonlinear in-plane deformation field—the main difference in the modelling—which grows at a much smaller rate.

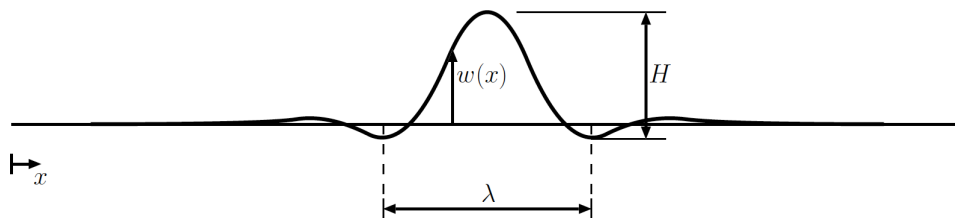


Figure 2.16: Definition of localized buckle wavelength λ and maximum wave height H .

In conclusion, the results of the comparative study between the TBT and RBT analytical formulations have shown that the latter model provides a safer prediction for the location where the secondary instability is initiated as a result of higher axial stress developing in the face plates. This effect is magnified for sandwich panels with deeper cores where the difference between the two models becomes more pronounced. In terms of the critical load, the RBT model overestimates the critical load compared to the TBT model, indicating that the linear in-plane displacement field is a more accurate representation of the actual field.

Chapter 3

Modelling localized buckling in sandwich struts with inhomogeneous deformations in both face plates

Sandwich construction, comprising two stiff face plate separated by a softer core material, is popular as provider of structural combined with weight efficiency and as seen in the previous chapter it is utilized in a multitude of applications in engineering world. However, precisely because they are both specialized and efficient, the responses of sandwich struts are liable to exhibit complicated collapse mechanisms (Hunt et al 1988; Wadee and Hunt 1998; Sokolinsky and Frostig 1999; Fleck and Sridhar 2002). It is well known from classical work that compressed sandwich panels, or more specifically struts sometimes fail by a combination of overall (Euler-type) buckling and local buckling (wrinkling) of the face plates. As presented in Chapter 2, this type of structural response has been previously modelled using combination of non-linear structural stability theory, the appearance of shear strains within core

material being vital in introducing a nonlinear interaction between the overall buckling wavelength scale and the local (face) buckling.

Mode interaction and localization in sandwich structures is a very important phenomenon since it can dominate the post-critical response, regardless of the initiating mode (Wadee 2000). This work seeks to extend the fundamental model for interactive buckling developed by Wadee and Hunt (1998) which considers localization that occurs solely at the more compressed face plate of the sandwich strut. More recently, Wadee and Bai (2014) successfully modeled interactive buckling between minor axis buckling of an I-section strut, using a similar modeling technique. Although this is a different problem, the aim herein is to present an analytical model that investigates and accounts for local deformations on the both face plates during post-buckling. Specifically for the case where overall buckling occurs first, it has been observed both experimentally and in finite element simulations that smaller amplitude local deformations begin appear practically immediately after the second bifurcation when local buckling within the other face plate has been triggered. This chapter aims to capture these responses and study their effects on the post-buckling response of different sandwich configurations. The results from this model are compared with the results obtained from Wadee and Hunt (1998).

3.1 Analytical modelling

In the current work, the original Hunt and Wadee (1998) - hereinafter termed the ‘1998 model’ - is modified to allow local deformations in both face plates. The dimensions of the sandwich strut and the coordinate system are shown in Figure 2.5. The model assumes isotropic face plates with Young’s modulus E and Poisson’s ratio ν as well as an isotropic core material with

Young's modulus E_c and Poisson's ratio ν_c . Loading is applied axially by a compressive force P acting at the mid-section, through rigid end plates to ensure equal load transfer to the face plates.

The purely compressive displacement prior to buckling is represented by ΔL , while overall (Euler-type) buckling is decomposed into sway and tilt components, $W(x)$ and $\theta(x)$ (see Figure 3.1). These components are represented by predetermined trigonometric functions with dimensionless amplitudes q_s and q_t respectively as:

$$W(x) = q_s L \sin \frac{\pi x}{L}, \quad \theta(x) = q_t \pi \cos \frac{\pi x}{L}, \quad (3.1)$$

since it is well known that the solution for the overall buckling mode of simply supported strut can be best approximated by a half-sine wave and the total shear effect is determined by the difference of sway and tilt. The amplitudes q_s and q_t , as well as Δ enter the model as generalized coordinates, which are computed during the solution process. The new model retains the Timoshenko Beam Theory (TBT) for the core material under which shear strains are allowed to develop within the core, which are essential for including the interaction between the two buckling modes of different length scales (Wadee et al 2010). For the range of application of this model (weak, isotropic core and stiff thin face plates) Timoshenko shear deformable theory for the core suffices and offers a sufficiently good approximation of the kinematics of the overall mode. Furthermore, along with the contributions of the sway and tilt components for overall buckling to the displacement of the strut, both face plate $w_t(x)$ is defined as the displacement of the buckled face plate perpendicular to the unbuckled face, and $u_t(x)$ is defined as the displacement parallel to the unbuckled face. The corresponding displacements for the bottom face plate are defined as $w_b(x)$ and $u_b(x)$. These functions of x have no predetermined form and are sought as solutions from the minimization of the total poten-

tial energy functional formulated in a later subsection. To ensure continuity of the displacements within the core, the top and bottom interactive mode displacements are taken to vary linearly with y , as:

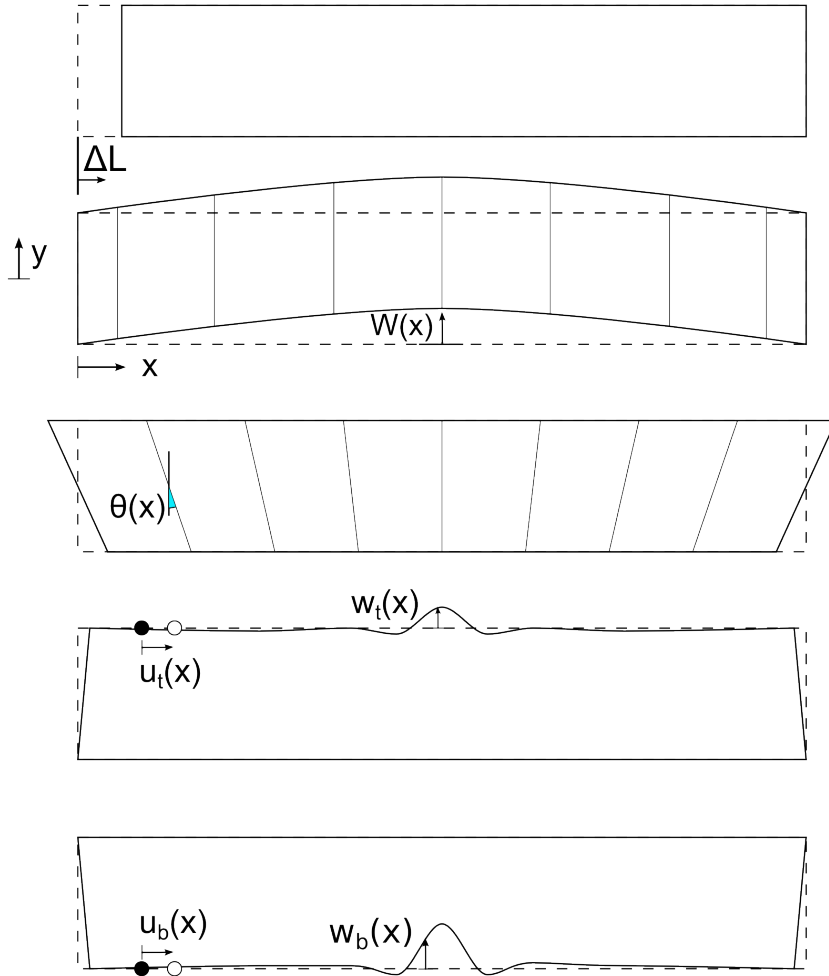


Figure 3.1: From top to bottom: Purely compressive displacement prior to buckling denoted by ΔL ; overall buckling mode $W(x)$; overall tilt mode $\theta(x)$; top face plate transverse $w_t(x)$ and in-plane $u_t(x)$ displacements and bottom face plate transverse $w_b(x)$ and in-plane $u_b(x)$ displacements.

$$w_c(x, y) = \left(\frac{b + 2y}{2b} \right) w_t(x) + \left(\frac{b - 2y}{2b} \right) w_b(x) \quad (3.2)$$

$$u_c(x, y) = \left(\frac{b + 2y}{2b} \right) u_t(x) + \left(\frac{b - 2y}{2b} \right) u_b(x) \quad (3.3)$$

so that pure deformations for each face plate can be easily extracted as the solutions of the governing differential equations, while superposition can be

used to quantify the displacement due to local deformations within the core. The linear variation of each displacement function across the depth of the core was deemed appropriate, since the magnitudes of these displacements are generally small and previous trials with nonlinear variations did not reveal any significant changes in the response.

3.1.1 Strain energy

As in the original work by Hunt and Wadee (1998), a total potential energy approach with large displacement assumptions is followed to arrive at the equilibrium equations for the strut. The Total Potential Energy V of the system comprises the strain energy of the sandwich strut integrated over its entire volume minus the work done by the applied load. In sandwich struts, the face plates are considered to provide the principal resistance to bending. The primary function of the core, on the other hand, is to resist shear deformation and does not intrinsically provide significant bending or axial resistance. Hence, the total strain energy of the strut is compartmentalized into strain energy components associated with pure bending due to buckling, membrane stretching of the face plates with core shear and transverse deformation. Finally, the work done by the applied load is introduced in the potential energy functional. Assuming a plane stress condition, the potential energy of the strut is readily integrated over the breadth of the strut. The procedure for formulating the total energy is thoroughly explained in chapter 2.

3.1.2 Bending energy

Presently, the strain energy due to the overall and local curvature on the face plates is considered. These are taken as their linearized form; the second derivative of global and local lateral displacements, since the bending

strains are small and the cross terms add complexity to the formulation without changing the response significantly. The strain energy from the local and global curvature is assembled, neglecting cross terms that play a negligible role in the total potential energy functional for a sandwich panel geometry where $b \gg t$ and $L \gg b$ or $t \ll b$ and $t \ll L$:

$$U_b = \frac{1}{2}EI \int_0^L \left(2W''^2 + w_t''^2 + w_b''^2 \right) dx \quad (3.4)$$

where, $EI = Ect^3/12(1 - \nu^2)$ and primes indicate differentiation with respect to x .

3.1.3 Membrane energy

Along with bending energy, face plates are also subjected to membrane action. Unlike the previous model (Hunt and Wadee 1998), axial strains include global and local contributions for both face plates, as shown below:

$$\varepsilon_{xt} = -\frac{b}{2}\theta' - \Delta + \frac{1}{2}w_t'^2 + u_t' \quad (3.5a)$$

$$\varepsilon_{xb} = \frac{b}{2}\theta' - \Delta + \frac{1}{2}w_b'^2 + u_b' \quad (3.5b)$$

where u_b , u_t , w_b and w_t are all functions of x only given on the right hand side of the expressions in Equations 3 and 3.4. The nonlinear terms for each face plate arise from Von Kármán plate theory. Hence the membrane energy is assembled as follows:

$$\begin{aligned} U_m &= D \int_0^L (\varepsilon_{x,t}^2 + \varepsilon_{x,b}^2) dx, \\ &= D \int_0^L \left[2\Delta^2 + \frac{1}{2}b^2\theta'^2 + u_t'^2 + u_b'^2 + \frac{1}{4}(w_t'^4 + w_b'^4) \right. \\ &\quad \left. + (b\theta' - 2\Delta) \left(u_b' - u_t' + \frac{1}{2}w_b'^2 - \frac{1}{2}w_t'^2 \right) + u_t'w_t'^2 + u_b'w_b'^2 \right] dx \end{aligned} \quad (3.6)$$

where $D = Ect/2$.

3.1.4 Core strain energy

As in the 1998 model (Hunt and Wadee 1998), the strain energy stored in the core, U_c is derived from considering shear and transverse strains only, whereas the longitudinal strains are omitted for simplicity. This derives from the assumption that the core is soft and hence the strain energy stored in the system is very small compared to the face plate membrane energy. A subsequent model presented in Wadee and Hunt (1998), which accounted for the longitudinal strain energy in the core, had an overall buckling critical load less than 1% different from the current formulation, while the position of the secondary bifurcation and interactive buckling deformations were virtually identical. It was thus deemed appropriate to neglect the contributions of the direct longitudinal strains from the core strain energy, reducing the complexity of the model is reduced, without losing significant accuracy.

$$U_c = \frac{1}{2} \int_0^c \int_{-b/2}^{b/2} \int_0^L \left(\frac{E_c}{1-\nu^2} \varepsilon_y^2 + G_c \gamma_{xy}^2 \right) dx dy dz \quad (3.7)$$

where $G_c = E_c/[2(1 + \nu_c)]$ and

$$\varepsilon_y = \frac{w_t(x) + w_b(x)}{b} \quad (3.8)$$

$$\gamma_{xy} = W'(x) - \theta(x) + \left(\frac{b+2y}{2b} \right) w'_t(x) + \left(\frac{b-2y}{2b} \right) w'_b(x) + \frac{u_t - u_b}{b} \quad (3.9)$$

The core strain energy can be readily integrated over the breadth and depth of the core, resulting in an integral over the length. Thus:

$$\begin{aligned}
 U_c = \int_0^L \left\{ G \left[\frac{w_t'^2 + w_b'^2 + w_t'w_b'}{3} + \frac{u_t w_b' + u_t w_t' - u_b w_b' - u_b w_t'}{b} \right. \right. \\
 \left. \left. + \frac{u_t^2 + u_b^2 - 2u_t u_b}{b^2} + (W' - \theta) \left(w_t' + w_b' - \frac{2}{b}(u_b - u_t) \right) + (W' - \theta)^2 \right] \right. \\
 \left. + \frac{1}{2} k (w_t - w_b)^2 \right\} dx
 \end{aligned} \tag{3.10}$$

where $G = G_c bc/2$ and $k = E_c c/[b(1 - \nu_c^2)]$.

3.1.5 Work done by applied load

The work done by the external force is the product of the applied load P , multiplied by the total displacement \mathcal{E} at the point of application, i.e. at the mid-plane of the strut. The procedure for obtaining the total displacement at the point of application has been described in Yiatros et al (2013). For the kinematic variables in the current model, the work done by the external force has the form:

$$P\mathcal{E} = P \int_0^L \left[\frac{1}{2} W'^2 + \Delta - \frac{1}{2} (u_t' + u_b') \right] dx, \tag{3.11}$$

where the first term is the contribution from the overall buckling lateral displacement W if the strut is inextensional. The second term arises due to the uniform compressive strain Δ which gives the non-trivial pre-buckling end shortening. The remaining terms are contributions of the localized displacement components u_t and u_b of the top and bottom face plates within the core. The contribution due to these components is from the relative movement at the two end-points.

3.1.6 Total potential energy, critical load and equilibrium equations

The total potential energy V of the strut is obtained by summing all the energy contributions, such as:

$$\begin{aligned}
 V &= U_b + U_m + U_c - P\mathcal{E}, \\
 &= \int_0^L \left\{ \frac{EI}{2} \left(2q_s^2 \frac{\pi^4}{L^2} \sin^2 \frac{\pi x}{L} + w_t'^2 + w_b'^2 \right) \right. \\
 &\quad + \left[\frac{1}{2} b^2 \frac{q_t^2 \pi^4}{L^2} \sin^2 \frac{\pi x}{L} + 2\Delta^2 + u_t'^2 + u_b'^2 + \frac{1}{4} (w_t'^4 + w_b'^2) + u_t' w_t'^2 + u_b' w_b'^2 \right. \\
 &\quad \left. \left. + \left(\frac{q_t b \pi^2}{L} \sin \frac{\pi x}{L} - 2\Delta \right) \left(u_b' - u_t' + \frac{1}{2} w_b'^2 - \frac{1}{2} w_t'^2 \right) \right] \right. \\
 &\quad + G \left[(q_s - q_t)^2 \pi^2 \cos^2 \frac{\pi x}{L} + \frac{1}{3} (w_t'^2 + w_b'^2 + w_b' w_t') \right. \\
 &\quad + (q_s - q_t) \left(w_t' w_b' + \frac{2u_t - 2u_b}{b} \right) \pi \cos \frac{\pi x}{L} + \frac{u_t^2 + u_b^2 - 2u_b u_t}{b^2} \\
 &\quad \left. \left. + \frac{u_t w_b' + u_t w_t' - u_b w_b' - u_b w_t'}{b} \right] + \frac{1}{2} k (w_t + w_b)^2 \right. \\
 &\quad \left. - P \left(\frac{1}{2} q_s^2 \pi^2 \cos^2 \frac{\pi x}{L} - \frac{1}{2} u_t' - \frac{1}{2} u_b' + \Delta \right) \right\} dx.
 \end{aligned} \tag{3.12}$$

Note that by setting all w_t and u_t terms and their derivatives to zero, the potential energy functional becomes identical to the 1998 model. Hence the critical load for overall buckling, given in Eq. 3.13 remains the same as in (Hunt and Wadee 1998):

$$P^C = \frac{2\pi^2 EI}{L^2} + \frac{Gb^2 \pi^2}{L^2} \left[\frac{2D}{2G + Db^2 \pi^2 / L^2} \right]. \tag{3.13}$$

The governing nonlinear equations of equilibrium are found by minimizing the total potential energy functional. For the system to be in equilibrium, the total potential energy has to be stationary with respect to the functions w_b , w_t and u_t along with the generalized coordinates q_s , q_t and Δ . The station-

ary points of the functional are computed through a hybrid formulation: the calculus of variations (Fox 1987) is used for computing the stationary points with respect to the unknown functions w_b , w_t , u_b , u_t , whereas the stationary points with respect the generalized coordinates are computed as in the classical Rayleigh Ritz method by setting the partial derivatives of the energy functional with respect to q_s , q_t and Δ to zero. This leads to four nonlinear ordinary differential equations (ODEs) that are 4th order with respect to w_t and w_b and 2nd order with respect to u_t and u_b , plus three integral constraints, given in Eqs. 3.14 - 3.20 :

$$\begin{aligned}
 EIw_b'''' + D \left[2\Delta w_b'' + q_t \frac{b\pi^2}{L} \left(\sin \frac{\pi x}{L} w_b'' + \frac{\pi}{L} \cos \frac{\pi x}{L} w_b' \right) \right. \\
 \left. - 3w_b'^2 w_b'' - 2w_b'' u_b' - 2w_b' u_b'' \right] + G \left[\frac{u_b' - u_t'}{b} - \frac{2w_b'' + w_t''}{3} \right. \\
 \left. + (q_s - q_t) \frac{\pi^2}{L} \sin \frac{\pi x}{L} \right] + k(w_b - w_t) = 0,
 \end{aligned} \tag{3.14}$$

$$\begin{aligned}
 EIw_t'''' + D \left[2\Delta w_t'' + q_t \frac{b\pi^2}{L} \left(\sin \frac{\pi x}{L} w_t'' + \frac{\pi}{L} \cos \frac{\pi x}{L} w_t' \right) \right. \\
 \left. - 3w_b'^t w_t'' - 2w_t'' u_t' - 2w_t' u_t'' \right] + G \left[\frac{u_b' - u_t'}{b} - \frac{2w_t'' + w_b''}{3} \right. \\
 \left. + (q_s - q_t) \frac{\pi^2}{L} \sin \frac{\pi x}{L} \right] + k(w_t - w_b) = 0,
 \end{aligned} \tag{3.15}$$

$$u_b'' + w_b' w_b'' - \frac{b\pi^3 q_t}{2L^2} \cos \frac{\pi x}{L} + \frac{G}{Db} \left(\frac{u_t - u_b}{b} + \frac{w_t' + w_b'}{2} + (q_s - q_t) \pi \cos \frac{\pi x}{L} \right) = 0, \tag{3.16}$$

$$u_t'' + w_t' w_t'' - \frac{b\pi^3 q_t}{2L^2} \cos \frac{\pi x}{L} + \frac{G}{Db} \left(\frac{u_b - u_t}{b} + \frac{w_b' + w_t'}{2} + (q_s - q_t) \pi \cos \frac{\pi x}{L} \right) = 0, \tag{3.17}$$

$$P = \frac{2G}{q_s} \left\{ \int_0^L \left[\left(w_b' + w_t' - \frac{2u_b - 2u_t}{b} \right) \cos \frac{\pi x}{L} \right] dx \right\} + \frac{2EI\pi^2}{L^2}, \tag{3.18}$$

$$q_s = q_t \left(1 + \frac{Db^2\pi^2}{2GL^2} \right) + \int_0^L \left[\frac{1}{\pi L} \left(\frac{2u_b - 2u_t}{b} - w'_b - w'_t \right) \cos \frac{\pi x}{L} - \frac{Db}{GL^2} \left(u'_b - u'_t + \frac{w_b'^2}{2} - \frac{w_t'^2}{2} \right) \sin \frac{\pi x}{L} \right] dx, \quad (3.19)$$

$$\Delta = \frac{P}{4D} + \frac{1}{2L} \int_0^L \left(u'_t + u'_b + \frac{1}{2}w_b'^2 + \frac{1}{2}w_t'^2 \right) dx. \quad (3.20)$$

The governing equations are subject to the following boundary conditions that minimize V :

$$w_b(0) = w_b(L) = w_b''(0) = w_b''(L) = 0, \quad (3.21)$$

$$w_t(0) = w_t(L) = w_t''(0) = w_t''(L) = 0, \quad (3.22)$$

$$u'_b(0) + \frac{1}{2}w_b'^2(0) - \Delta = u'_t(0) + \frac{1}{2}w_t'^2(0) - \Delta = -\frac{P}{4D}, \quad (3.23)$$

$$u'_b(L) + \frac{1}{2}w_b'^2(L) - \Delta = u'_t(L) + \frac{1}{2}w_t'^2(L) - \Delta = -\frac{P}{4D}, \quad (3.24)$$

which ensure simple supports for face plates and matching in-plane stresses at both ends.

3.2 Nonlinear stability analysis

In order to establish the non-trivial interactive modes, the system of governing ordinary differential equations, integral constraints and boundary conditions was nondimensionalized and solved using AUTO (Doedel et al 2012), the powerful numerical continuation software with the ability to trace evolving solutions with parametric changes, identify bifurcation points and trace paths. The selected leading parameter —usually P in the current case— is varied and AUTO solves for the remaining parameters (q_s , q_t and D) as well as the unknown functions and their derivatives. The investigation of buckling mode interaction is conducted for the cases where either overall or local buckling is critical. The selected leading parameter is varied from zero along the

fundamental path until a bifurcation point is found. The load parameter in AUTO is normalized with respect to the overall buckling load, so that when overall buckling is critical, $p = P/P_o^C = 1$. A second run is then performed from the primary bifurcation until the secondary bifurcation, beyond which interactive buckling is triggered in the bottom—more compressed—face plate, while simultaneously, deformations begin to appear at the top face plate. In the next few subsections some key results from the analysis described above are presented and discussed.

3.2.1 Results

A typical sandwich strut configuration comprising stiff aluminum alloy plates and a polymeric compliant foam was used. The material and geometrical properties are given below:

Face plate Young's modulus	:	$E = 68947.57 \text{ Nmm}^{-2}$
Face plate Poisson's ratio	:	$\nu = 0.3$
Core Young's modulus	:	$E_c = 198.57 \text{ Nmm}^{-2}$
Core Poisson's ratio	:	$\nu_c = 0.2$
Core shear modulus	:	$G_c = 82.74 \text{ Nmm}^{-2}$
Face plate thickness	:	$t = 0.50 \text{ mm}$
Core thickness	:	$b = 5.08 - 18.00 \text{ mm}$
Length of the structure	:	$L = 100.0 - 200.0 \text{ mm}$

The same material properties and some of the geometric ones have been used in earlier relevant publications (Hunt et al 1988; Hunt and Wadee 1998) and are also used currently for comparison purposes. The materials are considered to be linearly elastic for the ranges of strains studied. The geometric properties were selected to include cases of criticality of the overall mode and others of the local (face plate) modes.

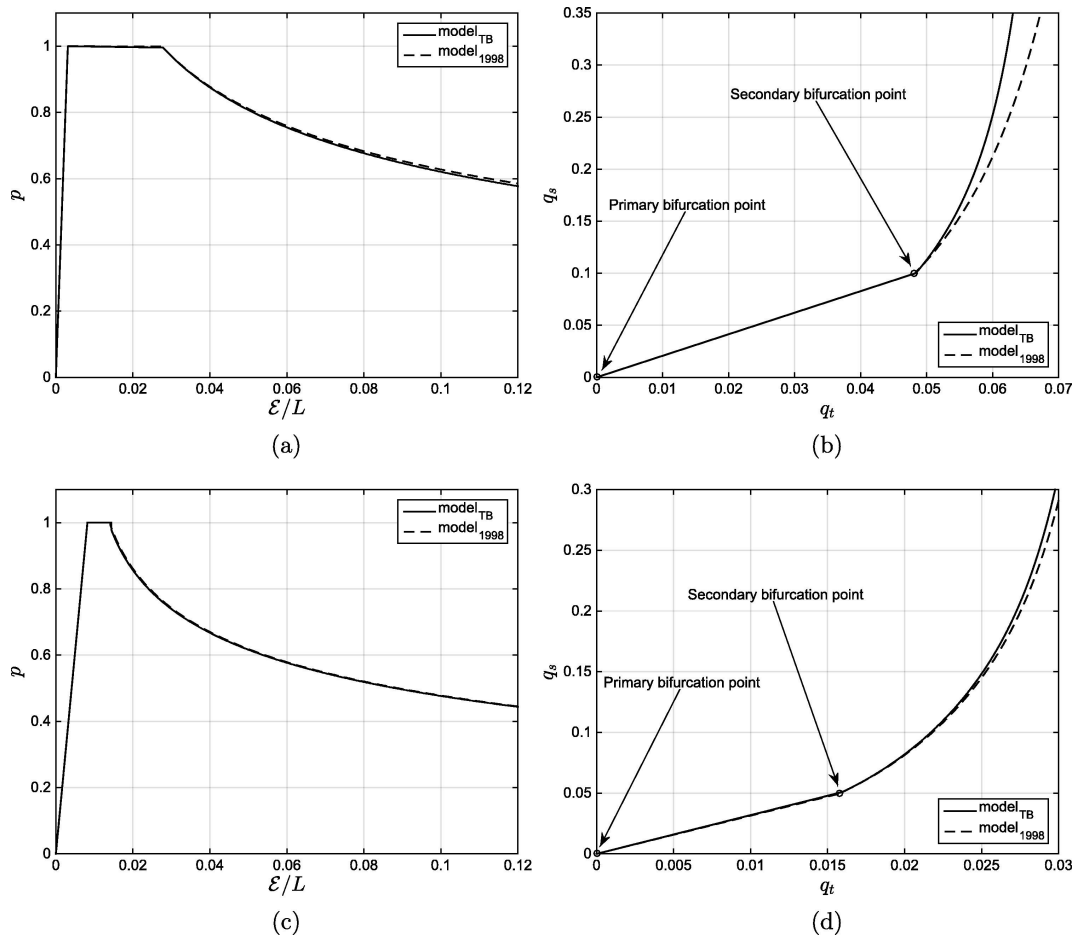


Figure 3.2: Left: plotting p versus normalized end shortening (\mathcal{E}/L). Right: plotting amplitude of tilt q_t versus amplitude of sway q_s for struts of length $L = 100\text{mm}$ and different core depths. $b = 5.08\text{mm}$ for (a) and (b) and $b = 10.16\text{mm}$ for (c) and (d)

Considering the first strut, where $b = 5.08\text{mm}$ and $L = 100\text{mm}$. In this case overall buckling is critical once the secondary bifurcation is located and the strut subsequently destabilizes, rapidly losing its load carrying capacity as seen in Figure 3.2(a). It can be seen that by comparing the two models, no significant differences can be observed in the post-buckling unloading response beyond the secondary bifurcation. Some very minor differences can be seen in Figure 3.2(c), which depicts the response of a sandwich strut of core depth $b = 10.16\text{mm}$ and length $L = 100\text{mm}$. In both instances, the new model (thereafter termed 'modelTB') has a marginally steeper post-buckling but,

nonetheless, following the same unloading trend. A slightly more measureable difference beyond the critical (primary) bifurcation is visible when comparing the tilt and sway components of the overall mode directly, as shown in Figures 3.2(b) and 3.2(d). These differences, however small, are attributed to the formation of local deformations occurring at the top (less compressed) face plate, which were inhibited within the 1998 model. As seen in Figure 3.3, which exhibits the evolution of interactive modes w_b ; w_t ; u_b ; u_t with P unloading, as soon as the interactive localized buckle appears within the more compressed face plate, a quasi-periodic buckle pattern appears in the other. The top face plate deformation begins for all configurations as a shallow negative displacement, flattening the top face plate at mid-span and down the post-buckling path, two more half sine waves begin appearing at the two ends. These diagrams show the nature, as well as the comparative magnitude, of the interactive modes. The first observation is that the modes corresponding to the top face plate are smaller in magnitude compared to the ones corresponding to the bottom face plate. This can be attributed to the fact that the localized interactive buckling displacement occurring within the bottom face plate is a signature of a destabilizing phenomenon and hence grows faster during unloading. The displacement w_t , however small, contributes to the flattening of the top face plate during post-buckling (Figure 3.4). Parametric studies, while keeping the core depth constant, demonstrate that with increasing length the periodicity in the deformations of the top face plate is maintained, albeit with an increasing number of half sine waves and diminishing growth, as shown in Figure 3.5. This is expected since with increasing length, more half sine waves would be generated in the most energetically favorable buckle pattern. The amplitude of the less compressed face plate local deformations does not change with increasing length at different levels of load P . These local deformations are independent of the localized mode that manifests in the more compressed face plate, as shown in Equations and 3.3. Moreover they have a different

wavelength and their amplitude is uniform, unlike the localized mode which is concentrated at midspan. A further parametric study, performed by investigating the amplitude and nature of deformations for different sandwich depths at constant levels of load, P , exhibited an insensitivity to the amplitude of the less compressed face plate deformations, maintaining a constant local displacement amplitude to depth ratio. Conversely, the interactive mode in the more compressed face plate becomes more localized with increasing depth, for the different depths ($5.08\text{--}14\text{mm}$). As the load rapidly decreases during post-buckling, local plate buckling at the top does not grow and its effect is quickly diminished due to the tensile stresses from bending introduced by the overall buckling component.

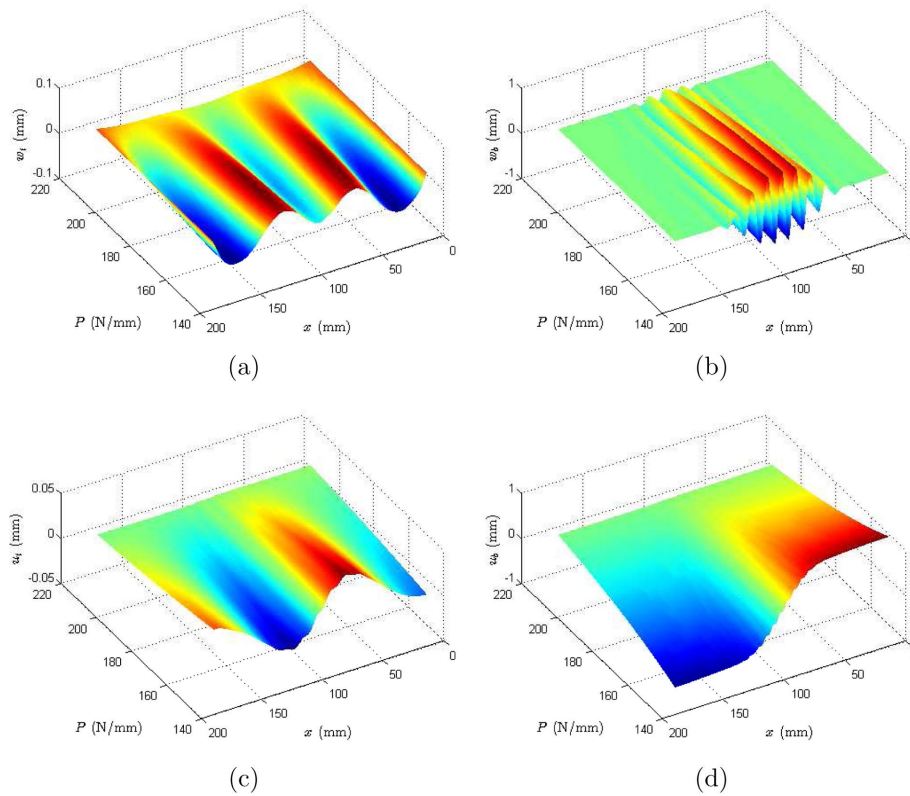


Figure 3.3: (a) Local mode evolution of face plates unloading for strut of length $L = 175\text{mm}$ and core depth $b = 5.08\text{mm}$. (a) w_t (b) w_b , (c) u_t and u_b .

An important feature of the model presented herein is that it enables the investigation of interactive localized buckling when local buckling occurs first.

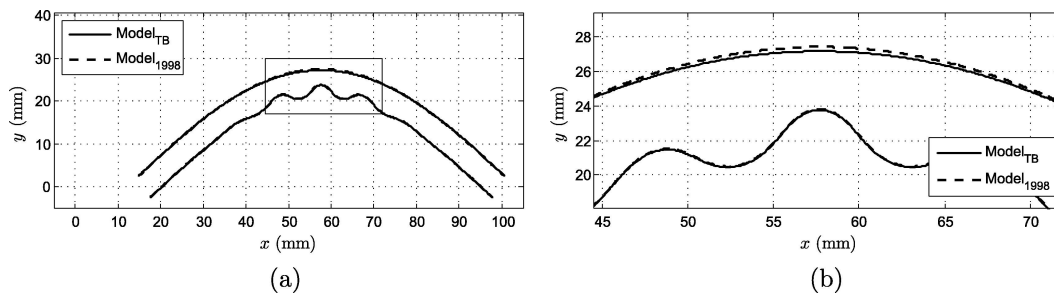


Figure 3.4: (a) The overall buckling on a $b = 5.08\text{mm}$ and $L = 100\text{mm}$ strut at $p = 0.7$. (b) A close look at midspan deformations. While the bottom face plate deformations are easily observed, the top face plate local deformations are not as clear but contribute to the flattening of the top face plate.

The second case considers deeper struts where local buckling becomes critical. Example struts of length $L = 100\text{mm}$ with depths $b = 16$ and 18mm are analyzed. Since the load parameter is normalized with respect to the overall critical load, the primary bifurcations are, in all cases, found to be close to, but below, $p = 1$; specifically p is critical at 0.94 and 0.92 for $b = 16\text{mm}$ and $b = 18\text{mm}$ respectively. An interesting feature compared to the case where the overall mode is critical, is the continued close proximity of the primary (local mode) and secondary (overall mode) bifurcation. Owing to the close proximity of the two bifurcations, the solver jumped from the primary (local) bifurcation to interactive buckling beyond the secondary bifurcations, thus not revealing the nature (symmetric/antisymmetric) of the local mode that was triggered first. The system subsequently exhibiting a steep destabilizing post-buckling response as the interactive mode is initiated, as observed in Figure 3.6. The confinement and growth in amplitude of the localized mode in the bottom face plate, as well as the top face plate deformations, lead to a steeper postbuckling response and sudden loss of the load carrying capacity. It has to be noted that these interactive modes cannot be captured by the 1998 model since it does not account for local deformation on both face plates and hence it could not account for the case where local buckling is critical very accurately. However, an attempt was made in Wadee (2000) to model pure local buckling assuming a mode where the bottom plate deflected with a purely periodic profile; similar

findings were made, where the gap between triggering local buckling and then interactive buckling was very small for all geometries that were considered. More differences can be found when examining the mode shapes more closely, the interactive mode observed within the more compressed face plate remains confined to the midspan as the post-buckling response evolves, exhibiting a higher modulation of the main wave, further down the path. This can be attributed to the softer nature of the strut that has a deeper core. On the other hand, local face plate displacements are seen within the top face plate, initially as a sizable negative displacement at midspan of similar amplitude to the localized mode, which then tends to be quasi-periodic, without growing as fast as the localized mode (Figure 3.7).

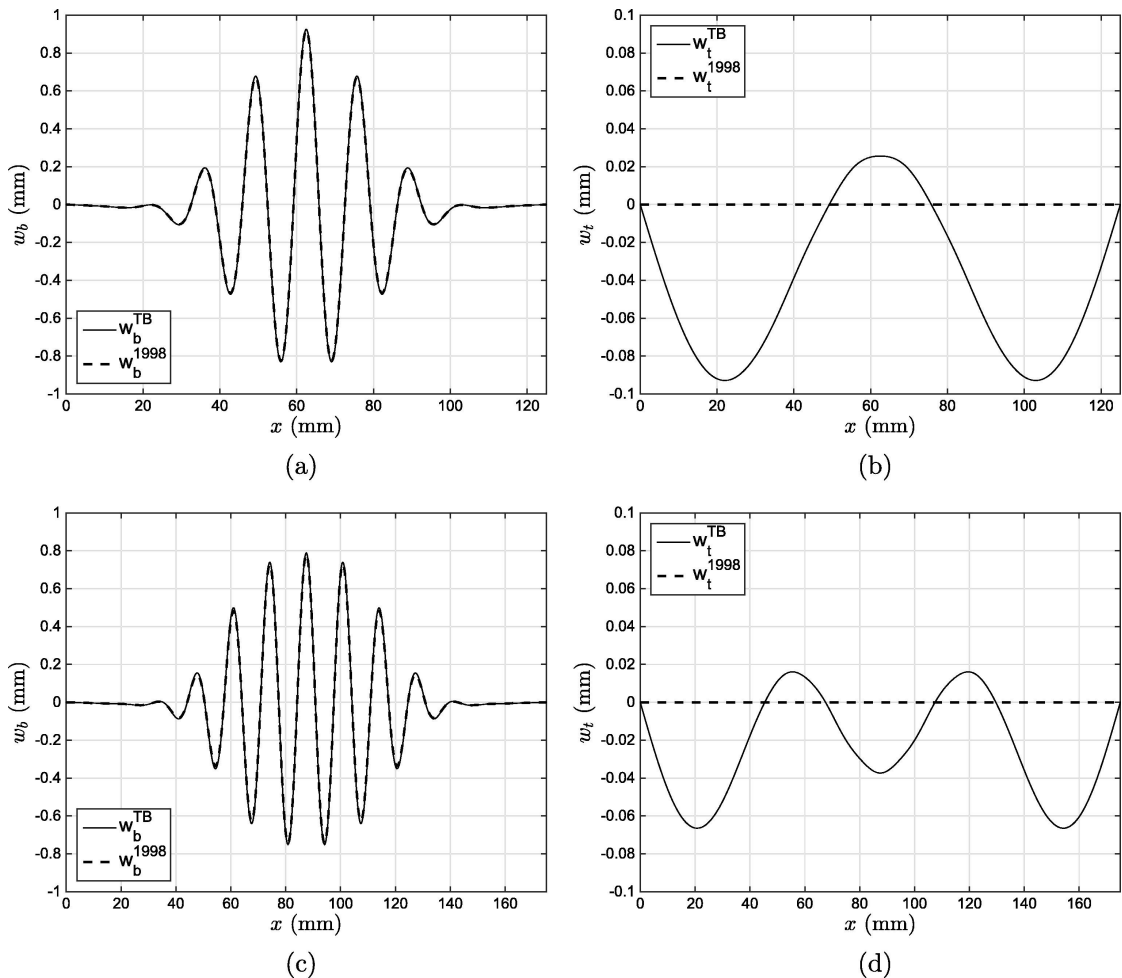


Figure 3.5: Both face plate local displacements for depth $b = 5.08$ mm. Length $L = 125$ mm for (a-b) and $L = 175$ mm for (c-d). All are shown at $p = 0.7$.

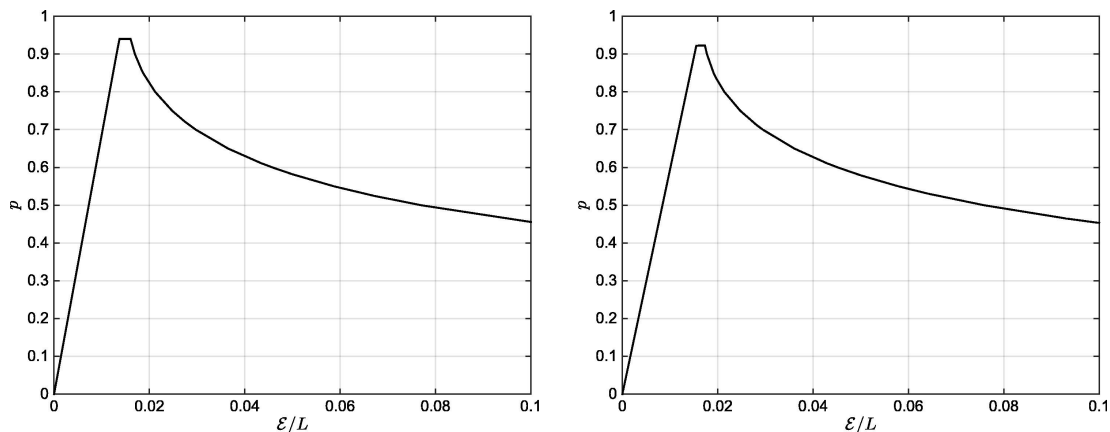


Figure 3.6: Equilibrium paths for struts with length $L = 100mm$ and core depth (a) $b = 16mm$, or (b) $b = 18mm$. The \mathcal{E}/L gap between the primary and secondary bifurcation points is 0.0024 and 0.0018 for $b = 18mm$.

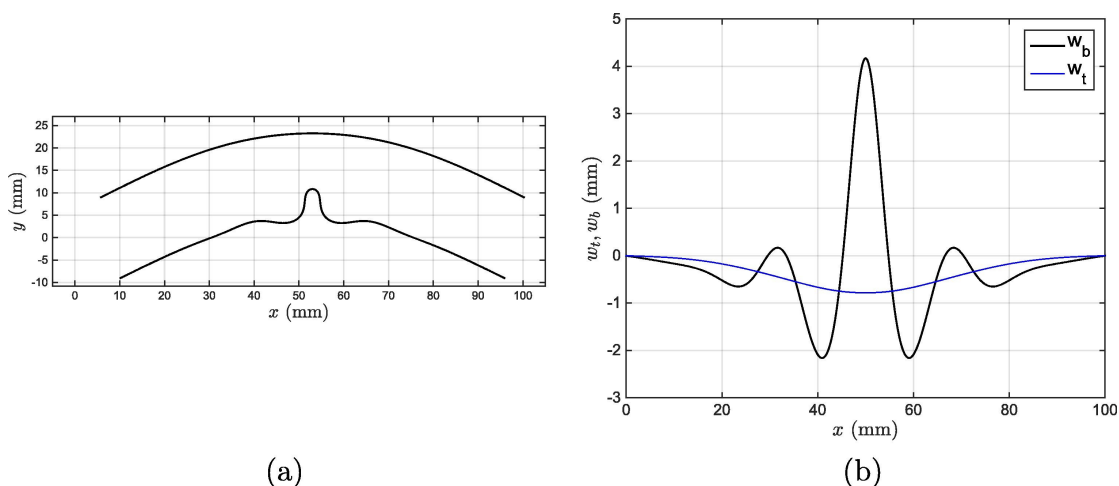


Figure 3.7: (a) Interactive mode deformation profile for strut of length $L = 100mm$ and core depth $b = 16mm$. (b) Local modes within the top and bottom face plate at $\mathcal{E}/L = 10\%$ within the interactive post-buckling range.

3.3 Conclusions

A variational formulation based on potential energy principles accounting for interactive buckling in sandwich struts has been presented. The model builds on the fundamental work by Hunt and Wadee (1998) and captures local quasi-periodic deformations within the top, less compressed, face plate in the post-buckling range. The deformations in the less compressed face plate have a different wavelength to the interactive buckle in the more compressed face plate; both grow with progressive unloading in the postbuckling range, but the deformations in the less compressed face plate are always significantly smaller in amplitude than the localized interactive mode that dominates the response. Indeed, the dominance of the interactive buckling mode is highlighted by the minimal difference in the equilibrium paths, showing that the local deformations in the less compressed face plate play a negligible influence in the mechanical response of the sandwich strut, for the thickness considered and where overall buckling was critical. More importantly for the current discussion, however, the model is capable of dealing with the case where local buckling is critical. This case exhibits a very close proximity between the primary and secondary bifurcations and a severely unstable response is the result, which would translate into a high degree of imperfection sensitivity (Wadee 2000).

Chapter 4

Modelling interactive buckling for FGM sandwich struts

In Chapter 3, a nonlinear analytical model to investigate localized interactive buckling in simply supported thin-face plate sandwich struts with weak core was extended to account for local deformations in both face plates. The results indicated that the local deformations in the less compressed face plate play negligible influence in the overall mechanical response of the sandwich strut during interactive buckling, while the real merits of the model is when investigating the cases where the local mode is critical. Sandwich construction boasts its advantage over homogeneous construction methods due to its optimized configuration which assigns material and stiffness where it is most effective, thus reducing the cost and weight of the structural element. This optimisation could be enhanced further with the use of functionally graded materials in sandwich construction. Functionally graded materials have properties that vary continuously, either by varying their density or their chemical composition.

In this chapter an introduction to functionally graded materials is pre-

sented. This is followed by review of available methodologies for analysing functionally graded materials, before moving to the analytical modelling of interactive buckling in sandwich struts with functionally graded core.

4.1 Functionally graded core materials

Functionally graded materials (FGMs) are materials or structures in which the material properties vary with location in such a way as optimize some function of the overall FGM. Nature provides many examples of functionally graded materials. In many of the cases the nature at functionally graded structures were evolved based on some mechanical function: bones give a light, stiff frame to the body, wood supports the tree under environmental loadings, leaves transport fluids. Bamboo is one of the examples of structurally smart plant (Amanda et al 1997). Bamboo structure, which resembles that of a unidirectional, fiber-reinforced composite, is described by a macroscopically graded geometry that is adapted to environmental wind loads while the fiber distribution exhibits a microscopically graded architecture, which leads to smart properties of bamboo. Amanda et al (1997) demonstrated experimentally and analytically how the functionally graded microstructure of a bamboo has been optimized through evolution to maximize its load bearing capabilities under environmental loading conditions.

The concept of functionally graded materials was proposed in the 80s by materials scientists in Japan as a way to create thermal barrier materials. Koizumi (1997) summarized the first projects in this field. The idea proposed was to combine in a gradual manner heat-resistant ceramics and tough metals with high thermal conductivity. The result is a panel with a high heat-resistance on the high-temperature side and high mechanical strength on the other side. The new materials were obtained by four methods: Chemical Va-

por Deposition (CVD), powder metallurgy, plasma sprays and self propagating combustion synthesis (SHS).

As the use of FGMs increases, new methodologies have to be developed to characterize FGMs, and also to design and analyze structural components made of these materials. Although fabrication technology of FGMs is in its infancy, they offer many advantages. Few of the manufacturing methods are presented here. Fukui (1991) developed a high-speed centrifugal casting method, in which the layers are formed in the radial direction due to different mass densities. An melted Al-Ni alloy cast into a thick-walled tube was rotated at a speed such that the molten metal experienced an acceleration, thereby producing two kinds of composition gradient. El-Hadek and Tippur (2003) developed functionally graded syntactic foam sheets by dispersing micro balloons (with linear graded volume fraction) in epoxy. They determined Young's modulus and the density by using the wave speed and density for syntactic foams having homogenous dispersion of the micro balloons. The resulting foam sheets have a nearly constant Poisson's ratio. Other FGM manufacturing methods presented in literature are powder metallurgy, plasma sprays and self-propagating combustion synthesis.

4.2 Sandwich structures with FGMs

Sandwich structures have many benefits such as their low-weight and high bending stiffness and thus have been broadly applied in aircraft, aerospace, flexible electronics, and biomedical areas (Birman and Kardomateas 2018). The introduction of inhomogeneous materials, such as functionally graded materials, has made the sandwich structures become even more attractive (Garg et al 2021). As options for either face plates and/or the core, FGMs can play a functional role as sandwich components, by helping reduce interlaminar

stresses and thermal stresses, enhancing the mechanical and thermal performances of sandwich structures (Jha et al 2013; Swaminathan et al 2015). Two types of FGM sandwich structures are mainly seen: sandwich structures with FGM face plates and a homogeneous core, and sandwich structure with homogeneous face plates and FGM core.

More relevant to the scope of work herein the sandwich panels with functionally graded cores where the stiffness in the core varies in the transverse direction by gradually changing the mechanical properties of the core materials. Functionally grading the core properties can provide further advantages to sandwich construction, such as the increase of critical loads, but it can also address specific localized phenomena such as delamination and fracture due to impact (Anderson 2003). The interest here is to see whether particular stiffness functional gradations, could be used as part of a design mitigation strategy to delay or ameliorate buckling.

In terms of the structural analysis of functionally graded sandwich panels, the literature focuses on the application of mechanical and thermal loads (Samsam Shariat et al 2005; Zenkour 2005; Zhu and Sankar 2007), with special attention to the change in the response brought by the gradation. It has been shown that the risk of delamination due to high interfacial shear stresses is minimized if the stiffness of the weaker part is locally increased (Venkataraman and Sankar 2003; Anderson 2003). The increasing stiffness near the interface also results in an increase of the wrinkling (local buckling) critical load (Ávila 2007) as well as contributing in reducing electric displacement intensity factors in piezoelectric FGMs (Li and Weng 2002).

The accurate modelling of sandwich FGMs has been of great interest to many researchers leading to the proposal of several approaches from simpler

Equivalent Single Layer (Reissner 1945; Reddy 1984) to Layer-wise (Cho et al 1991) and Carrera's unified formulation (Carrera et al 2008); the approaches listed currently are in order of increasing complexity. Apetre et al (2008), compared two Equivalent Single layer approaches with a Higher Order (Frostig et al 1992) and a Fourier-Galerkin (Zhu and Sankar 2007) showing that the two approaches correlate much better with an FE simulation used for comparisons, at the expense of increased computational cost. The reason lies in the fact that both approaches rely in the solution of the elasticity equations without making any assumptions about the through-depth in-plane displacements, unlike the Equivalent Single Layer approaches which are based on the same assumptions as the TBT and RBT models presented in this thesis. On similar grounds, Brischetto (2009) also suggested the use of higher order theories in the cases of thick plates or large gradients.

The stability of FGMs has also been investigated in terms of compression (Feldman and Abudi 1997) and thermal buckling including (Samsam Shariat and Eslami 2007; Javaheri and Eslami 2002) some postbuckling (Shen and Li 2008; Ke et al 2009) and vibration analysis (Yang et al 2006; Park and Kim 2006). Since these have been mostly on the stability of plates, postbuckling work is yet to be seen on the onset of interactive buckling and localization of sandwich panels with FGM cores. This has been shown to destabilize the neutrally stable postbuckling of sandwich struts and its effects are magnified in the presence of eccentric load (Yiatros and Wadee 2011) or geometrical imperfections (Wadee 2000) as seen in part from in the earlier chapters. It is for reason that the current of FGM sandwich panels under the influence of an axial load for various graded combinations.

4.3 Analytical modelling

In this section, the two models TBT and RBT presented in Chapter 2,

predicting interactive buckling in sandwich struts are adapted in a pilot study to account for cores made from a functionally graded material. Currently, both models account for homogeneous orthotropic materials where the material properties vary in two orthogonal directions. In the current modelling, core properties are considered to be graded continuously in the transverse direction, y , using the gradation function presented in Equation 4.1.

$$X(y) = X_C \left[a_0 + a_1 \frac{y^2}{b^2} + a_2 \frac{y^4}{b^4} + a_3 \frac{y^6}{b^6} + a_4 \frac{y^8}{b^8} \right], \quad (4.1)$$

where, X_C is the base material property, such as Young's modulus or Shears modulus, while X gives the value of the property at position y in the transverse direction. The parameters a_0, \dots, a_4 denote the material constants and the nature of the gradation, as seen in Figure (4.1). When the parameters a_1, \dots, a_4 are set to zero the distribution of material properties is constant through the depth of the core. Selecting polynomial gradation allows the investigation of different gradations modes. Two distinct distributions with different gradations modes are investigated. When the gradation is concave, the material property is minimum at the neutral axis and increases further away from it, and when the gradation is convex, the material property is maximum at the neutral axis and reduces further way from it.

The analytical models are based on the Total Potential Energy principle, as described in the earlier chapters. Given that only the core is assumed to be made from FGM, the strain energy of the face plates remains unchanged and the same applies for the work done by the axial force. The difference in the core is that previously, the material property terms were treated as constants. In the current modelling procedure, the material property terms are inside the integral since they vary across the depth of the strut. The potential energy functionals for both TBT and RBT models are presented next.

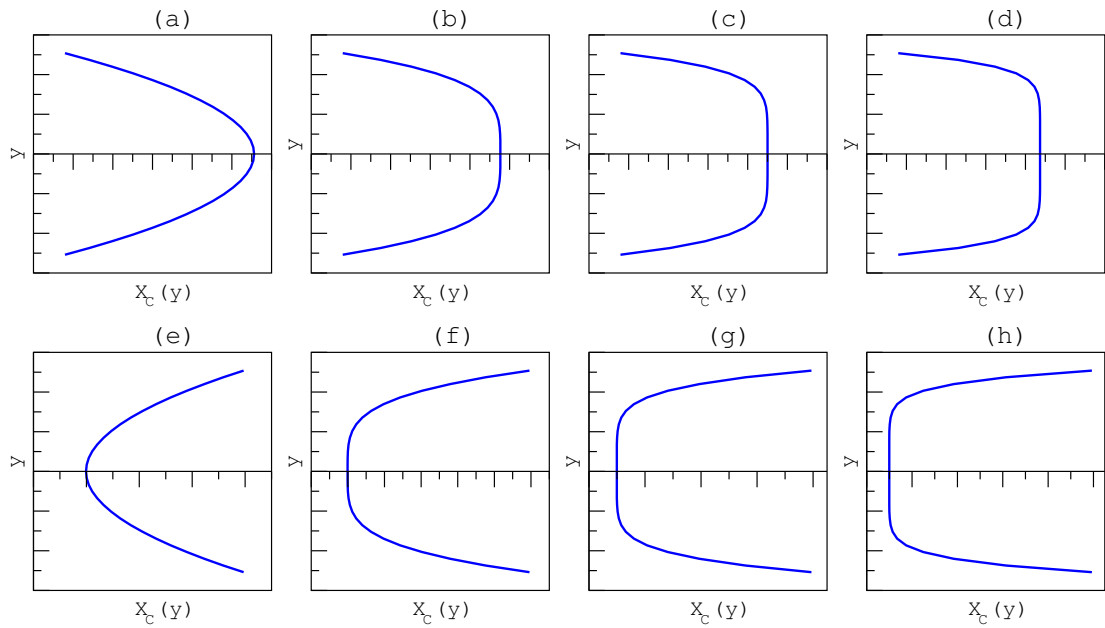


Figure 4.1: The variation in material properties through the depth of the core. (a)-(d) Convex: From left to right (a) $a_0 > 0, a_1 > 0$; (b) $a_0 > 0, a_2 > 0$; (c) $a_0 > 0, a_3 > 0$; (d) $a_0 > 0, a_4 > 0$. (e)-(h) Concave: From left to right (e) $a_0 > 0, a_1 < 0$; (f) $a_0 > 0, a_2 < 0$; (g) $a_0 > 0, a_3 < 0$; (h) $a_0 > 0, a_4 < 0$. When $a_1..a_4 = 0$ the distribution of material properties is constant through the depth of the strut.

4.3.1 Strain energy

Bending Energy

The first component of this strain energy comes from the strain induced in the two face plates bending about their local minor axis and contains contributions from both global and local curvature and is stated in Equation 2.8 .

Membrane Energy

The second component is the strain energy arising from the axial strains in the face plates. These strains are developed from the initial squashing and the subsequent bending due to buckling and is stated in Equation 2.11. For TBT the Membrane Energy given as :

$$\begin{aligned}
U_{m,T} = \int_0^L \left\{ D \left[2\Delta^2 + \frac{\dot{w}^4}{4} + q_t^2 \frac{\pi^4 \phi^2}{2} \sin^2 \frac{\pi x}{L} \right. \right. \\
\left. \left. + \dot{u}^2 + \dot{u}\dot{w}^2 - q_t \pi^2 \phi \left(\dot{u} + \frac{\dot{w}^2}{2} \right) \sin \frac{\pi x}{L} - 2\Delta \left(\dot{u} + \frac{\dot{w}^2}{2} \right) \right] \right\} dx
\end{aligned} \quad (4.2)$$

For RBT the Membrane Energy given as :

$$\begin{aligned}
U_{c,R} = \int_0^L \left\{ D \left[2\Delta^2 + \frac{\dot{w}^4}{4} + (2q_t + q_s)^2 \frac{\pi^4 \phi^2}{18} \sin^2 \frac{\pi x}{L} \right. \right. \\
\left. \left. + \dot{u}^2 + \dot{u}\dot{w}^2 - (2q_t + q_s) \frac{\pi^2 \phi}{6} \sin \frac{\pi x}{L} \left(2\dot{u} + \dot{w}^2 \right) - 2\Delta \left(\dot{u} + \frac{\dot{w}^2}{2} \right) \right] \right\} dx
\end{aligned} \quad (4.3)$$

Core Energy

As stated in Chapter 2, the strain energy stored in the core has three sources: axial, transverse and shear strains. Equation 2.21 gives the basic expression for the core energy, which recast to describe FGM core as the following expressions. For TBT the Core Energy given as :

$$\begin{aligned}
U_{c,T} = \int_0^L \left\{ C_x \left[\frac{\dot{w}^4}{20} f_5 + \frac{\dot{u}^2}{3} f_2 + \frac{\dot{w}^2 \dot{u}}{4} f_4 - \Delta \left(\dot{u} f_1 + \frac{\dot{w}^2}{3} f_2 - \Delta f_1 \right) \right. \right. \\
\left. \left. + \frac{q_t \phi}{12} f_3 \pi^2 \sin \frac{\pi x}{L} \left(q_t \pi^2 \phi \sin \frac{\pi x}{L} - \dot{w}^2 - 2\dot{u} \right) \right] \right. \\
\left. + C_y \left[\Delta \nu_x^2 \left(\dot{u} f_1 + \frac{\dot{w}^2}{3} f_2 - \Delta f_1 \right) - \nu_x \frac{w}{b} \left(\dot{u} f_1 + \frac{\dot{w}^2}{3} f_2 \right) \right] + \frac{1}{2} k w^2 f_1 \right. \\
\left. + G \left[\pi^2 \cos^2 \frac{\pi x}{L} (q_s - q_t)^2 f_1 - \pi (q_s - q_t) \cos \frac{\pi x}{L} \left(\frac{2u}{b} - \dot{w} \right) f_1 + \frac{u^2}{b^2} f_1 \right. \right. \\
\left. \left. + \frac{\dot{w}^2}{3} f_2 - \frac{\dot{w}u}{b} f_1 \right] \right\} dx
\end{aligned} \quad (4.4)$$

For RBT the Core Energy given as :

$$\begin{aligned}
U_{c,R} = \int_0^L \left\{ \frac{C_x}{1260} \left[\left(5q_s^2 f_6 + 32q_t q_s f_7 + 68q_t^2 f_9 \right) \phi^2 \pi^4 \sin^2 \frac{\pi x}{L} \right. \right. \\
- 21\phi \pi^2 \sin \frac{\pi x}{L} (q_s f_3 + 4q_t f_8)(2\dot{u} + \dot{w}^2) + 315\dot{u}\dot{w}^2 f_4 + 420f_2(\dot{u}^2 - \dot{w}^2 \Delta) \\
+ 1260f_1 \left(\Delta^2 - \dot{u}\Delta \right) + 63\dot{w}^4 f_5 \left. \right] \\
+ C_y \nu_x \left[\Delta \nu_x \left(\dot{u} f_1 + \frac{\dot{w}^2}{3} f_2 - \Delta f_1 \right) - \frac{w}{b} \left(\dot{u} f_1 + \frac{\dot{w}^2}{3} f_2 \right) \right] + \frac{1}{2} k w^2 f_1 \\
+ G \left[\frac{8\pi^2}{15} \cos^2 \frac{\pi x}{L} (q_s - q_t)^2 f_{11} - \frac{2\pi}{3} (q_s - q_t) \cos \frac{\pi x}{L} \left(\frac{2u}{b} - \dot{w} \right) f_{10} \right. \\
\left. + \frac{u^2}{b^2} f_1 + \frac{\dot{w}^2}{3} f_2 - \frac{\dot{w}u}{b} f_1 \right] \left. \right\} dx
\end{aligned} \tag{4.5}$$

Work done by load

The work done comprises the axial load P multiplied by the total end shortening \mathcal{E} . The contributions come from pure compression, overall buckling and the in-plane displacement due to local buckling. This term remain unchanged from the TBT and RBT formulation in Chapter 2, given in Equation 2.25.

4.3.2 Total Potential Energy

The total potential energy, V , whether is equal to V_T or V_R , is obtained by summing all the energy contributions. Integrating over the depth and assembling all the strain energy and work done contributions, the Total Potential Energy is given as an integral over the length. For TBT:

$$\begin{aligned}
V_T &= U_b + U_m + U_c - P\mathcal{E} \\
&= \int_0^L \left\{ \frac{EI}{2} \left[\ddot{w}^2 + 2q_s^2 \frac{\pi^4}{L^2} \sin^2 \frac{\pi x}{L} \right] + D \left[2\Delta^2 + \frac{\dot{w}^4}{4} + q_t^2 \frac{\pi^4 \phi^2}{2} \sin^2 \frac{\pi x}{L} \right. \right. \\
&\quad \left. \left. + \dot{u}^2 + \dot{u}\dot{w}^2 - q_t \pi^2 \phi \left(\dot{u} + \frac{\dot{w}^2}{2} \right) \sin \frac{\pi x}{L} - 2\Delta \left(\dot{u} + \frac{\dot{w}^2}{2} \right) \right] \right. \\
&\quad \left. + C_x \left[\frac{\dot{w}^4}{20} f_5 + \frac{\dot{u}^2}{3} f_2 + \frac{\dot{w}^2 \dot{u}}{4} f_4 - \Delta \left(\dot{u} f_1 + \frac{\dot{w}^2}{3} f_2 - \Delta f_1 \right) \right. \right. \\
&\quad \left. \left. + \frac{q_t \phi}{12} f_3 \pi^2 \sin \frac{\pi x}{L} \left(q_t \pi^2 \phi \sin \frac{\pi x}{L} - \dot{w}^2 - 2\dot{u} \right) \right] \right. \\
&\quad \left. + C_y \left[\Delta \nu_x^2 \left(\dot{u} f_1 + \frac{\dot{w}^2}{3} f_2 - \Delta f_1 \right) - \nu_x \frac{w}{b} \left(\dot{u} f_1 + \frac{\dot{w}^2}{3} f_2 \right) \right] + \frac{1}{2} k w^2 f_1 \right. \\
&\quad \left. + G \left[\pi^2 \cos^2 \frac{\pi x}{L} (q_s - q_t)^2 f_1 - \pi (q_s - q_t) \cos \frac{\pi x}{L} \left(\frac{2u}{b} - \dot{w} \right) f_1 + \frac{u^2}{b^2} f_1 \right. \right. \\
&\quad \left. \left. + \frac{\dot{w}^2}{3} f_2 - \frac{\dot{w}u}{b} f_1 \right] - P \left[\Delta + \frac{1}{2} q_s^2 \pi^2 \cos^2 \frac{\pi x}{L} - \frac{1}{2} \dot{u} \right] \right\} dx
\end{aligned} \tag{4.6}$$

where, f_1, \dots, f_5 define the graded materials constants and given as:

$$\begin{aligned}
f_1 &= a_0 + \frac{a_1}{12} + \frac{a_2}{80} + \frac{a_3}{448} + \frac{a_4}{2304}, \\
f_2 &= a_0 + \frac{a_1}{10} + \frac{9a_2}{560} + \frac{a_3}{336} + \frac{5a_4}{8448}, \\
f_3 &= a_0 + \frac{3a_1}{20} + \frac{3a_2}{112} + \frac{a_3}{192} + \frac{3a_4}{2816}, \\
f_4 &= a_0 + \frac{7a_1}{60} + \frac{11a_2}{560} + \frac{5a_3}{1344} + \frac{19a_4}{25344}, \\
f_5 &= a_0 + \frac{11a_1}{84} + \frac{23a_2}{1008} + \frac{65a_3}{14784} + \frac{295a_4}{329472}
\end{aligned} \tag{4.7}$$

For RBT the total potential energy given as:

$$\begin{aligned}
V_R &= U_b + U_m + U_c - P\mathcal{E} \\
&= \int_0^L \left\{ \frac{EI}{2} \left[\dot{w}^2 + 2q_s^2 \frac{\pi^4}{L^2} \sin^2 \frac{\pi x}{L} \right] + D \left[2\Delta^2 + \frac{\dot{w}^4}{4} + (2q_t + q_s)^2 \frac{\pi^4 \phi^2}{18} \sin^2 \frac{\pi x}{L} \right. \right. \\
&\quad \left. \left. + \dot{u}^2 + \dot{u}\dot{w}^2 - (2q_t + q_s) \frac{\pi^2 \phi}{6} \sin \frac{\pi x}{L} \left(2\dot{u} + \dot{w}^2 \right) - 2\Delta \left(\dot{u} + \frac{\dot{w}^2}{2} \right) \right] \right. \\
&\quad \left. + \frac{C_x}{1260} \left[\left(5q_s^2 f_6 + 32q_t q_s f_7 + 68q_t^2 f_9 \right) \phi^2 \pi^4 \sin^2 \frac{\pi x}{L} \right. \right. \\
&\quad \left. \left. - 21\phi \pi^2 \sin \frac{\pi x}{L} (q_s f_3 + 4q_t f_8) (2\dot{u} + \dot{w}^2) + 315\dot{u}\dot{w}^2 f_4 + 420f_2 (\dot{u}^2 - \dot{w}^2 \Delta) \right. \right. \\
&\quad \left. \left. + 1260f_1 \left(\Delta^2 - \dot{u}\Delta \right) + 63\dot{w}^4 f_5 \right] \right. \\
&\quad \left. + C_y \nu_x \left[\Delta \nu_x \left(\dot{u} f_1 + \frac{\dot{w}^2}{3} f_2 - \Delta f_1 \right) - \frac{w}{b} \left(\dot{u} f_1 + \frac{\dot{w}^2}{3} f_2 \right) \right] + \frac{1}{2} k w^2 f_1 \right. \\
&\quad \left. + G \left[\frac{8\pi^2}{15} \cos^2 \frac{\pi x}{L} (q_s - q_t)^2 f_{11} - \frac{2\pi}{3} (q_s - q_t) \cos \frac{\pi x}{L} \left(\frac{2u}{b} - \dot{w} \right) f_{10} \right. \right. \\
&\quad \left. \left. + \frac{u^2}{b^2} f_1 + \frac{\dot{w}^2}{3} f_2 - \frac{\dot{w}u}{b} f_1 \right] - P \left[\Delta + \frac{1}{2} q_s^2 \pi^2 \cos^2 \frac{\pi x}{L} - \frac{1}{2} \dot{u} \right] \right\} dx
\end{aligned} \tag{4.8}$$

where, f_1, \dots, f_{11} the RBT graded material constants.

$$\begin{aligned}
f_1 &= a_0 + \frac{a_1}{12} + \frac{a_2}{80} + \frac{a_3}{448} + \frac{a_4}{2304}, \\
f_2 &= a_0 + \frac{a_1}{10} + \frac{9a_2}{560} + \frac{a_3}{336} + \frac{5a_4}{8448}, \\
f_3 &= a_0 + \frac{5a_1}{28} + \frac{5a_2}{144} + \frac{5a_3}{704} + \frac{5a_4}{3328}, \\
f_4 &= a_0 + \frac{7a_1}{60} + \frac{11a_2}{560} + \frac{5a_3}{1344} + \frac{19a_4}{25344}, \\
f_5 &= a_0 + \frac{11a_1}{84} + \frac{23a_2}{1008} + \frac{65a_3}{14784} + \frac{295a_4}{329472}, \\
f_6 &= a_0 + \frac{7a_1}{36} + \frac{7a_2}{176} + \frac{7a_3}{832} + \frac{7a_4}{3840}, \\
f_7 &= a_0 + \frac{25a_1}{144} + \frac{35a_2}{1056} + \frac{245a_3}{36608} + \frac{7a_4}{4992}, \\
f_8 &= a_0 + \frac{a_1}{7} + \frac{25a_2}{1008} + \frac{5a_3}{1056} + \frac{35a_4}{36608}, \\
f_9 &= a_0 + \frac{83a_1}{612} + \frac{205a_2}{8976} + \frac{665a_3}{155584} + \frac{1589a_4}{1867008}, \\
f_{10} &= a_0 + \frac{a_1}{20} + \frac{3a_2}{560} + \frac{a_3}{1344} + \frac{a_4}{8448}, \\
f_{11} &= a_0 + \frac{a_1}{28} + \frac{a_2}{336} + \frac{5a_3}{14784} + \frac{5a_4}{109824}
\end{aligned} \tag{4.9}$$

4.3.3 Critical load

The critical load for overall buckling can be defined by the linear eigenvalue analysis. To perform that, all the local mode terms, $u(x)$ and $w(x)$ from the Equations (4.6) and (4.8) must be set to zero.

$$P_T^C = \frac{2\pi^2 EI}{L^2} + \frac{2G\phi^2\pi^2 f_1 \left(D + \frac{C_x}{6} f_3 \right)}{2Gf_1 + \phi^2\pi^2 \left(D + \frac{C_x}{6} f_3 \right)} \tag{4.10}$$

$$\begin{aligned}
P_R^C &= \frac{2\pi^2 EI}{L^2} + \frac{840G\pi^2\phi^2 f_{11}(C_x A_1 + 6D) + C_x \pi^4 \phi^4 (C_x A_2 + 20DA_3)}{30(168Gf_{11} + 17C_x \phi^2 \pi^2 f_9 + 70D\phi^2 \pi^2)} \\
A_1 &= \frac{68f_9}{105} + \frac{f_6}{21} + \frac{32f_7}{105}, \\
A_2 &= \frac{85f_6 f_9}{21} - \frac{64f_7^2}{21}, \\
A_3 &= -\frac{8f_7}{3} + \frac{17f_9}{6} + \frac{5f_6}{6}
\end{aligned} \tag{4.11}$$

From each expression the first terms represent the load of the face plates buckling independently, and the last term represent the contributions from the face plates bending about the global neutral axis of the sandwich panel.

4.3.4 Governing Equations

Upon assembly of the potential energy for each model, the system of the two ordinary differential equations and three integral equilibrium constraints are obtained via the same strategy described in §2.4.10 by utilizing the calculus of variations and minimizing the potential energy with respect to the generalized coordinates. For the ODEs, the boundary conditions remain the same. The two non-autonomous coupled ordinary differential equations (ODEs) for the TBT model is presented first:

$$\begin{aligned}
\{EI\ddot{w}\}_T = & -D \left[2\Delta\ddot{w} + q_t\phi\pi^2 \left(\ddot{w} \sin \frac{\pi x}{L} + \dot{w} \frac{\pi}{L} \cos \frac{\pi x}{L} \right) \right. \\
& \left. - \left(2i\ddot{w} + 2\dot{w}\ddot{u} + 3\dot{w}^2\ddot{w} \right) \right] \\
& - C_x \left[\frac{2}{3}\Delta\ddot{w}f_2 + q_t\frac{\Phi\pi^2}{6} \left(\ddot{w} \sin \frac{\pi x}{L} + \dot{w} \frac{\pi}{L} \cos \frac{\pi x}{L} \right) f_3 \right. \\
& \left. - \left(\frac{1}{2}\dot{w}\ddot{u}f_4 + \frac{1}{2}\dot{u}\ddot{w}f_4 + \frac{3}{5}\dot{w}^2\ddot{w}f_5 \right) \right] \\
& - \frac{C_y\nu_x}{b} \left[\frac{2}{3}w\ddot{w}f_2 - \frac{2}{3}\nu_x\Delta b\ddot{w}f_2 - \dot{u}f_1 + \frac{1}{3}\dot{w}^2f_2 \right] - kwf_1 \\
& - G \left[\frac{\dot{u}}{b}f_1 - \frac{2}{3}\ddot{w}f_2 + \frac{\pi^2}{L} \sin \frac{\pi x}{L} (q_s - q_t)f_1 \right]
\end{aligned} \tag{4.12}$$

$$\begin{aligned}
\left\{ 2\ddot{u} \left(\frac{C_x}{3} f_2 + D \right) \right\}_T &= \frac{2\pi}{b} \cos \frac{\pi x}{L} \left[q_t \frac{\phi^2 \pi^2}{2} \left(D + \frac{C_x}{6} f_3 \right) - G(q_s - q_t) f_1 \right] \\
&\quad - 2\dot{w}\ddot{w} \left(D + \frac{C_x}{4} f_4 \right) + \frac{C_y \nu_x}{b} \dot{w} f_1 \\
&\quad - \frac{2G}{b} \left(\frac{\dot{w}}{2} - \frac{u}{b} \right) f_1
\end{aligned} \tag{4.13}$$

For RBT the ODEs are given as:

$$\begin{aligned}
\{EI\ddot{w}\}_R &= -D \left[2\Delta\ddot{w} + (q_s + 2q_t) \frac{\phi\pi^2}{3} \left(\ddot{w} \sin \frac{\pi x}{L} + \dot{w} \frac{\pi}{L} \cos \frac{\pi x}{L} \right) - (2i\ddot{w} + 2w\ddot{w} + 3\dot{w}^2\ddot{w}) \right] \\
&\quad - C_x \left[\frac{2}{3} \Delta\ddot{w} f_2 + (q_s f_3 + 4q_t f_8) \frac{\Phi\pi^2}{30} \left(\ddot{w} \sin \frac{\pi x}{L} + \dot{w} \frac{\pi}{L} \cos \frac{\pi x}{L} \right) \right. \\
&\quad \quad \left. - \left(\frac{1}{2} \dot{w}\ddot{w} f_4 + \frac{1}{2} i\ddot{w} f_4 + \frac{3}{5} \dot{w}^2 \ddot{w} f_5 \right) \right] - kw f_1 \\
&\quad - \frac{C_y \nu_x}{b} \left[\frac{2}{3} w\ddot{w} f_2 - \frac{2}{3} \nu_x \Delta b \ddot{w} f_2 - \dot{u} f_1 + \frac{1}{3} \dot{w}^2 f_2 \right] \\
&\quad - G \left[\frac{\dot{u}}{b} f_1 - \frac{2}{3} \ddot{w} f_2 + \frac{2\pi^2}{3L} \sin \frac{\pi x}{L} (q_s - q_t) f_{10} \right]
\end{aligned} \tag{4.14}$$

$$\begin{aligned}
\left\{ 2\ddot{u} \left(\frac{C_x}{3} f_2 + D \right) \right\}_R &= \frac{C_y}{b} \nu_x \dot{w} f_1 - D \left[2\dot{w}\ddot{w} - (q_s + 2q_t) \frac{\pi^3 \phi}{3L} \cos \frac{\pi x}{L} \right] \\
&\quad - C_x \left[\frac{1}{2} \dot{w}\ddot{w} f_4 - \frac{\pi^3 \phi}{30L} (q_s f_3 + 4q_t f_8) \cos \frac{\pi x}{L} \right] \\
&\quad - \frac{G}{b} \left[\dot{w} f_1 + \frac{4\pi}{3} f_{10} (q_s - q_t) \cos \frac{\pi x}{L} - \frac{2u}{b} f_1 \right]
\end{aligned} \tag{4.15}$$

The integral constraints for the TBT model given as:

$$\begin{aligned} \{P\}_T &= \frac{2\pi^2 EI}{L^2} + 2G \left(1 - \frac{q_t}{q_s}\right) f_1 \\ &+ \frac{2}{\pi L} \int_0^L \frac{G}{q_s} \cos \frac{\pi x}{L} \left(\dot{w} - \frac{2u}{b}\right) f_1 \, dx \end{aligned} \quad (4.16)$$

$$\begin{aligned} &\frac{G}{\phi} \pi (q_t - q_s) f_1 + \frac{q_t \phi \pi^3}{2} \left(D + \frac{C_x}{6} f_3\right) \\ &- \frac{1}{L} \int_0^L \left[\left(D + \frac{C_x}{6} f_3\right) \pi \sin \frac{\pi x}{L} \left(\dot{u} + \frac{\dot{w}^2}{2}\right) + \frac{G}{\phi} \cos \frac{\pi x}{L} \left(\dot{w} - \frac{2u}{b}\right) f_1 \right] dx = 0 \end{aligned} \quad (4.17)$$

$$\begin{aligned} \left\{\frac{P}{2}\right\}_T &= \Delta \left(2D + C_x f_1 - \nu_x^2 C_y f_1\right) \\ &- \frac{1}{2L} \int_0^L \left[\left(\dot{u} f_1 + \frac{\dot{w}^2}{3} f_2\right) (C_x - \nu_x^2 C_y) + D (\dot{w}^2 + 2\dot{u}) \right] dx \end{aligned} \quad (4.18)$$

The following integral constraints for the RBT are given as:

$$\begin{aligned} \{P\}_R &= \frac{2\pi^2 EI}{L^2} + \frac{16}{15} G \left(1 - \frac{q_t}{q_s}\right) f_{11} + \frac{C_x \phi^2 \pi^2}{126} \left(f_6 + \frac{16q_t}{5q_s} f_7\right) + \frac{D \phi^2 \pi^2}{9} \left(1 + \frac{2q_t}{q_s}\right) \\ &- \frac{1}{q_s L} \int_0^L \left[\frac{\phi}{15} (C_x f_3 + 10D) \sin \frac{\pi x}{L} \left(\dot{u} + \frac{\dot{w}^2}{2}\right) - \frac{4G}{3\pi} \cos \frac{\pi x}{L} \left(\dot{w} - \frac{2u}{b}\right) f_{10} \right] dx \end{aligned} \quad (4.19)$$

$$\begin{aligned} &\frac{4\pi G}{15\phi} (q_t - q_s) f_{11} + \frac{\phi \pi^3}{630} [(4C_x f_7 + 35D)q_s + (17C_x f_9 + 70D)q_t] \\ &- \frac{1}{L} \int_0^L \left\{ \left(D + \frac{C_x}{5} f_8\right) \frac{\pi}{3} \sin \frac{\pi x}{L} \left(\dot{u} + \frac{\dot{w}^2}{2}\right) + \frac{G}{3\phi} \cos \frac{\pi x}{L} \left(\dot{w} - \frac{2u}{b}\right) f_{10} \right\} dx = 0 \end{aligned} \quad (4.20)$$

$$\begin{aligned} \frac{P}{2} &= \Delta \left(2D + C_x f_1 - \nu_x^2 C_y f_1\right) \\ &- \frac{1}{2L} \int_0^L \left[\left(\dot{u} f_1 + \frac{\dot{w}^2}{3} f_2\right) (C_x - \nu_x^2 C_y) + D (\dot{w}^2 + 2\dot{u}) \right] dx \end{aligned} \quad (4.21)$$

4.3.5 The solution process

Having formulated the necessary equations, in order to establish the non-trivial interactive modes the system of governing ordinary differential equations, integral constants and boundary conditions was non-dimensionalized (Appendix A) and solved numerically using AUTO07p (Doedel et al 2012). The merits of using AUTO07p have been extensively highlighted in Chapters 2 and 3.

Case	$E_{eq}(MPa)$	$E_c(MPa)$	$E_{CE}(MPa)$	a_0	a_1	a_2	a_3	a_4
C0	198.57	198.57	198.57	1.0	0.0	0.0	0.0	0.0
C1.1ex	198.57	278.00	39.71	1.4	-4.8	0.0	0.0	0.0
C1.2ex	198.57	238.28	39.71	1.2	0.0	-16.0	0.0	0.0
C1.3ex	198.57	225.05	39.71	1.1333	0.0	0.0	-59.733	0.0
C1.4ex	198.57	218.43	39.71	1.1	0.0	0.0	0.0	-230.4
C2.1ex	198.57	258.14	79.43	1.3	-3.6	0.0	0.0	0.0
C2.2ex	198.57	228.36	79.43	1.15	0.0	-12.0	0.0	0.0
C2.3ex	198.57	218.43	79.43	1.1	0.0	0.0	-44.8	0.0
C2.4ex	198.57	213.46	79.43	1.075	0.0	0.0	0.0	-172.8
C3.1ex	198.57	238.28	119.14	1.2	-2.4	0.0	0.0	0.0
C3.2ex	198.57	218.43	119.14	1.1	0.0	-8.0	0.0	0.0
C3.3ex	198.57	211.81	119.14	1.06667	0.0	0.0	-29.8667	0.0
C3.4ex	198.57	208.45	119.14	1.05	0.0	0.0	0.0	-115.2
C1.1ve	198.57	99.29	397.14	0.5	6.0	0.0	0.0	0.0
C1.2ve	198.57	99.29	595.71	0.5	0.0	40.0	0.0	0.0
C1.3ve	198.57	99.29	794.28	0.5	0.0	0.0	224.0	0.0
C1.4ve	198.57	99.29	992.85	0.5	0.0	0.0	0.0	1152.0
C2.1ve	198.57	139.00	332.60	0.7	3.6	0.0	0.0	0.0
C2.2ve	198.57	139.00	436.85	0.7	0.0	24.0	0.0	0.0
C2.3ve	198.57	139.00	549.00	0.7	0.0	0.0	132.145	0.0
C2.4ve	198.57	139.00	666.14	0.7	0.0	0.0	0.0	679.6
C3.1ve	198.57	158.86	278.00	0.8	2.4	0.0	0.0	0.0
C3.2ve	198.57	158.86	357.43	0.8	0.0	16.0	0.0	0.0
C3.3ve	198.57	158.86	429.86	0.8	0.0	0.0	89.6	0.0
C3.4ve	198.57	158.86	516.28	0.8	0.0	0.0	0.0	460.8

Table 4.1: $a_0...a_4$ Material parameters. Note that E_C is the Young's modulus for the core center, E_{CE} is the Young's modulus for the core edge. Cases between C1.1-ve to C3.4-ve refers to concave distribution shape and C1.1-ex to C3.4-ex refers to convex distribution shape.

4.4 Results and discussion

4.4.1 Material and geometrical properties

A typical sandwich strut comprising stiff aluminium alloy plates and FGM core is used. The material and geometrical properties are given below:

Face plate Young's modulus	:	$E = 68947.57 \text{ MPa}$
Face plate Poisson's ratio	:	$\nu = 0.3$
Core Young's modulus	:	$E_c = 198.57 \text{ MPa}$
Core Poisson's ratio	:	$\nu_c = 0.2$
Core shear modulus	:	$G_c = 82.74 \text{ MPa}$
Face plate thickness	:	$t = 0.50 \text{ mm}$
Core thickness	:	$b = 5.00 - 10.00 \text{ mm}$
Length of the structure	:	$L = 100.0 \text{ mm}$

The axial load is assumed to be applied along the neutral axis of the sandwich panel through a rigid plate that spreads the load evenly through the depth of the panel. In order to compare the TBT and RBT models a number of geometrical and material parametric studies have been performed. Two types of parametric studies investigating gradation distributions through the depth of the core are presented, as reflected in Figure 4.2. The first parametric study where the material is relatively compliant at the core interfaces and stiffer at the mid-height of the core is denoted by “convex” (Figure 4.2a), while the second parametric study is where the stiffer core properties are at the face core interface is denoted by “concave” (Figure 4.2b). The material parameters for convex and concave parametric studies are tabulated in Table 4.1. For the concave parametric study, the Young's modulus of the core is kept constant and different patterns are examined with different Young's modulus at the face core interface, while convex parametric study the Young's modulus of

the face core interface is kept constant and different patterns are examined with different Young's modulus at the mid-height of the core. The case of the homogenous core with uniform through-the-thickness properties is denoted by "C0". The stiffness corresponding to this case corresponds to the average of the convex and concave parametric studies.

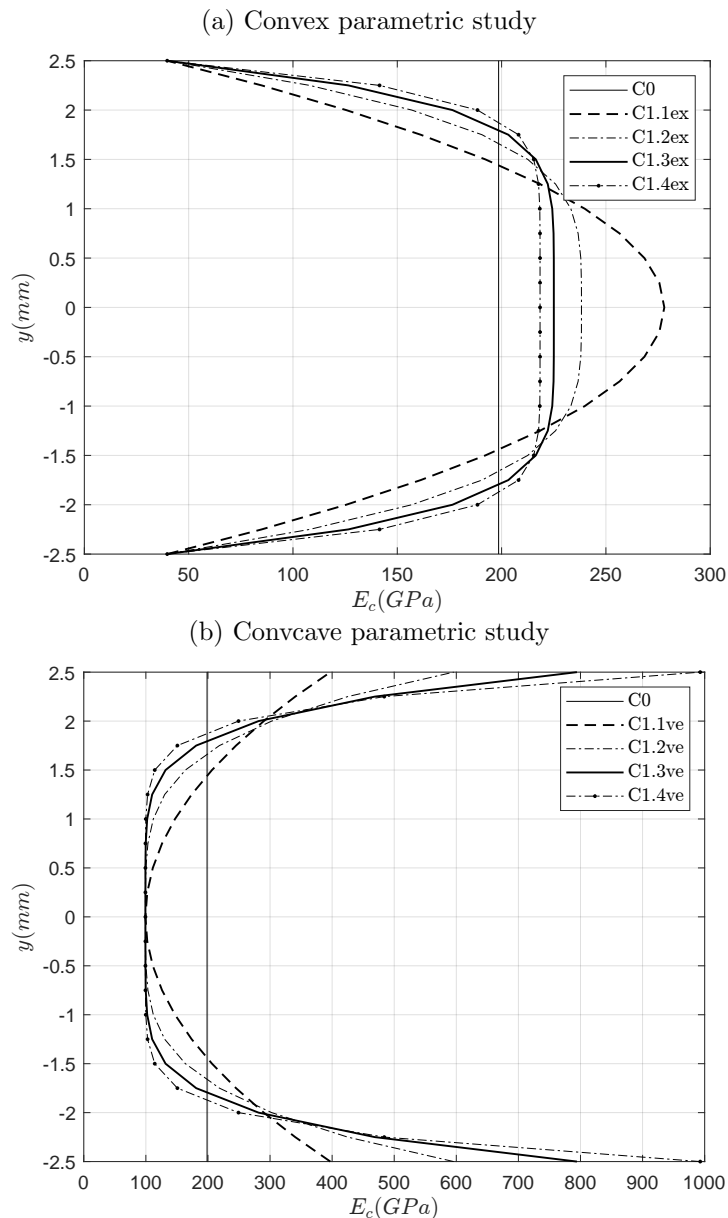


Figure 4.2: (a)-(b) The variation in material properties through the depth of the core. (a) Convex parametric studies cases and (b) Concave parametric studies cases.

4.4.2 Convex parametric study

In this section, three different convex parametric study cases are considered. Every case, four different core material gradation patterns are examined, labelled C1.1ex, C1.2ex, C1.3ex and C1.4ex (C1 denotes the case number and 1ex denote the material gradation pattern). In all cases, the core modulus at the face plate interface is kept fixed while the core modulus at the mid-plane is varied. The critical load for Case 1 with different material gradation patterns are given in the Table 4.2. The first and most important observation is that the TBT model indicates virtually no impact on critical load. This emanates from the graded material constant as it can be seen in the given Equation 4.10 (TBT critical load), where only f_1 and f_3 graded material constants are taken into account, f_1 is the ratio E_{eq}/E_c ; for this study is equal to 1, while the contribution of f_3 is minimal. On the other hand, for the RBT model can be seen in the given Equation 4.11, that more than one graded material constant is taken into account. For this reason the RBT model exhibits variation in critical load. The critical load increase from the C1.1ex to C1.4ex pattern, lies in the way the gradation in the core stiffness is treated. This is expected since an increase in core stiffness, is contributing to the resistance of the strut to buckling.

Case	$P_{TBT}^C(N/mm)$	$P_{RBT}^C(N/mm)$	TBT \mathcal{E}^S/L	RBT \mathcal{E}^S/L
C0	211.78	231.05	0.0276	0.0248
C1.1ex	211.62	252.47	0.0263	0.0200
C1.2ex	211.66	245.86	0.0267	0.0213
C1.3ex	211.69	242.26	0.0269	0.0220
C1.4ex	211.71	240.03	0.0270	0.0225

Table 4.2: The critical load for overall buckling for core depth $b = 5mm$ with different convex FGM patterns.

Figure 4.3(a,c) illustrates the equilibrium path for Case 1 with different

material gradation patterns. Comparing the prediction of the secondary bifurcation and the subsequent postbuckling path, the trend for the two models is the same. Starting with the secondary bifurcation point, which marks the onset of localized buckling, as the core stiffness increases (C1.4ex to C1.1ex) the plateau between the critical bifurcation point and the secondary decreases, more intensely is observed in RBT model. More importantly, the RBT model predicts the secondary bifurcation before the TBT model, which can be attributed to a more flexible representation of the cross-sectional deformation (Table 4.2).

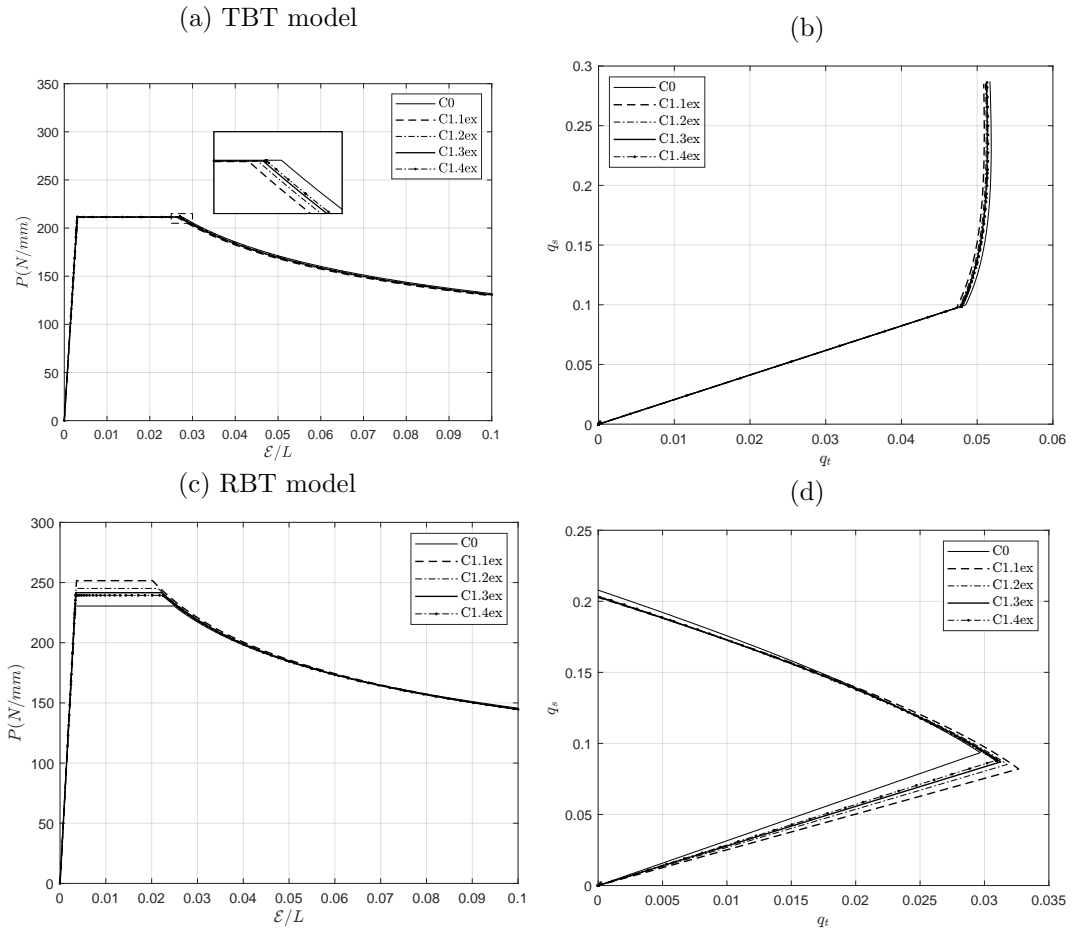


Figure 4.3: Left: plotting P versus normalized end shortening \mathcal{E}/L , Right: plotting amplitude of tilt q_t versus amplitude of sway q_s for struts of core depth $b = 5\text{mm}$. (a)-(b) TBT model and (c)-(d) RBT model.

Another interesting feature in the results is found during the comparison of the evolution of the overall mode components, sway and tilt. Figure

4.3(b&d) shows q_s plotted against q_t for different material gradation patterns. During prebuckling, the two models exhibit similar trends with q_s increasing along with q_t . Beyond the instability, for the TBT model, the slope of q_t decreases abruptly indicating a slower growth with increasing q_s . On the other hand, for the RBT model (4.3(d)) beyond the instability, q_t decreases with increasing q_s . This difference in the response can be attributed to the nonlinear cross-sectional deformation field which relaxes the constraint of constant tilting throughout the depth of the panel. Before the instability the difference in the cross-sectional deformations are small; beyond it, the in-plane displacement within the core becomes increasingly nonlinear while the displacement at the edges is very close to the corresponding displacements of TBT model. The decrease in q_t occurs since the minimum energy configuration for the displacement field is significantly influenced by the flexibility of the core under shear.

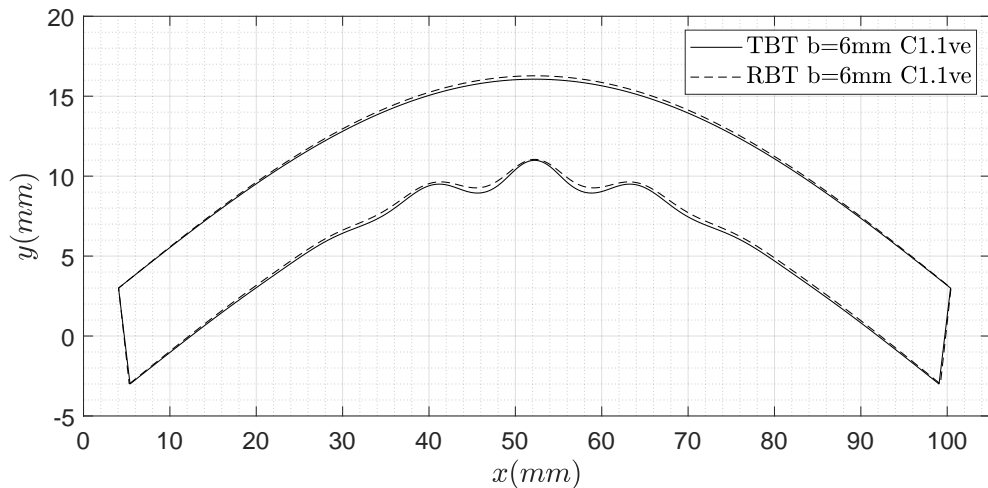


Figure 4.4: Interactive buckling on a sandwich panel 100mm long and 6mm deep at 5% end shortening.

Localized buckling is triggered beyond the point of instability and the modes are similar for both models since this is caused by the compressive stress in the bottom face plate, as shown in Figure 4.5. This effect manifests

itself as $w(x)$ and $u(x)$ become non-zero and grow as the axial load carrying capacity from P^C . The interactive buckling modes of TBT and RBT models exhibit similar characteristics qualitatively, both having a localized maximum displacement at midspan which decays towards the boundaries. Even though the RBT localized mode triggered first, leading to larger deflections than TBT equivalent, particularly in the neighbourhood of the limiting load, the two models become similar in amplitude and localized wavelength λ (Figure 2.16) in the far post-buckling range where the sway mode dominates.

Moving further to the important contribution of the two models—the prediction of the secondary bifurcation and the subsequent postbuckling path—for material gradation patterns with different cases are presented in Table 4.3. The average core stiffness for all cases is remain constant. As observed, the critical load and the prediction of the secondary bifurcation point for TBT model are same for all cases, on the other hand a slightly more measurable difference is observed for RBT model. Comparing the two models, the RBT model provides a higher critical load and predicts the secondary bifurcation point before the TBT model. This is supported by the fact that the RBT model assumes a different in-plane displacement field that is both influenced by the amplitude of tilt and sway after overall buckling has been triggered.

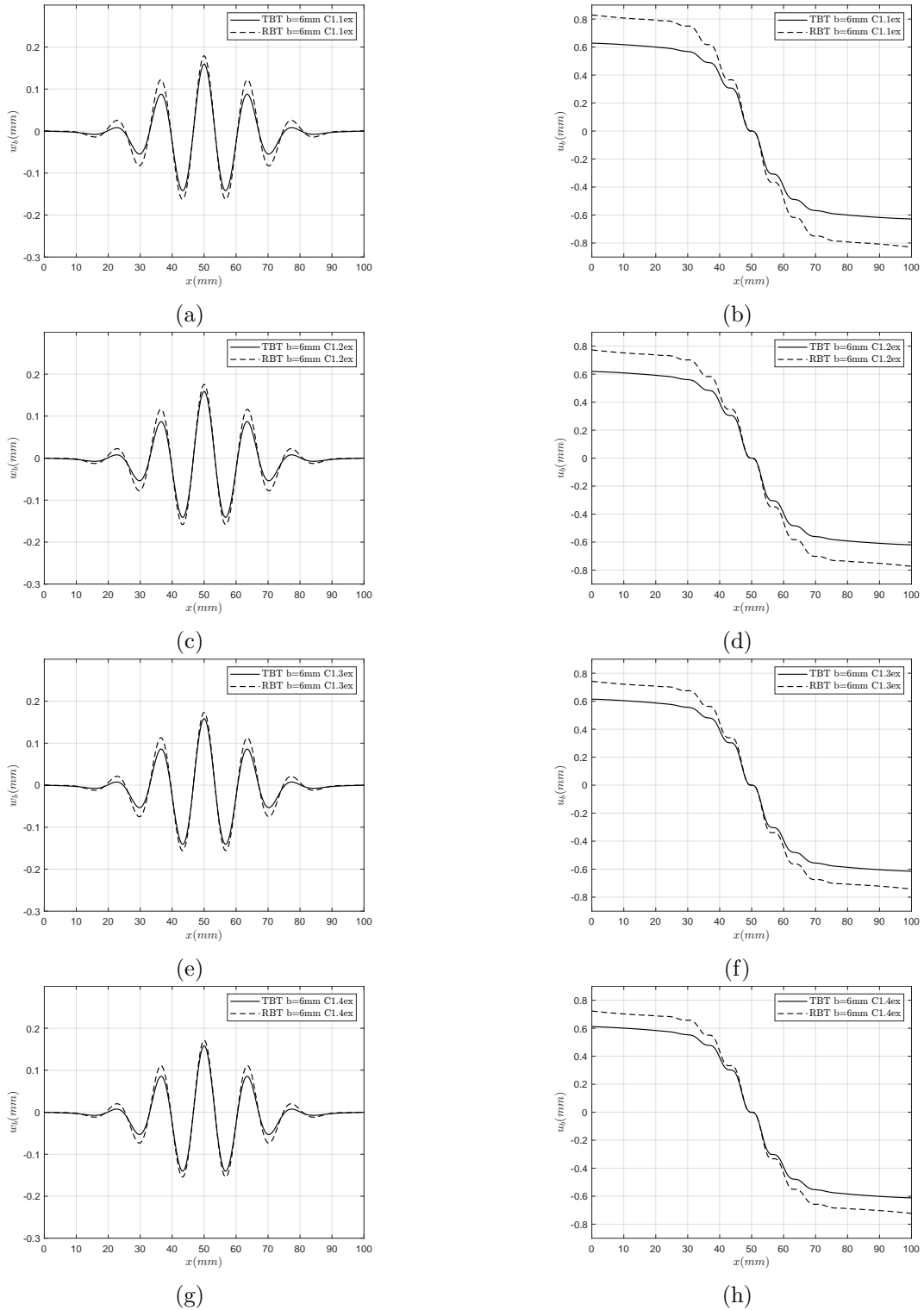


Figure 4.5: The evolution of the local modes (a),(c),(e),(g) $w(w)$ and (b),(d),(f),(h) $u(x)$ for the convex cases in the unloading path $\mathcal{E}/L = 5\%$. In this case: $L = 100\text{mm}$ and $b = 6\text{mm}$.

Case	P_T^C	P_R^C	TBT \mathcal{E}^S/L	RBT \mathcal{E}^S/L	TBT $\mathcal{E}^S/L - \mathcal{E}^C/L$	RBT $\mathcal{E}^S/L - \mathcal{E}^C/L$
C0	276.47	304.11	0.0211	0.0188	0.01723	0.01446
C1.1ex	276.24	335.44	0.01997	0.01503	0.01604	0.01026
C2.1ex	276.30	328.24	0.02026	0.01573	0.01632	0.01107
C3.1ex	276.36	320.63	0.02058	0.01663	0.01665	0.01207
C1.2ex	276.31	325.72	0.02029	0.01594	0.01636	0.01131
C2.2ex	276.35	320.61	0.02050	0.01656	0.01657	0.01199
C3.2ex	276.39	315.32	0.02075	0.01723	0.01681	0.01274
C1.3ex	276.34	320.44	0.02048	0.01649	0.01654	0.01193
C2.3ex	276.38	316.53	0.02064	0.01699	0.01670	0.01249
C3.3ex	276.41	312.51	0.02084	0.01754	0.01691	0.01309
C1.4ex	276.37	317.17	0.02059	0.01692	0.01666	0.01241
C2.4ex	276.39	314.02	0.02064	0.01733	0.01683	0.01287
C3.4ex	276.42	310.79	0.02089	0.01777	0.01696	0.01335

Table 4.3: The critical loads, end shortening and gap between critical and secondary bifurcations for core depth, $b = 6mm$ with convex FGM patterns for different cases.

Furthermore, using the previous strut configuration for four different core depths ($b = 5.0mm$, $b = 6.0mm$, $b = 8.0mm$ and $b = 10.0mm$), the interaction between the overall and local mode is examined. Comparing, the critical loads predicted by the two models, for all material gradation patterns indicates a similar trend as observed in Figure 4.6(a)&(c) since they both increase with an increasing core depth. This is expected since increases the core depth, contribute to the resistance of the strut to buckling. Also, as the core depth increases both models shows similar decreasing gap between primary and secondary bifurcation points (Figure 4.6(b)&(d)).

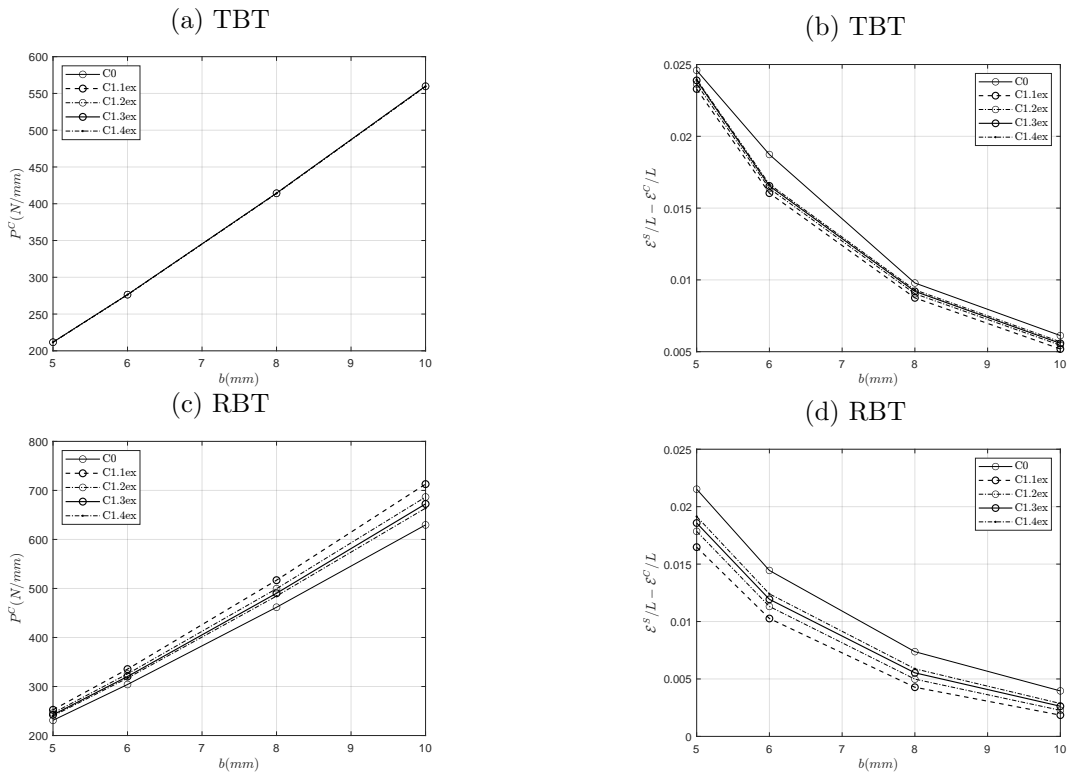


Figure 4.6: Comparison of the critical loads and gap between critical and second bifurcation point from the two analytical model for different core depth. (a)-(b) TBT model, (c)-(d) RBT model. Convex parametric study.

4.4.3 Concave parametric study

In the previous section, a convex distribution parametric study was considered. Herein, concave parametric studies to further examine the postbuckling behaviour are considered. As previously, four different type material gradation patterns are examined, labelled C1.1ve, C1.2ve, C1.3ve and C1.4ve. The core modulus at the mid-plane is kept fixed while the core face plate interface is varied. The critical buckling load and the position of the secondary bifurcation point for the two models with different type material gradation patterns are given in the Table 4.4. The critical buckling loads for RBT model with different gradation patterns are smaller than the values obtained for sandwich struts with homogeneous core (C0). Instead, the results of TBT model are good agreement with the case C0 (sandwich strut with homogeneous core). The differences in the critical load for the RBT model are dependent to the

cross-sectional displacement function set by the Reddy-Bickford theory. When the face-core interface stiffness is not high, the RBT model can predict the behaviour of sandwich structures with good accuracy. But, as the stiffness at the face-core interface increases, the critical loads diverge.

Case	$P_{TBT}^C(N/mm)$	$P_{RBT}^C(N/mm)$	TBT \mathcal{E}^S/L	RBT \mathcal{E}^S/L
C0	211.78	231.05	0.0276	0.0248
C1.1ve	211.99	195.34	0.0292	0.0361
C1.2ve	212.07	180.36	0.0299	0.0435
C1.3ve	212.12	172.89	0.0303	0.0485
C1.4ve	212.16	168.70	0.0306	0.0517

Table 4.4: The Critical load for overall buckling for core depth $b = 5mm$ with different concave FGM patterns.

Figure 4.7 shows the equilibrium paths for load versus end shortening for a concave parametric study with different gradation patterns. As mentioned in §4.4.1 for the TBT model virtually no impact on results is observed. The main difference is visible when comparing the tilt and sway components of the overall mode directly, as shown in Figure 4.7. Comparing all types of gradation patterns for RBT model, it is observed that the gap between critical and secondary bifurcation point depends by the face-core interface stiffness. As the stiffness near the face-core interface increases, the plateau between the critical and the secondary bifurcation point increases (as seen for C1.4ve).

At the secondary bifurcation, interactive buckling is triggered, leading to a localized buckling that maximizes at midspan. In Figure 4.8 the local mode at $\mathcal{E}/L = 5\%$ is presented. Comparing the gradation material patterns for RBT model, the figure clearly shows that the pattern with lower stiffness near the core-face interface predict an earlier onset of localization (Figure 4.8(d)). The effective match in the amplitude of localization between the different gradation

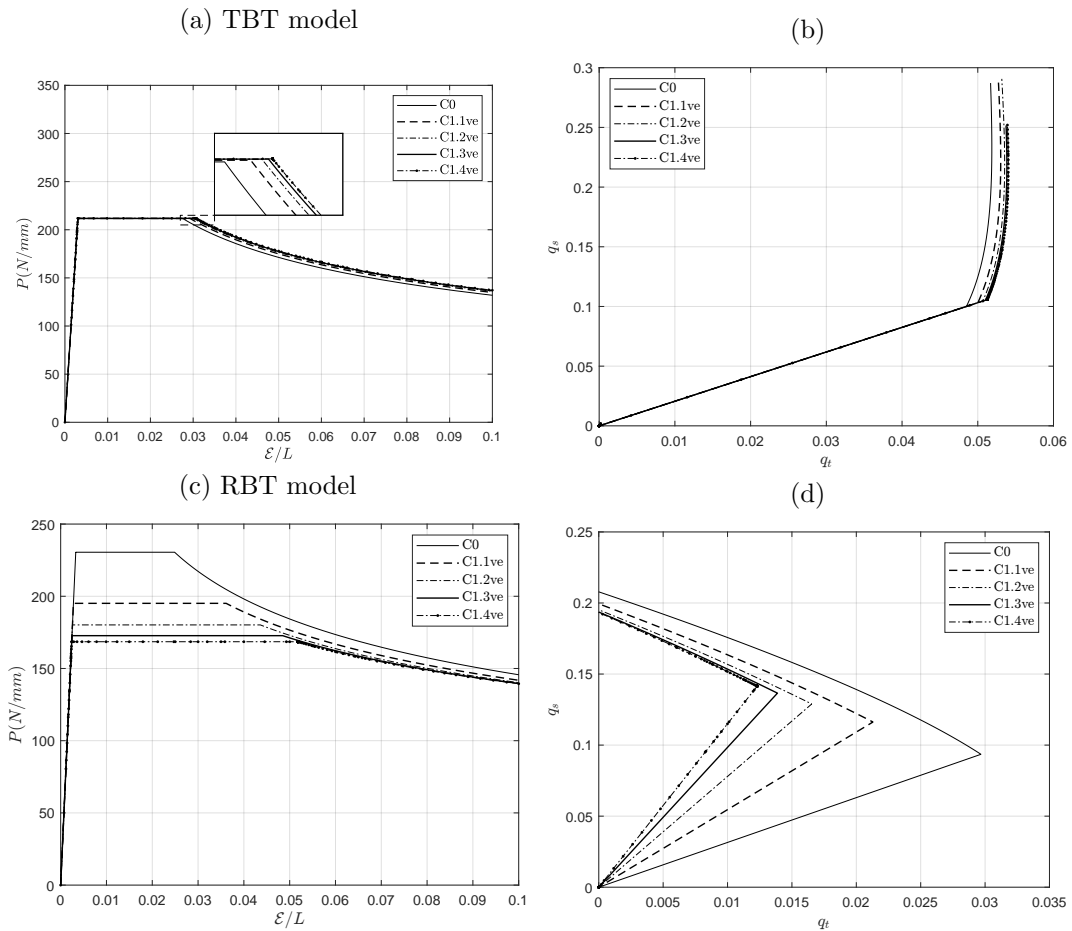


Figure 4.7: Equilibrium paths for concave parametric study for length 100mm and depth 5mm. (a) TBT model, (b) RBT model.

patterns at early postbuckling can be attributed to the close proximity of the secondary bifurcation points. The secondary bifurcation for the type C1.4ve is found to occur at lower load and therefore the localized buckling initially has a much smaller amplitude, when compared with all gradation patterns for RBT model.

As the buckling interaction is analyzed, it is important to show the effect of the interaction of buckling modes for all types of gradation patterns with different cases. The results of the postbuckling equilibrium path for all types patterns with different cases is presented in Table 4.5. An interesting feature, in the results is observed for the case 3 where the core stiffness increase and

the face-core interface stiffness decrease. In this case, for all pattern types (C3.1ve, C3.2ve, C3.3ve and C3.4ve), the results of the two analytical models are in good agreement. Comparing results for all pattern types with different cases, variation in the results for RBT model was observed. On the other hand, the results for TBT model are similar.

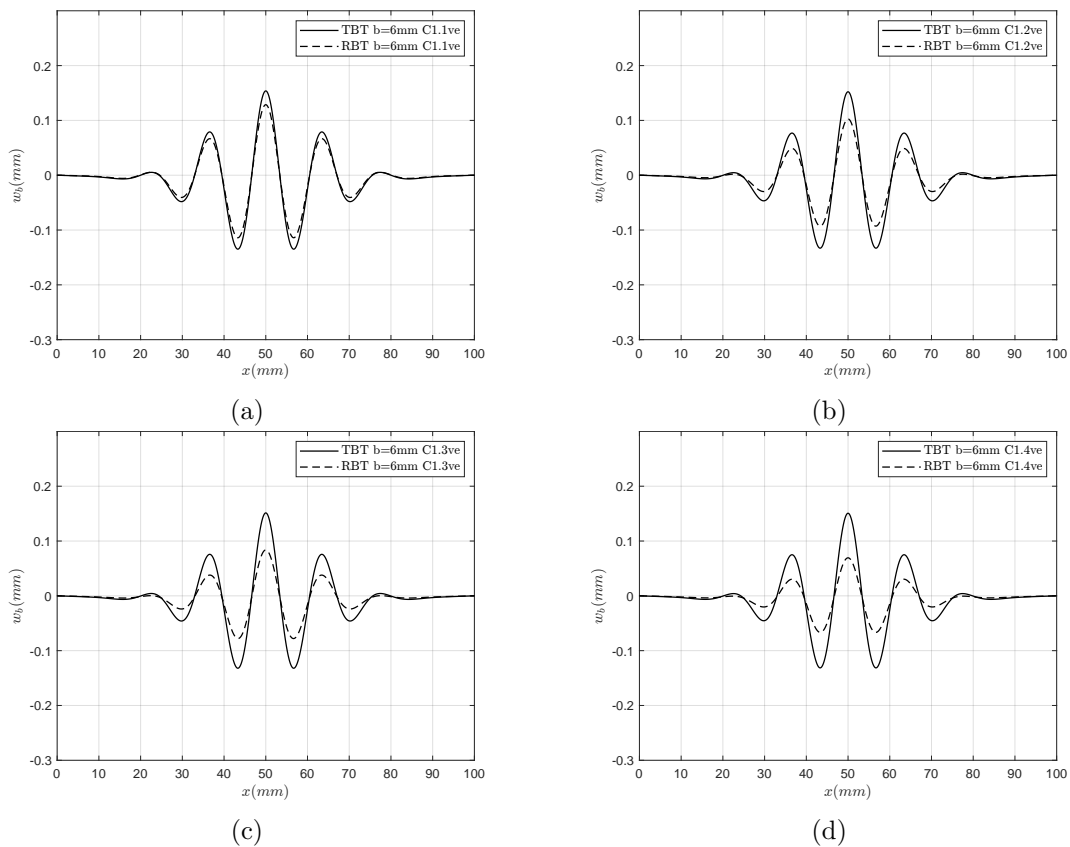


Figure 4.8: The evolution of the local modes $w(x)$ for the concave cases in the unloading path $\mathcal{E}/L = 5\%$. In this case: $L = 100\text{mm}$ and $b = 6\text{mm}$.

Case	P_T^C	P_R^C	TBT \mathcal{E}^S/L	RBT \mathcal{E}^S/L	TBT $\mathcal{E}^S/L - \mathcal{E}^C/L$	RBT $\mathcal{E}^S/L - \mathcal{E}^C/L$
C0	276.47	304.11	0.0211	0.0188	0.01723	0.01446
C1.1ve	276.77	253.16	0.02267	0.02829	0.01878	0.02468
C2.1ve	276.65	275.45	0.02207	0.02343	0.01813	0.01951
C3.1ve	276.59	285.58	0.02177	0.02048	0.01783	0.01755
C1.2ve	276.89	232.24	0.02333	0.03487	0.01939	0.03156
C2.2ve	276.72	264.69	0.02236	0.02584	0.01853	0.02207
C3.2ve	276.64	278.92	0.02203	0.02287	0.01859	0.01891
C1.3ve	276.96	221.92	0.02237	0.03918	0.01975	0.03602
C2.3ve	276.99	259.42	0.02264	0.02706	0.01870	0.02336
C3.3ve	276.67	275.80	0.02187	0.02036	0.01823	0.01970
C1.4ve	277.00	216.14	0.02391	0.04211	0.01997	0.03904
C2.4ve	276.01	256.64	0.02277	0.02787	0.01884	0.02422
C3.4ve	276.69	274.11	0.02171	0.02408	0.01832	0.02018

Table 4.5: The critical loads, endshortening and gab between critical and secondary bifurcation for core depth $b = 6mm$ with concave FGM patterns for different cases

To analyze the effect of the core depths on the post-critical equilibrium paths, the results for sandwich panels with core depth $5mm$, $6mm$, $8mm$ and $10mm$ and with different type material gradation patterns are compared. The results presented in Figure 4.9 indicate the differences in the postbuckling response. As the previous parametric study, the two analytical models are well correlated. As the core depth increases the critical buckling load increases and the gap between the critical and secondary bifurcation point decreases. Comparing all pattern types, more divergence between RBT results compared to TBT results is observed. The difference between the two models depends on the way the gradation in the core stiffness is treated.

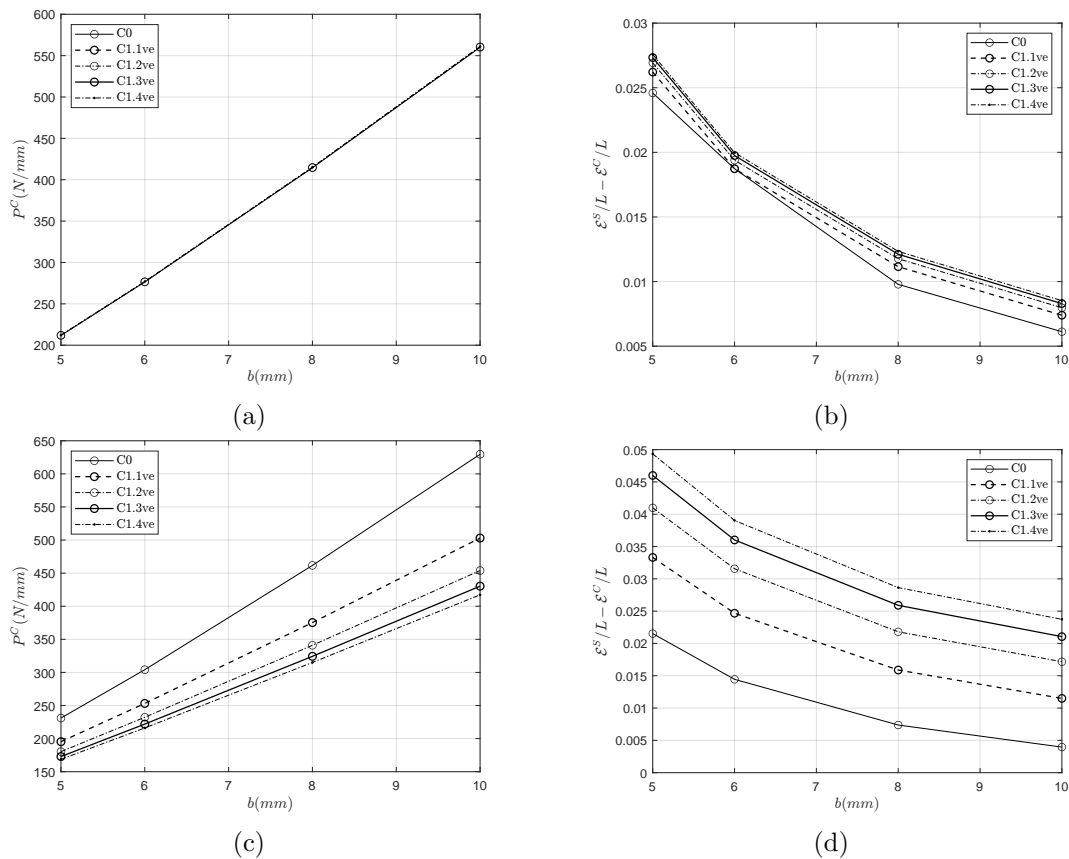


Figure 4.9: Comparison of the critical loads and gap between critical and second bifurcation points from the two analytical model for different core depth. (a)-(b) TBT model, (c)-(d) RBT model. Concave parametric study.

4.5 Conclusions

The utilization of functionally graded materials in the core of sandwich strut and its effect on their load carrying capacity and stability has been examined in the current chapter. The merits of FGM in the core can be realized by assigning a certain material property where it is most needed, without creating steep changes. This gradual change in the properties across the depth of the strut can minimize the risk of delamination in composites (such as sandwich panels) where there is a large interlaminar shear stress between the two laminates in the cases where the adhesive is not strong. If the stiffness of the softer layer gradually increases toward the interface, the danger of a shear discontinuity appearing is reduced. On the other hand, the reduction of the

stiffness at plates where it is not needed, could be utilized in an optimization strategy in system with weight constraints.

Two analytical models based on different shear deformable bending theories, as described in Chapter 2, have been adapted to investigate the interactive buckling of sandwich struts with functionally graded cores, using a symmetric polynomial gradation function. The two models are tested with struts where the stiffness in the core is graded symmetrically about the neutral axis. In the “Convex” first parametric study, the stiffness of the core is larger at the neutral axis and decreases towards the extreme edges. In the “Concave” parametric study, the trend is reversed with shear stiffness being minimum at the neutral axis and increasing further from it. The two models exhibited different results regarding the critical buckling load and the position of the secondary bifurcation point. The TBT model, shows virtually no impact on results, while the RBT model exhibits variations in both critical load and position of secondary bifurcation. The difference between the two models lies in the way the gradation in the core stiffness is treated. For TBT model, as its name implies the shear strain is assumed to be constant across the depth of the strut due to the use of the Timoshenko beam theory. The RBT model though, is based on a third order theory, assuming a quadratic distribution of shear strain which is maximum in the middle and zero at the extreme edges. This makes the RBT model more versatile to adapt to the gradation in the stiffness of the strut predicting a more realistic cross-sectional deformation distribution at for convex gradation parametric study, than the TBT model.

The results of this study between the two analytical models have shown that the RBT model provides a safer estimation of the location of the secondary bifurcation where the secondary instability is initiated as a result of higher axial stresses developing in the face plates. This effect is magnified for

sandwich struts with concave FGM cores where the difference between the two models becomes more pronounced. Conversely, for sandwich struts with convex FGM core and deeper cores, the differences between the two analytical models become negligible since overall buckling dominates and the relative influence of the shear capacity of the core reduces. In terms of the critical load, the RBT model overestimates the critical load compared to the TBT model, indicating that the linear in-plane displacement field is a more accurate representation of the actual field in all cases.

The next chapter describes the development of finite element models for sandwich struts using the commercial package ANSYS (2019). These models are used to compare the analytical models for a number of different cases.

Chapter 5

Comparison of analytical models with finite element simulations

In Chapters 3 and 4, mechanical models based on different shear deformable theories and different attributes were presented. In Chapter 3 the focus was to identify whether the allowance of inhomogeneous deformation in the least compressed face plate of a sandwich strut undergoing interactive buckling leads to a substantially different behaviour in the interactive mode evolution. Furthermore the model was able to offer insights when the local (hourglass) mode was critical. In Chapter 4 the focus shifted on parametric design for the core and how the gradation in core mechanical properties affects interactive buckling when overall mode is critical, showing distinct differences in the response of the two models with the different shear deformable theories, both in terms of the critical load as well as the onset and subsequent interactive buckling response.

The chapter begins with an introduction into finite element (FE) modelling pertinent to geometrically nonlinear analysis and stability, followed by a description of FE stability models from the literature and the development of

the current bespoke model. The chapter ends with comparison of the results of the mechanical models with finite element simulations for different geometric and material cases.

5.1 Finite element method

Before describing numerical models from the literature, a brief introduction to the finite element method is presented, which is commonly applied to structural engineering problems. The finite element method (FEM) is a method for numerical analysis of field problems. Numerical methods, as the name implies, offers an alternative way to continuous mathematical modelling in analysing structures. Unlike the analytical modelling—which is based on continuous shape functions—used in the development of the TBT and RBT models, the finite element method, discretizes the system into nodes and elements. The system does not need to be described by differential equations, but rather through the relationship between the displacement of the nodes using appropriate shape functions for the elements. Through an iterative procedure, the loads (or displacements) are applied to the structure and the response of the elements is computed at each step. With advances in technology and computational power, FEM has become increasingly popular for analysing complicated structural and geometrical engineering problems, especially the ones for which closed form solutions form are not easily obtainable.

The finite element method can be used for both linear and geometrically nonlinear systems (Belytschko et al 2000). For linear elastic analysis, the equilibrium of the structural system is invoked from the local (node, element) level to the overall by satisfying appropriate physical boundary conditions. The equilibrium is given as the assembly of:

$$\{P\} = [K]\{U\} - \{P_p\}, \quad (5.1)$$

where $\{P\}$ is the set of equivalent nodes due to external loading, $[K]$ is the structural stiffness matrix and $\{U\}$ is the set of nodal displacement. The final term $\{P_p\}$ is zero for perfect structures, but for most practical situations this term represents equivalent nodal loading due to imperfections, such as initial lack of fit, initial thermal strains and distributed loading. The equations are assembled for all nodes with the nodal displacements being the unknowns. For geometrically nonlinear analysis the effects of the deflected shape at each step need to be considered when calculating at each equilibrium state. The geometric nonlinearities are manifested in the stiffness matrix, which is no longer constant, and changes with changing displacements. Since this makes the direct force equilibrium calculations cumbersome, the principle of virtual work is thus utilized. In the context of nonlinear structural analysis, the principle states that a structural system is in equilibrium in its deflected configuration if the external work, performed by the applied forcing over any possible infinitesimal displacement mode, is equal to the internal work performed by the component forces over the corresponding compatible infinitesimal deformations, thus:

$$\delta W = \delta\{d\}^T \{f\}. \quad (5.2)$$

In this relationship, δW is the incremental work done by the structure, $\{d\}^T$ is the transpose of the set of deformations, $\{f\}$ is the set of internal forces and this holds for all increments of the nodal displacement $\delta\{U\}$. The equilibrium equations can thus be expressed in the form of:

$$\{G\} = \left\{ \frac{\partial V}{\partial \{U\}} \right\} = \{0\}, \quad (5.3)$$

where ∂V refers to the change in the potential energy and $\{G\}$ describe the

out-of-balance forces. The infinitesimal variation of the out-of-balance forces $\{G\}$ with respect of the degrees of freedom of the system $\{U\}$ is known as the tangent stiffness matrix, $[K_T]$:

$$\{G\} = \left[\frac{\partial\{G\}}{\partial\{U\}^T} \right]. \quad (5.4)$$

For conservative loading, the nonlinearity in the system can only be considered in terms of the tangent stiffness matrix which is symmetric. This comprises the material constant stiffness matrix associated with the constitutive law and geometric stiffness matrix which is associated with geometric nonlinearities:

$$[K_T] = [K_E] + [K_G], \quad (5.5)$$

where

$$[K_E] = [T]^T [k] [T], \quad (5.6)$$

and

$$[K_G] = \left[\frac{\partial^2\{d\}^T}{\partial\{U\}\partial\{U\}^T} \{f\} \right] - \left[\frac{\partial^2 W_i}{\partial\{U\}\partial\{U\}^T} \right] - \Lambda \left[\frac{\partial^2 W_n}{\partial\{U\}\partial\{U\}^T} \right]. \quad (5.7)$$

Here, $[T]$ is a geometric transformation matrix, $[k]$ is the stiffness constant matrix and Λ is the load factor. The subscripts i and n refer to the initial and the next stage respectively. The geometric stiffness matrix is dependent on the deflected shape of the structure, the presence of existing imperfections (as indicated by the second variation of work $\partial^2 W_i$) and the applied loads as indicated by the third term with the corresponding load factor Λ .

5.2 Buckling and postbuckling analysis

Buckling in structures is associated with the presence of bifurcation points

which lead to more than one equilibrium state or limit points in the response. The position of these points, which reveals the critical loads, can be found by the nature of tangent stiffness matrix through linear analysis. In the discrete system case, such as the case in FEM, the second variation of the energy is given as:

$$\delta^2 V = \frac{1}{2} \delta\{U\}^T [K_T] \delta\{U\}. \quad (5.8)$$

Taking advantage of this form, and by finding the determinant of the tangent stiffness matrix, the stability of the system can be found from the sign of the result. Specifically, if the determinant of $[K_T]$ is positive this translates to a stable equilibrium path, if it is negative to an unstable path and when it is zero this is the signature of a critical point. The critical point can be classified as a limit point if the first order work done by the load over any of the buckling modes $\delta\{U\}$ is non-zero. If it is zero, then it indicates the presence of a bifurcation point. To evaluate the critical loads at the bifurcation or limit point, the tangent stiffness matrix is observed more closely. Since the material stiffness matrix, $[K_E]$, remains positive for elastic systems with changing load or displacement, the focus shifts to the geometric stiffness matrix by considering the linear change in terms of Λ in $[K_T]$.

$$[K_T] = [K_T^A] + \Delta\Lambda [K_{G_n}^A], \quad (5.9)$$

where the superscript A represents the initial stage of the matrices. If A represents the unloaded state, then when the determinant of $[K_T]$ becomes zero, the values of $\Delta\Lambda$ that satisfy the above equation are the critical loads of the different buckling modes.

Even though linear buckling analysis can provide the critical buckling loads and expected mode shapes, it cannot progress any further beyond the critical

points, especially in the cases of bifurcations, where more than one nontrivial equilibrium paths are available. Nonlinear analysis is thus employed to trace postbuckling paths using incremental methods by tracing successive adjacent equilibrium states. The two incremental methods used in structural engineering are known as load control and displacement control methods, sometimes also called “dead” or “rigid” loading respectively. As their corresponding names imply, neighbouring equilibrium states on the path are computed iteratively by applying small increments of either loads or displacements respectively. The nature of these incremental methods may lead to erroneous results, if applied to a perfect structure from the unloaded state, since upon reaching the bifurcation, the next successive state might be still on the fundamental path, hence skipping over the bifurcation point. A small imperfection allows the method to compute and trace an equilibrium path as close as possible to the perfect path. A large step-size in load control may again lead to erroneous results especially close to the critical point, where smaller step-sizes are necessary for continuation purposes (Figure 5.1). Displacement control methods can usually rectify the situation, although nowadays most commercial codes, such as ANSYS, offer adaptive step-sizes to increase computational efficiency.

A numerical technique for tracing equilibrium paths in FEM is the Newton-Raphson procedure to compute the tangent stiffness matrix at every iteration. The modified Newton-Raphson strategy can also be implemented for which the tangent stiffness matrix is only computed at the beginning of each set of iterations, reducing the computational cost significantly. Finally, close to limit points in the equilibrium path the Riks pseudo-arclength algorithm (Riks 1979) is also invoked in order to trace the continuous paths whether stable or

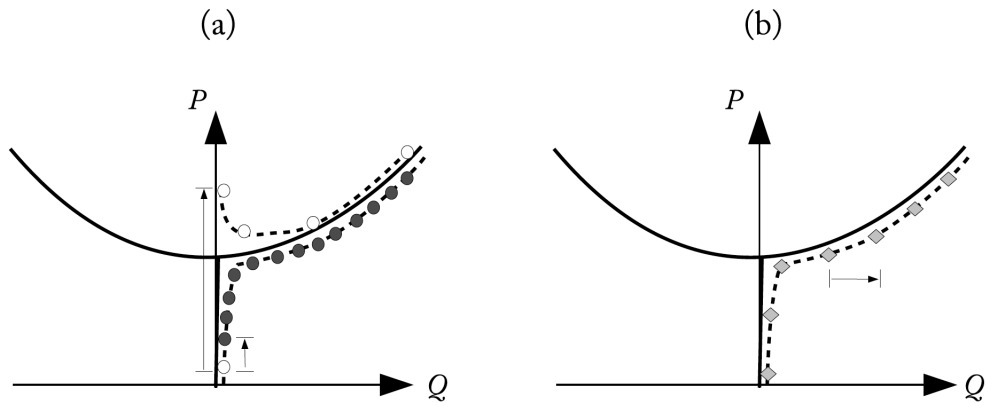


Figure 5.1: A diagram exhibiting the two incremental methods on a post-critical bifurcation system. (a) Load control and (b) displacement control. Symbols indicate "o" large step load control, "•" small step load control and "◇" displacement control.

unstable.

5.3 Errors

Results computed by finite element analysis contain errors, except in instances where the mathematical model is so simple, that a closed form solution of the continuum could also be possible with limited effort. Error here is a reference to the deviation between finite element analysis results and the exact solutions of the mathematical model. There are three main sources of error associated with the finite element method, namely modelling, discretization and computational errors (Cook et al 2002). The first source, modelling errors, refers to the difference between a physical system and its mathematical model. As the mathematical model is a simplification of the actual problem, based on accepted assumptions, the omission of details in the model might introduce errors in the modelling.

The second source of error comes from the degree of discretization. This error can become increasingly important if the discretization leads to a coarse mesh of elements, while on the other hand, it can be minimized by refining

the mesh with more nodes and elements at the expense of increased requirements for computational power. Another example of discretization errors is seen when the discretization cannot match or follow the continuum response due to the use of inappropriate shape functions for element deformations and their aspect ratio (Cook et al 2002). Especially in the presence of localized loads or other special boundary conditions, inappropriate shape functions can lead to large discontinuities in the stress-strain response between adjacent elements and hence erroneous results can be obtained. The complexity of the element and accuracy of the response in finite element modelling is associated with the aspect ratio of the element and the order of the elemental shape functions which are usually in the form of polynomials and guide the variation (if any) of stresses and strains within the element. Obviously, high order multi-nodal elements imply a significant increase in the computational cost, so in an optimum finite element model, these should only be used where they are most needed, with lower order elements being used everywhere else, making sure though that compatibility through the structural model is satisfied. For linear problems, the discretized system has a stiffer response since the work done by the loads is always less than the work done by the continuous model. As the mesh is refined, the solution of the work done from the discretized system approaches the exact solution from the continuum. The third and final source of error is associated with computational errors since by rounding off very small numbers, these errors can accumulate and can lead to unexpected results. It is worth applying some engineering intuition and back-analysis for parts of the structure in question to verify the validity of the obtained results.

5.4 Modeling sandwich structures with Finite Element

Modelling sandwich structures is not as straightforward as modelling ho-

mogeneous components, due to the composite nature of the structural system. Zenkert (1995) includes a chapter on the use of finite element analysis in the modelling of sandwich structures. In addition to the common sources of error outlined above, the author reports a few more key points to be considered in the finite element analysis, such as the core shear, local effects, boundary conditions and the potential anisotropy in the material properties of the face plates or the core.

Taking into account the geometry of regular sandwich panels, the problem can be reduced to two dimensional (2D) modelling, where the face plates can be modelled as rods and the core with membrane elements (Zenkert 1995). Rod elements can take either compression or tension while membrane element will be able to shear, since this is the main function of the core. In the case of sandwich panels for which the bending strain in the face plates is quite important, the face plates could be modelled with beam elements, hence allowing bending stresses to develop as well. The use of beam elements that share nodes with core membrane elements can lead to a small degree of incompatibility in the lines joining two nodes at the interface, since beam elements have rotational degrees of freedom while the membrane elements do not. This issue can be rectified with the use of membrane elements for the face plate as well, which refines the mesh significantly, since it is advisable that the side aspect ratios of membrane elements should be confined to 1:10 (Zenkert 1995). Other combinations of modelling include formulating the core with solid elements and using beam elements for the face plates which leads to the same sort of incompatibility at the interfaces mentioned previously.

5.4.1 Sandwich strut finite element models in the literature

Léotoing et al (2004) and Kim and Shridharan (2005) have both reported

on cases where interactive buckling and localization occurred after overall buckling. Léotoing et al (2004) describes the development of an analytical model to calculate the critical loads and buckling modes of different sandwich panels. The paper considers simply supported sandwich panels with three possible buckling modes, overall and two types of face wrinkling, antisymmetric ('snake') and symmetric ('hourglass'). In addition, finite element models were also developed to investigate the full postbuckling response of sandwich panels with different geometric configurations. The panels were modelled with solid two-dimensional bilinear plate stress elements and beam elements for the face plates. Perfect bonding between the core and the face plates was assumed. Initially, a linear elastic constitutive model was used and small imperfections were applied from the unloaded state to trace the equilibrium path. For the boundary conditions at the ends, the nodes were constrained in their local vertical and rotational degree of freedom. This was done to model adequately realistic conditions where the edges were stiffened by close-outs in order to apply connections or loading (Hexcel 1989). The load was applied horizontally on the edge supported on rollers along the neutral axis of the panel. In the later parts of that article, nonlinear analysis using elastoplastic material properties for sandwich panels was also implemented.

Kim and Shridharan (2005) also investigated the response of sandwich columns with a particular emphasis on the interaction of two competing buckling modes, the long-wave overall buckling mode and local buckling. The finite element modelling was implemented using Abaqus 5.8, where linear analysis was used initially to capture the linear buckling loads and mode shapes. Non-linear Riks analysis was then implemented to trace the postbuckling response of the sandwich columns. A two-dimensional finite element model was developed by the authors, with 3-noded Timoshenko beam elements, known as B22, for the face plates and plane stress solid elements with 8 nodes, known as CPS8.

Le Grogneq and Saoud (2015) developed two-dimensional finite element model, that included finite plasticity, arc-length methods and brach-switching procedures in order to investigate sandwich columns in elastoplastic buckling and post-buckling response. In the elastic range it was observed that secondary bifurcation points may generally occur for most of the geometric and material configurations, due to the modal interaction phenomena, leading to unstable collapse. On the other hand, in plasticity, no secondary bifurcation point is observed but the primary deformed shaped, either local or global, tend to localize, which in most cases corresponds a sharp snap-back phenomenon. A similar phenomenon was observed in the experiments undertaken by Wadee (1999).

5.4.2 Current model

In order to proceed with the comparisons, new finite element formulations are necessary with boundary conditions and constraints simulating the ones in the analytical modelling. Since the current research work is based on simply supported, perfectly elastic structural members, with perfect bonding at the face plate - core interface, these assumptions must be reflected in the finite element modelling. The models are formulated in the general purpose finite element package ANSYS (2019).

The sandwich struts are modelled with two-dimensional plane stress elements, the same assumption used in the analytical modelling. Given that sandwich panels are wide, plane strain could have also been used without a significant difference in the response other than it would give slightly higher critical load. The face plate and core are discretized with two dimensional (2D) solid element (Plate182) which is defined by four nodes having two degrees of freedom (DOF) at each node. Symmetry along the length of the strut has

been utilized, only half of struts has been modeled in the FE simulations by applying suitable boundary conditions along the axis of symmetry at the mid span of the strut Figure (5.2(a)). This is possible due to the inherent symmetry of the interactive mode along the span of the strut. Figure 5.2(b) shows the boundary conditions adapted for analyzing sandwich struts. The left and right edge are constrained in the vertical and horizontal direction. ANSYS enables the use of a multipoint constraint, such as either edge is constrained to behave as a solid medium, i.e. the nodes are prescribed to move along a straight line connecting the two extreme nodes located on the top and bottom skins. The line can stretch linearly and rotate around a central node, the degree of freedom of which is used to apply the boundary conditions and loading. On the right edge, symmetry conditions are applied with restrictions on the horizontal displacement and rotation while vertical displacement is permitted.

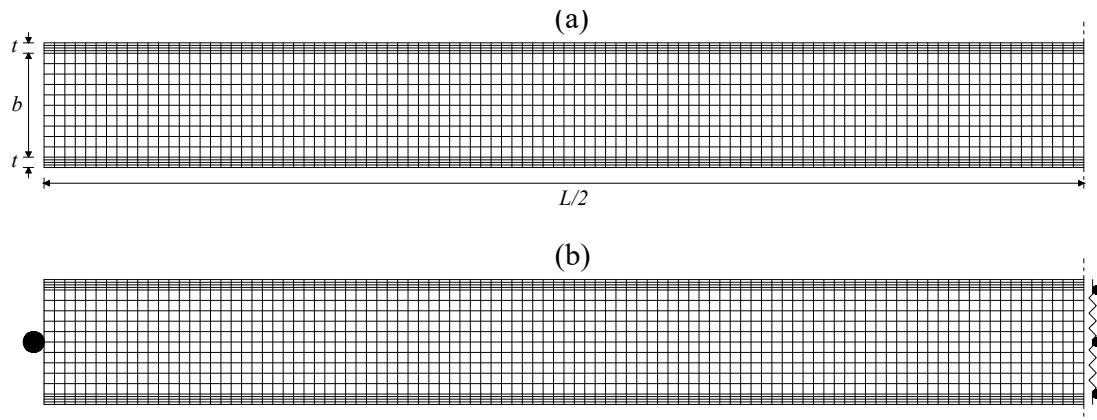


Figure 5.2: (a) Finite element sandwich panels, (b) The boundary conditions applied to the finite element model.

In order to study the buckling behaviour, ANSYS uses linear eigenvalue analysis for critical buckling and eigenmode predictions. Alternatively, non-linear geometry effects are turned on and postbuckling behaviour is evaluated along the buckling load. The geometrical nonlinear analyses are led with ANSYS and the use of an arc-length algorithm permits the investigation the post-buckling problems both with stable and unstable behaviours. In the nonlinear

geometry analysis, geometric imperfections can be defined by the linear superposition of buckling modes or any other displacement distributions. Often imperfections are assumed to be of the same shape as the first mode achieved from eigenvalue analysis. The amplitude of the imperfection is typically selected to manufacturing standards. An imperfection amplitude of $L/10000$ is selected as it sufficient to trigger the instability, and small enough to trace a path close to the equilibrium path of the perfect structure.

5.5 Comparison of FE simulations with the mechanical models in Chapter 3

Finite element simulations are conducted to capture both the bottom face plate localization as well as the top face plate local deformations. As seen in Table 5.1, the results from FE simulations achieved good agreement when compared to the analytical model in terms of critical loads for both cases of criticality (i.e. when overall buckling is critical or when local buckling is critical). For the cases where local buckling is critical, eigenvalue analysis revealed that "snake" (antisymmetric) and "hourglass" (symmetric) local modes are extremely close with the "snake" mode having a marginally smaller buckling load, as also observed in the literature (Williams et al 1941). For sufficiently deep cores where local buckling is critical, such as the range of depths used herein, the strain energy stored at the neutral axis is negligible and remains mostly unaffected, unlike the case of thinner cores where the neutral axis distorts following the buckled pattern of the face plates. Therefore, since the nature of local buckling is mainly governed by the face plate stiffness and thickness, as well as the core stiffness, the critical loads for the antisymmetric (snake) and symmetric (hourglass) modes of the same number of half-sine waves tend to be very close.

$b(mm)$	$P_{FE}^C(N/mm)$	$P_{Anal}^C(N/mm)$	Mode type
5.08	238.0	218.0	overall (Euler type: $i = 1$)
12.7	807.4	764.8	overall (Euler type: $i = 1$)
16.0	1009.2	959.35	local (Euler type: $i = 13$)
18.0	1020.4	1086.8	local (Euler type: $i = 13$)

Table 5.1: Comparison of FE and analytical model results, i represents the number of half-sine waves present in the eigenmode.

The equilibrium diagrams compare very well with the analytical model results for different strut depths, as seen in Figure 5.3. There was good agreement for the critical loads, which improved for deeper struts. The difference in the overall buckling loads results from the simplified kinematics in the analytical model for the overall mode, since the primary objective is to capture interactive buckling and is more appropriate for longer struts where the buckling loads for symmetric and antisymmetric modes are sufficiently close together. The agreement is even better in the postbuckling range, where the responses follow the same (unstable) unloading trend. For the case where overall buckling is triggered first, the principal difference can be seen in the far postbuckling range. The FE simulation locks the localized mode within the bottom face plate at midspan, which grows as the load reduces during unstable postbuckling, while for the analytical model, progressing down the postbuckling path, the localized response tends to resemble cellular behavior somewhat with localized waves spreading towards the edges (Wadee and Bai 2014; Hunt et al 2000; Wadee and Garden 2012; Wadee and Farsi 2014).

For the case where local buckling is critical the FE model generated equilibrium paths that completely bypassed the primary bifurcation and headed directly to the secondary bifurcation which leads to unloading, which can be attributed to the use of geometrical imperfections in the nonlinear analysis.

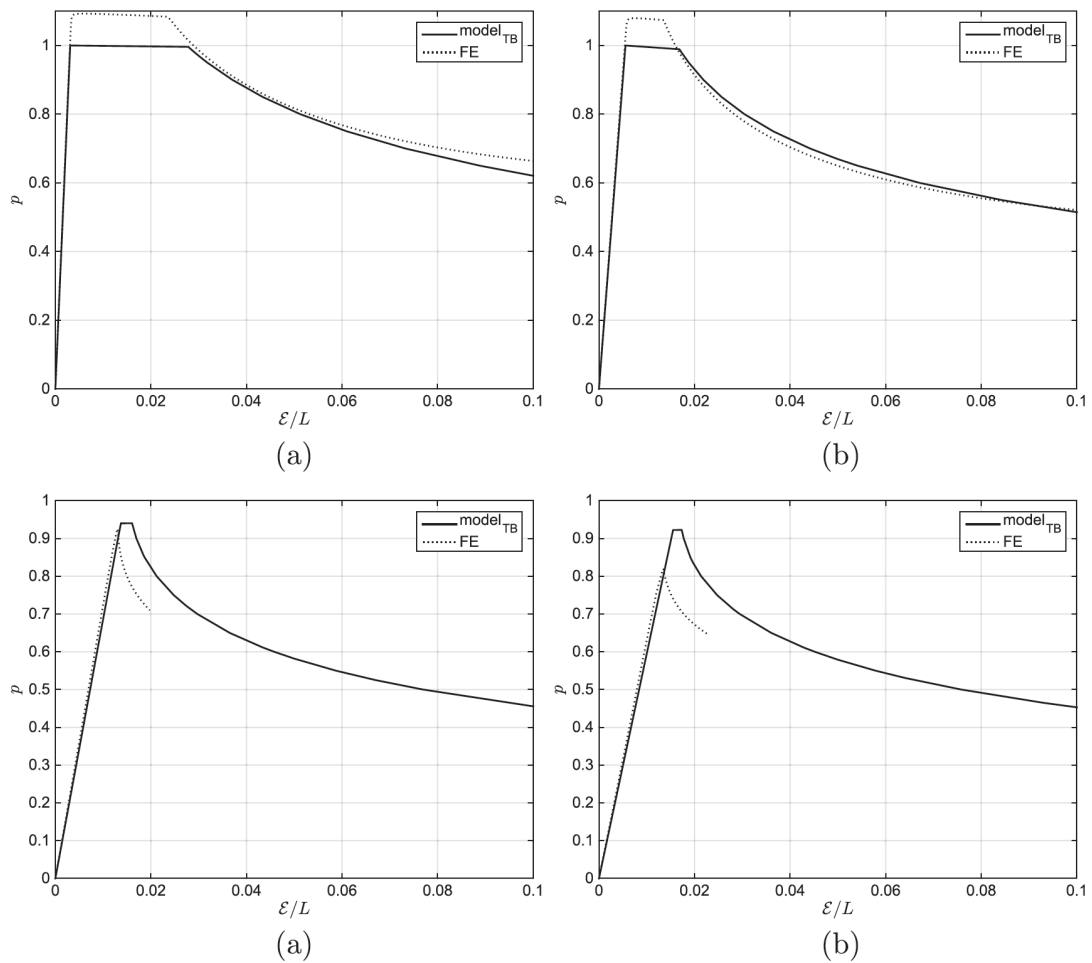


Figure 5.3: Comparison of equilibrium paths for different struts of Length $L = 100\text{mm}$ and core depths of: (a) $b = 5.08\text{mm}$, (b) $b = 7.63\text{mm}$, (c) $b = 16\text{mm}$ and (d) $b = 18\text{mm}$. (a) - (b) Overall buckling is critical; (c) - (d) Local buckling is critical.

Even though this also applies to the critical overall buckling case, the extremely close proximity of the two bifurcation points in the case where local buckling is critical makes the effect more pronounced. The close proximity of the primary and secondary bifurcations when local buckling is critical, has also been observed in the work of Le Grogneq and Saoud (2015) who studied nonlinear postbuckling of sandwich struts, for differing boundary conditions. Nevertheless, the unloading pattern of the postbuckling path are in good agreement in terms of the rate of unloading, with the two curves being essentially parallel.

The deformed shapes at equal normalized end shortening also agree very

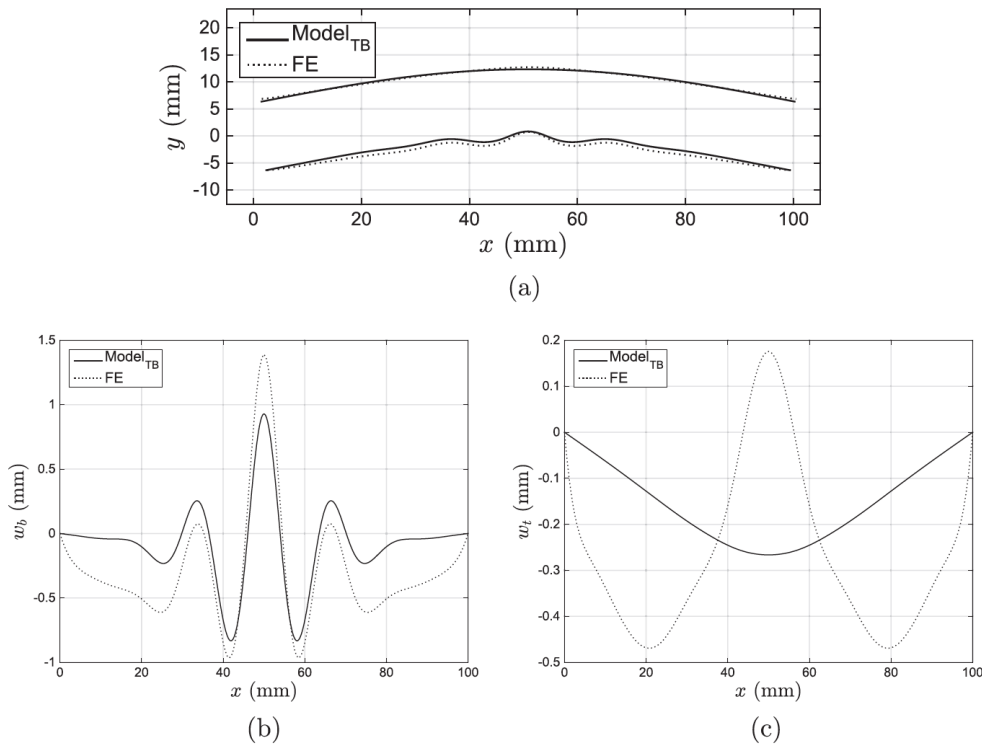


Figure 5.4: Comparison of deformation profiles from the analytical model and FE simulations for strut of depth $b = 12.7\text{mm}$ and length $L = 100\text{mm}$ at $\mathcal{E}/L = 2/2\%$. (a) Total deformations; (b) bottom face plate local deformations w_b and (c) top face plate local deformations w_c .

well, the wavelength and the amplitude of localization match well for the bottom face plate, as shown in Figure 5.4(a). The numerical simulations in all cases exhibited local deformations on the top face plate, diverging from the classical overall eigenmode with associated localized buckling in the bottom face plate. To evaluate the amplitude and nature of the local deformations on either face plate approximately, a half-sine wave is subtracted from the top and bottom face plate deformations. For the top face plate, the local deformations are mostly quasi-periodic in nature, starting with a negative displacement and later forming one or more crests, depending on the length of the strut. The main difference between the numerical simulations and the analytical model is that, in the far post-buckling range, the top face plate deformations in numerical simulations seem to be influenced by the bottom face plate localized mode, with a kink appearing at midspan, as shown in Figure 5.4(b) and (c).

This phenomenon is deliberately not modeled in the analytical model such that the model remains fairly simple in concept, otherwise non-local effects may become important, with one face plate strongly influencing the other, while the large displacement analysis in the finite element simulation, locks the localized mode in the more compressed face plate to such an extent that it essentially affects the less compressed face plate, at midspan. In the absence of this, away from midspan, the deformations seem to agree well both in nature and magnitude. For deeper struts, where local buckling is critical, there is also excellent agreement between the analytical model and the FE simulations in terms of the confinement of the localized mode at midspan, as seen in Figure 5.5. The difference in the amplitude of sway, observed in Figure 5.5(a), can be attributed to the difference in end shortening between the equilibrium paths at the same load level. Looking in detail at the decomposed local deformations, the numerical simulations are in very good agreement with the analytical results in terms of wavelengths. The only differences observed are some smaller amplitude higher frequency waves in the FE simulations, as seen in Figure 5.5(c), which may be attributed to the local imperfection that was used to initiate the nonlinear analysis, as well as the propagation of the more compressed face plate interactive mode, which contaminates the response. In terms of the amplitudes, some of the less stiff behavior of the overall panel and the bottom face plate can be attributed to the neglecting of the axial stiffness of the core, which increases in significance for panels with deeper cores.

5.5.1 Conclusions

A numerical Finite Element model is developed in order to simulate the full post-buckling response of linear elastic, sandwich strut. The results from Finite Element model shows good agreement with analytical model in terms of critical loads for the case when the overall buckling is critical, even in the case when the local buckling is critical. Comparing the Finite Element equilibrium

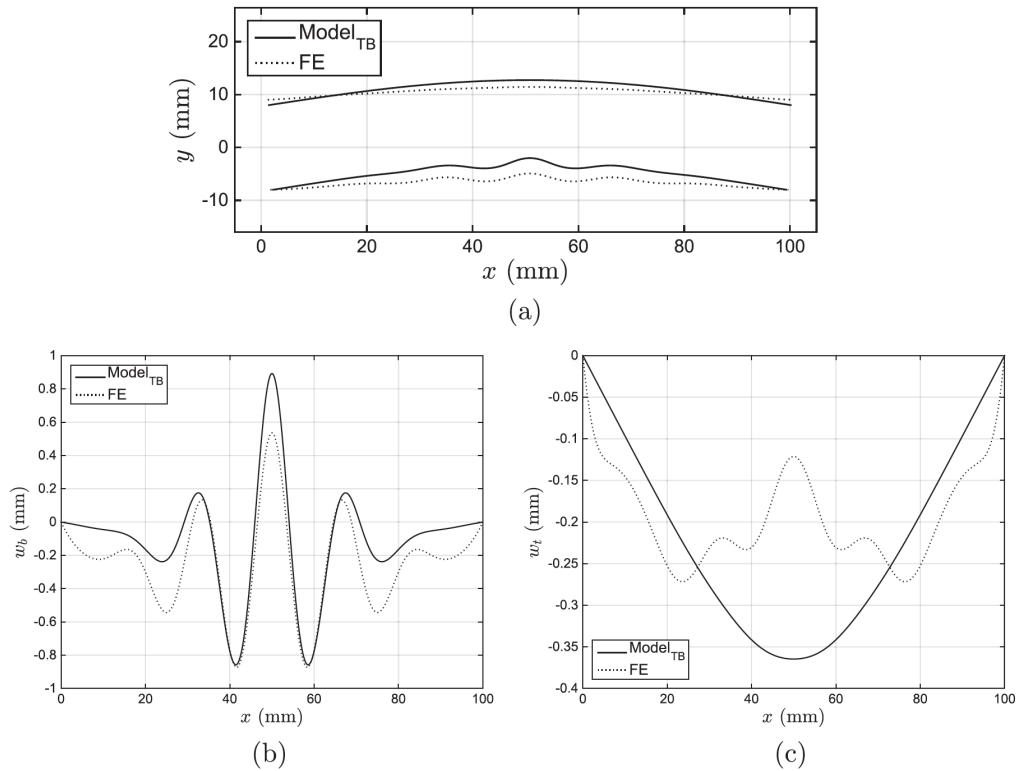


Figure 5.5: Comparison of deformation profiles from the analytical model and FE simulations for strut of depth $b = 16\text{mm}$ and length $L = 100\text{mm}$ at $p = 0.80$. (a) Total deformation; (b) bottom face plate local deformations w_b and (c) top face plate deformations w_t . Note that the FE results in (a) is possibly affected by the selected imperfection used to trigger buckling in the nonlinear analysis.

paths for different strut depths match well with the analytical model results. The difference where local buckling is critical for the Finite Element simulation can be attributed to the use of geometrical imperfections in the nonlinear analysis. However, the results show good agreement with the Finite Element results which also capture the inhomogeneous quasi-periodic deformation in the less compressed face plate.

5.6 Comparison of FE simulations with mechanical results from Chapter 4

The difference in the response of the two analytical models in Chapter 4, specifically in the position of the secondary bifurcation, led to the development

of a nonlinear finite element formulation in ANSYS. The functionally graded core is discretized vertically in horizontal strips. The gradation in the material properties is approximated by having a large number of strips of different properties. As seen in Figure (5.6) it was found that 20 strips across the core depth were sufficient to provide a reasonably smooth transition in the properties and more importantly avoid unwanted numerical errors. The property of each strip (Figure 5.7) is the value of the property at its mid-height which is derived from the below gradation function which was implemented in the analytical model:

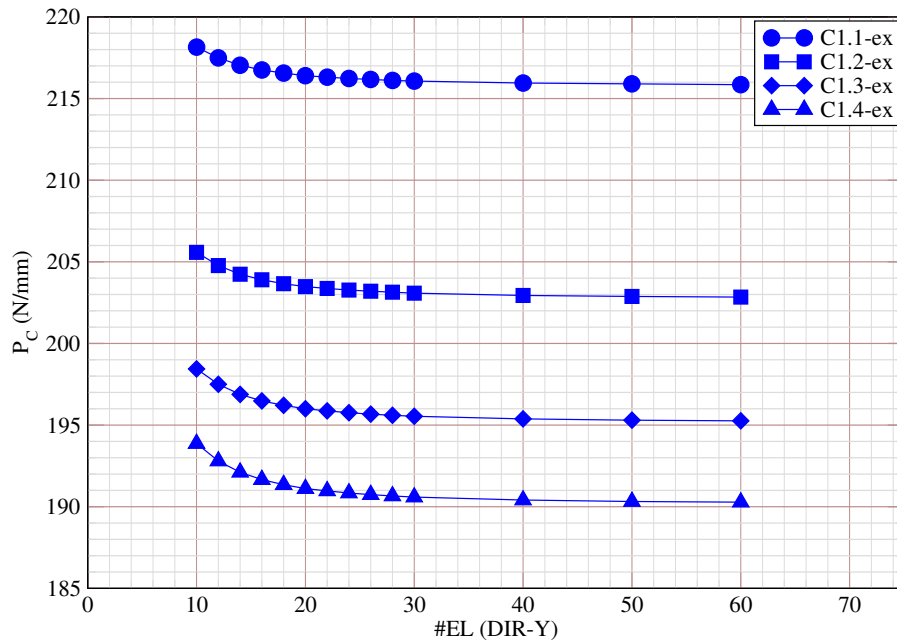


Figure 5.6: Plotting $P(N/mm)$ over the number of elements in the core thickness.

$$\begin{aligned}
 X(y) = \frac{X_C}{dy} \left[a_0(y_2 - y_1) + \frac{a_1}{3b^2} (y_2^3 - y_1^3) + \frac{a_2}{5b^4} (y_2^5 - y_1^5) \right. \\
 \left. + \frac{a_3}{7b^6} (y_2^7 - y_1^7) + \frac{a_4}{9b^8} (y_2^9 - y_1^9) \right] \quad (5.10)
 \end{aligned}$$

For each parametric study two types of simulation are performed. Firstly,

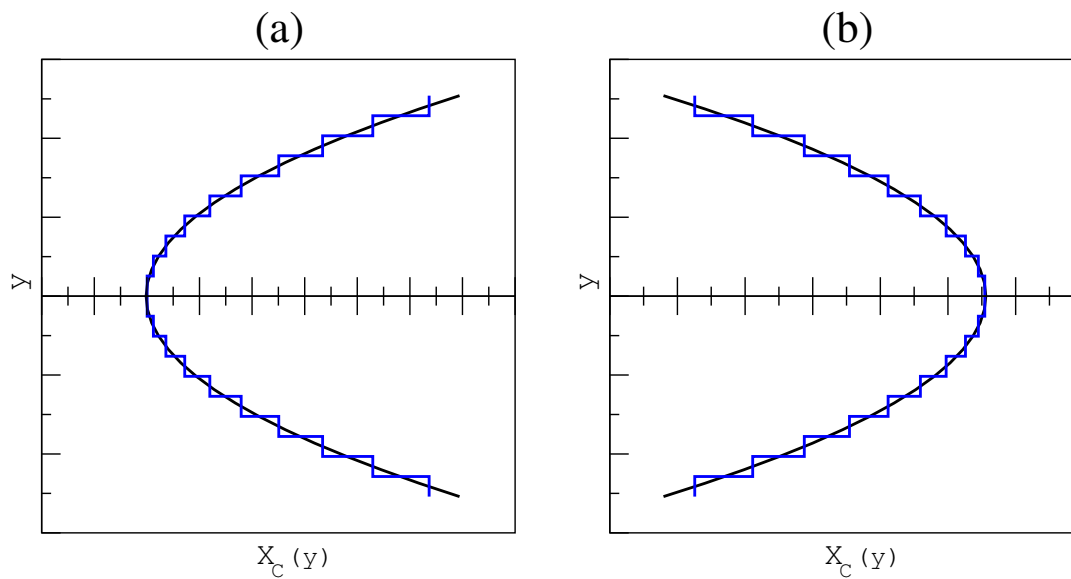
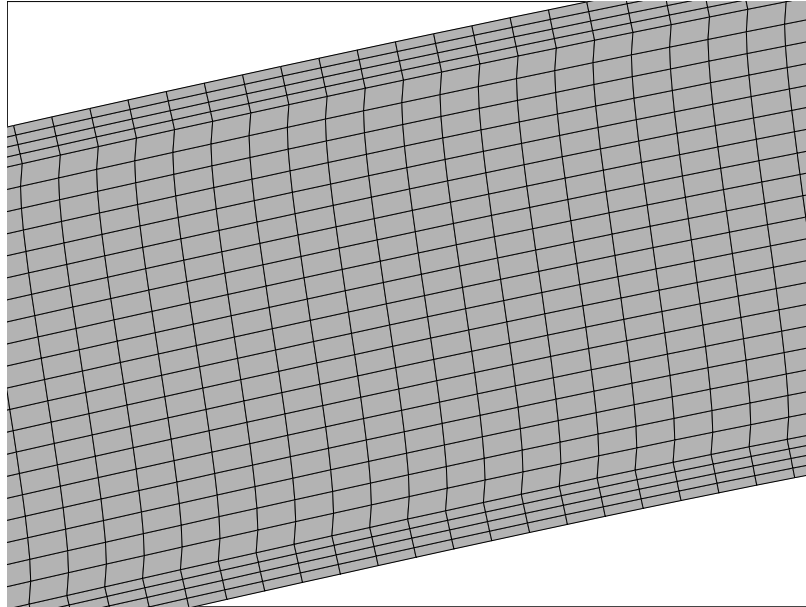
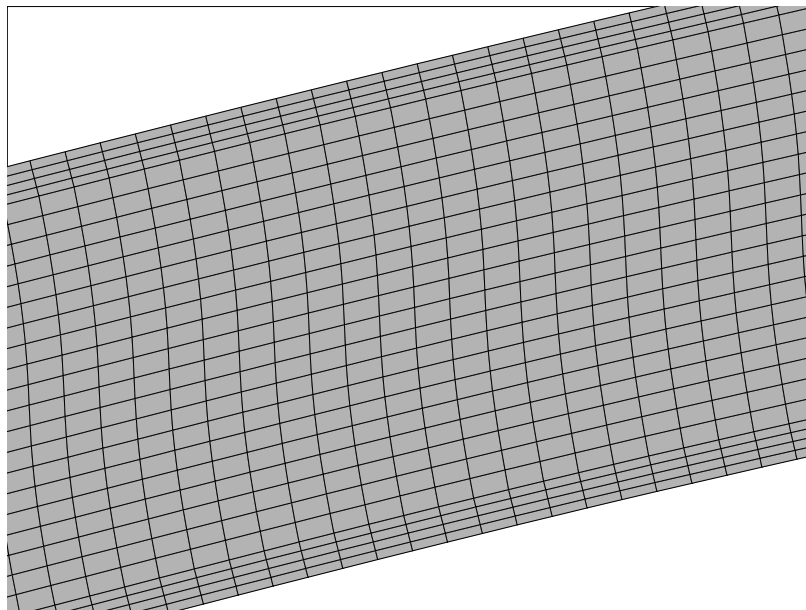


Figure 5.7: The variation in the core materials properties through its the depth of the core and the approximation used in the FE simulation for a sandwich strut. The same FE approximation used for the other gradation modes.

a linear perturbation analysis to capture the overall buckling mode and the corresponding critical load is performed. Table 5.2 shows the critical load for convex and concave parametric studies for different gradation patterns from the linear perturbation, the comparison with the TBT model is even favourable for the convex parametric study and RBT model for the concave parametric study. Qualitatively, regarding the mode shape, the FE simulation shows good agreement with the RBT model since the cross-sectional displacement seems to be increasing towards the extreme edges in the convex parametric study as shown in Figure 5.8(a). For concave parametric study which implies higher stiffness further from the neutral axis, the shear strain is seen to be maximum and localized at the neutral axis (Figure 5.8(b)).



(a)



(b)

Figure 5.8: A schematic of the in-plane displacement due to overall buckling as this was seen in the finite element simulations at quarter length along the length of the strut (a) Convex parametric study; (b) Concave parametric study.

Case	$P_{TBT}^C(N/mm)$	$P_{RBT}^C(N/mm)$	$P_{FE}^C(N/mm)$	TBT % diff	RBT %diff
C1.1-ve	276.77	253.16	268.99	2.89%	5.88%
C1.2-ve	276.89	232.24	252.91	9.48%	8.17%
C1.3-ve	276.96	221.92	242.79	14.07%	8.60%
C1.4-ve	276.00	216.14	236.59	16.65%	8.64%
C1.1-ex	276.24	335.44	269.42	2.53%	24.50%
C1.2-ex	276.31	325.72	279.26	1.06%	16.63%
C1.3-ex	276.34	320.44	285.49	3.20%	12.24%
C1.4-ex	276.37	317.17	289.00	4.47%	9.74%

Table 5.2: Comparison the critical load of FE ana analytical models

Using the overall buckling mode shape as an imperfection of size $L/10000$, as before, a nonlinear analysis is then performed in order to capture the full post-buckling response of the nearly perfect struts. The displacement control incremental method is used and the applied load is found from the reaction force. Examining the position of the secondary bifurcation point, for different convex gradation patterns (Figure 5.9(b)), the RBT model seems to be superior in capturing the trend which shows that the gap widening between the critical and secondary bifurcation points increases when the gradation pattern is similar homogeneous material C1.4ex. As can be seen from the equilibrium paths shown in Figure 5.10, the equilibrium paths predicted by the RBT model have a similar evolution for the postbuckling response with the FE simulation indicating a constant drop in the load carrying capacity (at $0.70P^C$ for normalised end shortening 3%), which remains approximately constant throughout.

The situation is reversed for the concave parametric study, which shows the TBT model predicting the position of the secondary bifurcation points and the initial postbuckling paths quite closely, as can be seen in Figure 5.9(d), with excellent agreement in the residual postbuckling load capacity. It should be noted that even though the RBT model marginally overestimates the plateau

between the critical and secondary bifurcations, it exhibits a good comparison of the postbuckling path with a very good load prediction.

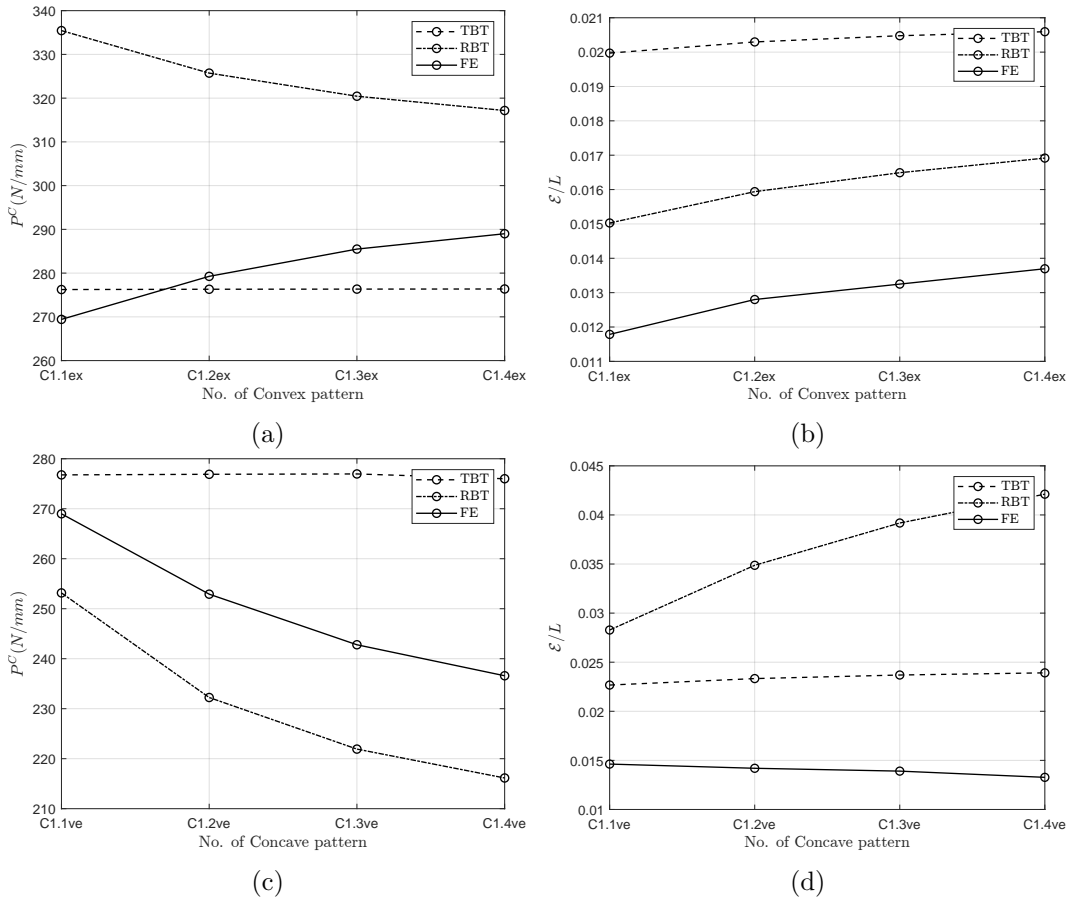


Figure 5.9: (a)&(c) Comparison of the critical loads from the two analytical models and FE simulations for different gradation patterns pattern. (b)&(d) The variation of the position of the secondary bifurcation for different gradation patterns.

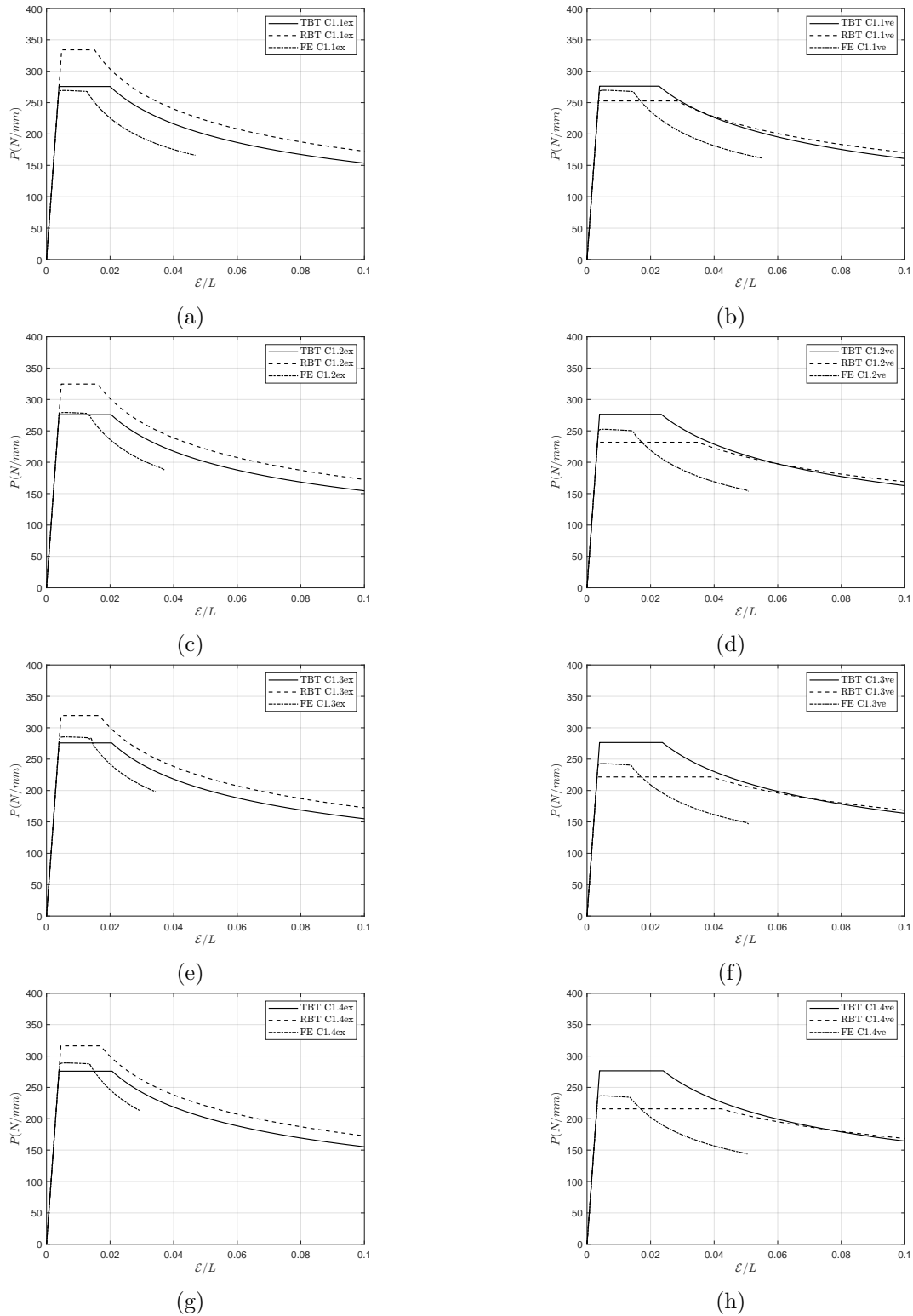


Figure 5.10: Left: Convex case. Right: Concave case. Equilibrium paths for strut for length 100mm and depth 6mm. (a)-(b) TBT model, (c)-(d) RBT model, (e)-(f) FE model.

5.6.1 Conclusions

Two analytical models based on different shear deformable bending theories, have been adapted to investigate the interactive buckling of sandwich struts with functionally graded cores. The analytical models have been compared with the Finite Element simulations implemented in ANSYS, exhibiting a good correlation. In the first parametric study, with a convex stiffness distribution, the RBT model exhibits a better correlation with the Finite Element simulations especially on the onset of interactive buckling since the displacement field shows an approximately cubic distribution. The amplification of the difference in the critical load is indicative of the limitation of Equivalent Single Layer approaches which tend to overestimate critical loads. For the second parametric study, with concave stiffness distribution, the TBT model seems to provide an excellent comparison for the position of secondary bifurcation points. The reason for the excellent correlation can be attributed to the in-plane displacement field is approximately linear except very locally near the neutral axis.

Chapter 6

Discussion

Elastic stability is practically important for engineers responsible for designing safe structures. If our sole concern was to understand the initial stages of buckling of such bodies, then a suitable model consisting of linearized equations would serve the purpose. On the other hand, deeper appreciation of the true nature of the instabilities together with knowledge of the subsequent responses of failure mechanisms requires that nonlinear effects be included as well. In the overwhelming majority of postbuckling scenarios, exact analytical solutions do not exist and so necessarily, we have to resort to approximation, be it fully numerical or a simplification of the full system followed by analysis in various limited ranges (Thompson and Hunt 1973). Both of these strategies can reveal behaviour which is of interest not only to engineers but also to applied scientists. Instability phenomena are becoming of increasing importance in many fields and some previous studies are being given renewed prominence owing to the discovery of physical phenomena down to the atomic level which these theories seem to model well (Lee et al 2008). It is in this spirit that herein we study mode interaction and localization in sandwich struts.

In the current thesis, the interactive postbuckling behaviour of a sandwich

strut has been successfully investigated using analytical and Finite Element methods. An analytical approach presents a novel contribution to the field and has added to the understanding of interactive buckling phenomena. The energy method has been utilized extensively in the field of interactive buckling phenomena for sandwich structures, the interaction being, in general between overall buckling and local buckling. The potential energy method used for these studies to describe the global buckling mode first, using at least a two degree of freedom system; “sway”, indicating the lateral displacement and “tilt”, for the rotation of the plane. Two mechanical models were developed based on two different shears deformable bending theories, that allow the development of shear strains within the core. The first model is based on the Timoshenko Beam theory (TBT), which assumes a constant shear strain distribution across the core, the second model is based on the third-order Reddy-Bickford Theory (RBT) which assumes a higher order shear strain distribution across the core. For local buckling, the out-of-plane and in-plane deflections in the transverse directions are solved by introducing mathematical functions for the in-plane and out-of-plane local displacements. The Total Potential Energy is formulated. By using the calculus of variations, a system of governing equations is subsequently found by considering the variations of the out-of-plane and in-plane displacements, and minimizing the Total potential energy with respect to sway and tilt degrees of freedom. The system of governing equations is the solved numerically in the continuation and bifurcation software AUTO-07p. The software is capable of identifying bifurcation and branching points; thus, the equilibrium paths and corresponding deflection shapes can be determined.

This thesis is divided into two parts. In the first part, a nonlinear analytical model for investigating localized interactive buckling in simply supported, thin-face plate sandwich struts with weak cores, is extended to account for local deformations in both face plates. In the second part, analytical models were

developed to cater for Functionally Graded Material's in the core. Using these models, the interactive buckling phenomenon is captured and investigated for different gradation patterns.

6.1 Modelling localized buckling in sandwich struts with inhomogeneous deformations in both face plates

An analytical model based by Hunt and Wadee (1998) model were developed in order to account local deformations of the face plate on the least compressed side of the panel. This phenomenon, which the smaller local deformations begin to appear almost right after the secondary bifurcation when interactive buckling at the second face plate has been triggered, it has been observed both experimentally and Finite Element simulations. The results from the analytical model are compared with the results obtained from Finite Element simulations performed in ANSYS.

First comparing the results obtained from Hunt and Wadee (1998) model, the results showing that the local deformations in the less compressed face plate play a negligible influence in the mechanical response of the sandwich strut. Second, comparing the results obtained from Finite Element simulations, the numerical results show inhomogeneous deformations in the least compressed face plate. The differences between analytical and Finite Element model are mainly due to the assumptions that have been use but also to the way the problem is solved with finite elements, as well as to the assumptions of the analytical model. A typical difference is that in Finite Element simulations there are boundary points, in contrast to the analytical model there are branches.

Another difference is that in the analytical model there is no imperfection but a specific deformation has been delivered to the core, on the other hand in the Finite Element model the geometric imperfection that was used to initiate the nonlinear analysis has more freedom and is based on the degree of discretization. As described in Chapter 5, the Finite Element model considers the face plate and core are uniform discretized with two dimensional solid element. In order to minimize the difference between the results of analytical and finite model could be optimized the mesh with more nodes and elements between core face plate interface. Moreover, owing to the small thickness of a face plates the Finite Element model will be considered as two-dimensional linear elements bonded to the edges of the core with specific suitable engineering properties.

6.2 Modelling interactive buckling for FGM sandwich struts

Two analytical models based on two different shear deformable bending theories have been enhanced to allow Functionally Graded Material (FGM) core. The first model is based on the Timoshenko beam theory and the second model is based on higher-order Reddy-Bickford beam theory. In order to describe the functionally graded material core we have used polynomial function to create a gradation in stiffness (Young's and Shear Modulus) which could be realised via changes in the density of a porous material. The polynomial equation except from the ease of modelling and being adaptable, has the ability to investigate various mechanical properties gradation patterns. Two types of parametric studies with different gradation distributions through the depth of the core investigated in order to capture interactive buckling phenomena. In the first parametric study "Convex" distribution, the Young's modulus is maximum at the neutral axis and reduces further away from it, and the second

parametric study, “Concave” distribution, the Young’s modulus is minimum at the neutral axis and increases further away from it. The results from the analytical models are compared with the results obtained from Finite Element simulations performed in ANSYS.

Comparing the results, the two analytical models exhibited different results regarding the critical buckling load and the position of the secondary bifurcation point. The difference between the two models lies in the way the gradation in the core stiffness is treated. The RBT model based on third-order theory, assuming quadratic distribution of shear strain, which is maximum in the middle and zero at the core interface, makes the model more versatile to adapt the convex gradation than the TBT model. On the other hand, the TBT model which assumes that the shear strain is constant across the depth of the core, makes the model adequate for concave gradation.

Summarizing all of the above findings, the two analytical models based on different bending theories seem to have quite distinct ranges of applicability, depending on the material configurations as has been shown from the finite element results. The RBT model exhibited a very good correlation with Finite Element simulations for the convex parametric study and TBT model for concave parametric study. A typical difference that was observed between analytical and Finite Element results, are due to the assumptions that have been used. In order to describe the functionally graded material in the core, the core in the finite element model is discretized uniform in horizontal strips. It was found that 20 strips across the core depth were sufficient to provide a reasonable smooth transition. Nevertheless, differences were observed between the results of analytical and Finite Element models. In order to minimize the error could be optimized the element discretized. For the convex parametric study where the material is relatively compliant at core interfaces and stiffer

at the mid-height of core, the Finite Element model could be minimized by refining the mesh with more nodes and elements at the mid-height of core. On the other hand, for concave parametric study where the stiffer core are at the face core interface, the Finite element model can be minimized by refining the mesh with more nodes and element between core face plate interface. In conclusion, further study will be needed to optimize the element discretize, in order to minimize the error between analytical and finite element models.

Chapter 7

General conclusions and further work

7.1 Conclusions

The thesis herein presented the development of series of analytical models to capture mode interaction in the elastic range between buckling modes and localization in sandwich struts with a soft core material. Building on an existing variational model which was based on Timoshenko beam theory and Reddy-Bickford beam theory (Hunt and Wadee 1998; Wadee et al 2010), enhanced models have been developed and adapted to examine interactive buckling for different geometric, and material, attaching particular importance to the onset of the instabilities.

Firstly, a nonlinear analytical model extended to account for local deformations in both face plates, which have been observed in experiments and finite element simulations. The original model was based on total potential energy principles with large displacement assumptions. The model was assumed a simply-supported strut with a linear elastic core and was compared against

the previous formulation (TBT) (Wadee and Hunt 1998); exhibiting a safer prediction of the secondary bifurcation point, which is known to pinpoint the onset of interactive buckling that causes destabilization of the postbuckling path. The extended model was able to capture measurable local face plate displacements in the less compressed face plate, beyond the secondary bifurcation which leads to localized interactive buckling, for the case where overall buckling is critical. The results showed that the local deformations in the less compressed face plate play a negligible influence in the mechanical response of the sandwich strut, for the thickness considered and where overall buckling was critical. More importantly for this current study, that the model was capable of dealing with the case where local buckling was critical. This case exhibits a very close proximity between the primary and secondary bifurcations and a severely unstable response is the result, which would translate into a high degree of imperfection sensitivity. The results of this work were published in *Composite Structures* (Yiatros et al 2015).

The second part of the work presented herein was dedicated to the application of functionally graded materials and their effect on triggering of interactive buckling. A study was initiated for a simply-supported sandwich strut with an elastic core whose material properties were varying across its depth. Two parametric studies where the stiffness decreases (convex distribution) or increases (concave distribution) from the neutral axis outwards have been considered since the former can be used in a minimum weight design strategy while the latter has been to reduce the risk of delamination and fracture. The analytical models have been adapted with changes in the potential energy to reflect the varying material properties across the depth of the core. The two models exhibited different results about the critical buckling load and the position of the secondary bifurcation point. The RBT model provides a safer estimation for convex parametric study, on other hand, for the concave parametric study

the TBT model provide excellent results for the position of secondary bifurcation points and post-buckling paths. These results have been presented at the EMI2021 Conference (Georgiou and Yiatros 2021).

The last part of the work involved the development of a nonlinear finite element formulation was developed in ANSYS. The model was created, using 2-dimensional solid elements for both the core and the face plates. In order to match the analytical models as closely as possible, the core depth was modeled as $b - t$. The left edge elements were free to rotate about a master element at mid-sections which were constrained in the vertical direction. On the right edge, simply supported conditions were imposed by restricting horizontal and vertical displacements of the master element, while the remaining elements were free to rotate about the master element. Initially, a linear eigenvalue analysis was used to find the individual buckling modes, which were then input as initial imperfections into a nonlinear model solved using Arc-length analysis. Comparing the results by analytical model of Chapter 3, the results have shown good agreement with the Finite Element results which also capture the inhomogeneous quasi-periodic deformations in the top (less compressed) face plate.

Finally, comparing the results for the analytical model of Chapter 4, the finite element model have been adapted to reflect the varying material properties across the depth of the core. More precisely, the RBT model exhibited an excellent correlation with the FE simulation for the convex parametric study where reduced stiffness outwards from the neutral axis for on the onset of the instability, even though it overestimated the critical load. The TBT model was superior for the concave parametric study, matching both the onset of interactive buckling, critical load and initial postbuckling path more closely. The reasons for the range of applicability of each corresponding model can be

found in the different in-plane displacement field used by each analytical model. As shown from the FE simulation each model approximated the in-plane displacement through the depth of the core more closely than the other for each respective case, thus better estimating the actual bending stress responsible for triggering interactive buckling.

7.2 Originality

Sandwich structures are well-known in many engineering disciplines as a versatile structural solution with a favorable combination of low weight and high bending stiffness. However, they are prone to instability phenomena such as overall buckling and wrinkling. These phenomena are triggered at certain critical loads with sandwich structures buckling either globally or locally in each face plate in a symmetric or antisymmetric. Since sandwich structures can fail in various mode, in this thesis, the interactive buckling phenomena of sandwich struts were investigated by developing analytical models. This thesis divided into two parts.

- The first part of thesis is direct continuation of the work of Hunt and Wade (1998) in order to capture localized deformation that occurs at the both face plates. An analytical model based on Timoshenko beam theory developed and the results compared with Finite Element simulations. The results of this work were published in Composite Structures (Yiatros et al 2015)
- Second part of thesis continues in a different direction, the materials optimization. Although, standard sandwich structures offer advantages over homogenous structures, in this thesis investigated other novel sandwich technologies in order to obtain optimum design response. One

such alternative is represented by sandwich structures with functionally graded core.

- Two analytical model based on different theorys, are developed for sandwich structures with functionally graded core, in order to see whether particular stiffness functional gradations, could be used as part of a design mitigation strategy to delay or ameliorate buckling.
- In order to describe the functionally graded material core we have used polynomial function to create a gradation in stiffness (Young's and Shear Modulus) which could be realised via changes in the density of a porous material.
- The results compared with Finite Element simulations.
- The results have been presented at the EMI2021 Conference (Georgiou and Yiatros 2021).

7.3 Further work

The widespread use sandwich structures with functionally graded material in industry offers a plethora of problems to be investigated for which the aforementioned models could be extended to cover. An obvious extension is the investigation of interactive buckling and localization on a sandwich beam under 3-point bending, a standard test of sandwich beams and continuous lateral loading. Such an extension would require different displacement functions, more appropriate to the loading scenario.

Furthermore, a possible extension of the model is to investigate the initiation and propagation of delamination at the face plate - core interface due to

interactive buckling. Delamination related issues are quite frequent in practice and may lead to catastrophic failure due to a sudden loss of local stiffness. Even though delamination is usually caused by impact, examining its initiation due to localized buckling and, more importantly, its propagation can be informative since the possible results of this investigation can shed more light onto the mechanism of failure and help engineers to adopt better procedures to account for it.

The current analytical model only limit to the linear elastic material properties. However, the sandwich struts with imperfection levels is mainly governed by material failure. Therefore, including the nonlinear effects of the material in the variational model would help to understand the underlying mechanism in the failure of sandwich structures in realistic scenarios better.

As far as the author knows, the current analytical and numerical model has not been validated with experimental results. However, experimental tests to capture interactive buckling phenomena using digital image correlation techniques through photogrammetric methods is necessary to validate the analytical models results (Sinur et al 2012; Skarlatos and Yiatros 2016).

Finally, an analytical approach presents a novel contribution to the field and has added to the understanding of complex interactive buckling phenomena in popular structural components. Developments have also been made towards the understanding of structural imperfection sensitivity, with some preliminary suggestions of how this research can be implemented in engineering design.

Appendix A

Non-Dimensionalization of system equations of Chapter 4

In Chapter 4, having formulated the necessary equations, in order to establish the nontrivial interactive modes the system of governing ordinary differential equations, integral constants and boundary conditions was non-dimensionalized and solved numerically using AUTO-07p (Doedel et al 2012). As its name implies AUTO is a solver for autonomous equations. However it can solve non-autonomous equations, such as the system derived currently, by introducing another variable. This would transform the sixth order ($w, \dot{w}, \ddot{w}, u, \dot{u}$) non-autonomous system into a seventh order system with the inclusion of \tilde{x} variable that takes values between 0 and 1, and represents the spatial parameter along the length of the panel. The spatial coordinate along the length x is non-dimensionalized such that:

$$x = L\tilde{x} \tag{A.1}$$

where, $\tilde{x} = 0$ at one end and $\tilde{x} = 1$ at the other end. Another note is that it normalizes the terms in the solution matrix making the matrix numerically less stiff and computation more efficient. The non-dimensionalization of the potential

energy of the system and all the terms in u and w given as:

$$V = \int_0^L \mathcal{L}[w, \dot{w}, \ddot{w}, u\dot{u}] \, dx = \int_0^1 \mathcal{L}\left[L\tilde{w}, \tilde{w}, \frac{1}{L}\tilde{\dot{w}}, L\tilde{u}, \tilde{\dot{u}}\right] \, d\tilde{x} \quad (\text{A.2})$$

The non-dimensionalized total potential energy for TBT given as:

$$\begin{aligned} \tilde{V}_T = \int_0^L \left\{ \left[\frac{\tilde{w}^2}{2} + \frac{\tilde{q}_s^2}{\phi^2} \sin^2(\pi\tilde{x}) \right] + \tilde{D} \left[2\Delta^2 + \frac{\tilde{w}^4}{4} + \frac{\tilde{q}_t^2}{2} \sin^2(\pi\tilde{x}) \right. \right. \\ \left. \left. + \tilde{u}^2 + \tilde{u}\tilde{w}^2 - \tilde{q}_t \left(\tilde{u} + \frac{\tilde{w}^2}{2} \right) \sin(\pi\tilde{x}) - 2\Delta \left(\tilde{u} + \frac{\tilde{w}^2}{2} \right) \right] \right. \\ \left. + \tilde{C}_x \left[\frac{\tilde{w}^4}{20} f_5 + \frac{\tilde{u}^2}{3} f_2 + \frac{\tilde{w}^2\tilde{u}}{4} f_4 - \Delta \left(\tilde{u} f_1 + \frac{\tilde{w}^2}{3} f_2 - \Delta f_1 \right) \right. \right. \\ \left. \left. + \frac{\tilde{q}_t}{12} f_3 \sin(\pi\tilde{x}) \left(\tilde{q}_t \sin(\pi\tilde{x}) - \tilde{w}^2 - 2\tilde{u} \right) \right] \right. \\ \left. + \tilde{C}_y \left[\Delta \nu_x^2 \left(\tilde{u} f_1 + \frac{\tilde{w}^2}{3} f_2 - \Delta f_1 \right) - \nu_x \frac{\tilde{w}}{\phi} \left(\tilde{u} f_1 + \frac{\tilde{w}^2}{3} f_2 \right) \right] + \frac{1}{2} \tilde{k} \tilde{w}^2 f_1 \right. \\ \left. + \frac{\tilde{G}}{\phi} \left[\cos^2(\pi\tilde{x}) \frac{1}{\pi^2} (\tilde{q}_s - \tilde{q}_t)^2 f_1 - (\tilde{q}_s - \tilde{q}_t) \frac{2\phi}{\pi} \cos(\pi\tilde{x}) \left(\frac{\tilde{u}}{\phi} - \frac{\tilde{w}}{2} \right) f_1 \right. \right. \\ \left. \left. + \tilde{u}^2 f_1 + \frac{\tilde{w}^2 \phi^2}{3} f_2 - \tilde{w} \tilde{u} \phi f_1 \right] - \tilde{P} \tilde{G} \phi \left[2\Delta + \frac{\tilde{q}_s^2}{\phi^2 \pi^2} \cos^2(\pi\tilde{x}) - \tilde{u} \right] \right\} \, dx \quad (\text{A.3}) \end{aligned}$$

and for RBT the non-dimensionilzed total potential energy given as:

$$\begin{aligned}
 \tilde{V}_R = \int_0^L \left\{ \left[\frac{\tilde{w}^2}{2} + \frac{\tilde{q}_s^2}{\phi^2} \sin^2(\pi\tilde{x}) \right] + \tilde{D} \left[2\Delta^2 + \frac{\tilde{w}^4}{4} + (2\tilde{q}_t + \tilde{q}_s)^2 \frac{1}{18} \sin^2(\pi\tilde{x}) \right. \right. \\
 + \tilde{u}^2 + \tilde{u}\tilde{w}^2 - (2\tilde{q}_t + \tilde{q}_s) \frac{1}{6} \sin(\pi\tilde{x}) (2\tilde{u} + \tilde{w}^2) - 2\Delta \left(\tilde{u} + \frac{\tilde{w}^2}{2} \right) \left. \right] \\
 + \frac{\tilde{C}_x}{1260} \left[(5\tilde{q}_s^2 f_6 + 32\tilde{q}_t \tilde{q}_s f_7 + 68\tilde{q}_t^2 f_9) \sin^2(\pi\tilde{x}) \right. \\
 - 21 \sin(\pi\tilde{x}) (\tilde{q}_s f_3 + 4\tilde{q}_t f_8) (2\tilde{u} + \tilde{w}^2) + 315\tilde{u}\tilde{w}^2 f_4 + 420 f_2 (\tilde{u}^2 - \tilde{w}^2 \Delta) \\
 \left. + 1260 f_1 (\Delta^2 - \tilde{u}\Delta) + 63\tilde{w}^4 f_5 \right] \\
 + \tilde{C}_y \nu_x \left[\Delta \nu_x \left(\tilde{u} f_1 + \frac{\tilde{w}^2}{3} f_2 - \Delta f_1 \right) - \frac{\tilde{w}}{\phi} \left(\tilde{u} f_1 + \frac{\tilde{w}^2}{3} f_2 \right) \right] + \frac{1}{2} \tilde{k} \tilde{w}^2 f_1 \\
 + \frac{\tilde{G}}{\phi} \left[\frac{8}{15\pi^2} \cos^2(\pi\tilde{x}) (\tilde{q}_s - \tilde{q}_t)^2 f_{11} - \frac{2\phi}{3\pi} (\tilde{q}_s - \tilde{q}_t) \cos(\pi\tilde{x}) \left(\frac{2\tilde{u}}{\phi} - \tilde{w} \right) f_{10} \right. \\
 \left. + \tilde{u}^2 f_1 + \frac{\tilde{w}^2}{3} \phi^2 f_2 - \tilde{w}\tilde{u} f_1 \right] - \tilde{G}\tilde{P}\phi \left[2\Delta + \frac{\tilde{q}_s^2}{\pi^2 \phi^2} \cos^2(\pi\tilde{x}) - \tilde{u} \right] \left. \right\} dx
 \end{aligned} \tag{A.4}$$

where the constants f_i for both models given by the Equations (4.7) and 4.9), respectively. The terms by the Equation (2.28) in a non-dimensional form given below:

$$\begin{aligned}
 V &= \frac{EI}{L^2} \tilde{V}, & D &= \frac{EI}{L^2} \tilde{D}, & C_x &= \frac{EI}{L^2} \tilde{C}_x, & C_y &= \frac{EI}{L^2} \tilde{C}_y, & G &= \frac{EI}{L^3} \tilde{G}, \\
 k &= \frac{EI}{L^4} \tilde{k}, & P &= 2G\tilde{P}, & q_t &= \frac{L}{b\pi^2} \tilde{q}_t, & q_s &= \frac{L}{b\pi^2} \tilde{q}_s
 \end{aligned} \tag{A.5}$$

The critical load P^C for the overall mode is normalized for the both models such that:

$$\tilde{P}_T^C = \frac{\pi^2}{\tilde{G}\phi} + \frac{f_1 \left(\tilde{D} + \frac{\tilde{C}_x}{6} f_3 \right)}{\frac{2\tilde{G}}{\phi\pi^2} f_1 + \left(\tilde{D} + \frac{\tilde{C}_x}{6} f_3 \right)} \tag{A.6}$$

$$\tilde{P}_R^C = \frac{\pi^2}{\tilde{G}\phi} + \frac{14\tilde{G}f_{11}(\tilde{C}_xA_1 + 6\tilde{D}) + \frac{\tilde{C}_x\pi^2\phi}{60\tilde{G}}(\tilde{C}_xA_2 + 20\tilde{D}A_3)}{\frac{168\tilde{G}}{\pi^2\phi}f_{11} + 17\tilde{C}_xf_9 + 70\tilde{D}} \quad (\text{A.7})$$

The boundary conditions that is same for the both models are non-dimensionalized as:

$$\tilde{w}(0) = \tilde{w}'(0) = \tilde{w}(1) = \tilde{w}'(1) = 0 \quad (\text{A.8a})$$

$$\tilde{u}(0) \left(2\tilde{D} + \frac{2\tilde{C}_x}{3}f_2 \right) + \tilde{w}^2(0) \left(\tilde{D} + \frac{\tilde{C}_x}{4}f_4 \right) - \Delta \left(2\tilde{D} + \tilde{C}_xf_1 - \tilde{C}_y\nu_x^2f_1 \right) + \tilde{P}\tilde{G}\phi = 0 \quad (\text{A.8b})$$

$$\tilde{u}(1) \left(2\tilde{D} + \frac{2\tilde{C}_x}{3}f_2 \right) + \tilde{w}^2(1) \left(\tilde{D} + \frac{\tilde{C}_x}{4}f_4 \right) - \Delta \left(2\tilde{D} + \tilde{C}_xf_1 - \tilde{C}_y\nu_x^2f_1 \right) + \tilde{P}\tilde{G}\phi = 0 \quad (\text{A.8c})$$

In the same fashion the non-dimensionalized system of equations for TBT are given below for:

$$\begin{aligned} \ddot{\tilde{w}} &+ \tilde{C}_x \left[\frac{2}{3}\Delta\tilde{w}f_2 + \frac{\tilde{q}_t}{6} (\tilde{w} \sin(\pi\tilde{x}) + \tilde{w}\pi \cos(\pi\tilde{x})) f_3 \right. \\ &- \left. \left(\frac{1}{2}\tilde{w}\ddot{\tilde{u}}f_4 + \frac{1}{2}\ddot{\tilde{u}}\tilde{w}f_4 + \frac{3}{5}\tilde{w}^2\ddot{\tilde{w}}f_5 \right) \right] + \frac{\tilde{C}_y\nu_x}{\phi} \left[\frac{2}{3}\tilde{w}\ddot{\tilde{w}}f_2 - \frac{2}{3}\nu_x\Delta\phi\ddot{\tilde{w}}f_2 - \ddot{\tilde{u}}f_1 + \frac{1}{3}\ddot{\tilde{w}}^2f_2 \right] \\ &+ \tilde{k}\tilde{w}f_1 + \tilde{D} [2\Delta\tilde{w} + \tilde{q}_t (\tilde{w} \sin(\pi\tilde{x}) + \tilde{w}\pi \cos(\pi\tilde{x})) - (2\ddot{\tilde{u}}\tilde{w} + 2\tilde{w}\ddot{\tilde{u}} + 3\ddot{\tilde{w}}^2\tilde{w})] \\ &+ \tilde{G} \left[\ddot{\tilde{u}}f_1 - \frac{2}{3}\phi\ddot{\tilde{w}}f_2 + \sin(\pi\tilde{x})(\tilde{q}_s - \tilde{q}_t)f_1 \right] = 0 \end{aligned} \quad (\text{A.9})$$

$$\begin{aligned} 2\ddot{\tilde{u}} \left(\frac{\tilde{C}_x}{3}f_2 + \tilde{D} \right) - \tilde{D} (\tilde{q}_t\pi \cos(\pi\tilde{x}) - 2\ddot{\tilde{w}}\tilde{w}) - \frac{\tilde{C}_x}{2} \left(\frac{\tilde{q}_t}{3}\pi \cos(\pi\tilde{x})f_3 - \ddot{\tilde{w}}\ddot{\tilde{w}}f_4 \right) \\ - \frac{\nu_x\tilde{C}_y}{\phi}\ddot{\tilde{w}}f_1 + \tilde{G}f_1 \left(\ddot{\tilde{w}} - \frac{2\ddot{\tilde{u}}}{\phi} + \frac{2}{\phi\pi} \cos(\pi\tilde{x}) (\tilde{q}_s - \tilde{q}_t) \right) = 0 \end{aligned} \quad (\text{A.10})$$

$$\frac{\tilde{q}_s \pi^2}{\phi} - \tilde{q}_s \tilde{G} \tilde{P} + \tilde{G}(\tilde{q}_s - \tilde{q}_t) f_1 - \tilde{G} \pi \phi f_1 \int_0^L \cos(\pi \tilde{x}) \left(\frac{2\tilde{u}}{\phi} - \tilde{w} \right) dx = 0 \quad (\text{A.11})$$

$$\begin{aligned} & \tilde{G}(\tilde{q}_t - \tilde{q}_s) f_1 + \frac{\tilde{q}_t \phi \pi^2}{2} \left(\tilde{D} + \frac{\tilde{C}_x}{6} f_3 \right) \\ & - \int_0^L \left[\left(\tilde{D} + \frac{\tilde{C}_x}{6} f_3 \right) \phi \pi^2 \sin(\pi \tilde{x}) \left(\tilde{u} + \frac{\tilde{w}^2}{2} \right) + \tilde{G} \pi \phi \cos(\pi \tilde{x}) \left(\tilde{w} - \frac{2\tilde{u}}{\phi} \right) f_1 \right] dx = 0 \end{aligned} \quad (\text{A.12})$$

$$\begin{aligned} & \Delta \left(2\tilde{D} + \tilde{C}_x f_1 - \nu_x^2 \tilde{C}_y f_1 \right) - \tilde{G} \tilde{P} \phi \\ & - \int_0^L \left[\tilde{D} \left(2\tilde{u} + \tilde{w}^2 \right) + \frac{1}{2} \left(\tilde{C}_x - \nu_x^2 \tilde{C}_y \right) \left(\tilde{u} f_1 + \frac{\tilde{w}^2}{3} f_2 \right) \right] dx = 0 \end{aligned} \quad (\text{A.13})$$

For RBT the the non-dimensionalized system of equations given as:

$$\begin{aligned} & \dot{\tilde{w}} + \tilde{C}_x \left[\frac{2}{3} \Delta \tilde{w} f_2 + (\tilde{q}_s f_3 + 4\tilde{q}_t f_8) \frac{1}{30} (\tilde{w} \sin(\pi \tilde{x}) + \tilde{w} \pi \cos(\pi \tilde{x})) \right. \\ & \left. - \left(\frac{1}{2} \tilde{w} \tilde{u} f_4 + \frac{1}{2} \tilde{u} \tilde{w} f_4 + \frac{3}{5} \tilde{w}^2 \tilde{w} f_5 \right) \right] + \tilde{C}_y \nu_x \left[\frac{2\tilde{w} \tilde{w}}{3\phi} f_2 - \frac{2}{3} \nu_x \Delta \tilde{w} f_2 - \frac{\tilde{u}}{\phi} f_1 + \frac{\tilde{w}^2}{3\phi} f_2 \right] \\ & + \tilde{k} \tilde{w} f_1 + \tilde{D} \left[2\Delta \tilde{w} + (\tilde{q}_s + 2\tilde{q}_t) \frac{1}{3} (\tilde{w} \sin(\pi \tilde{x}) + \tilde{w} \pi \cos(\pi \tilde{x})) - (2\tilde{u} \tilde{w} + 2\tilde{w} \tilde{u} + 3\tilde{w}^2 \tilde{w}) \right] \\ & + \tilde{G} \left[\tilde{u} f_1 - \frac{2}{3} \phi \tilde{w} f_2 + \frac{2}{3} \sin(\pi \tilde{x}) (\tilde{q}_s - \tilde{q}_t) f_{10} \right] = 0 \end{aligned} \quad (\text{A.14})$$

$$\begin{aligned} & 2\tilde{u} \left(\frac{\tilde{C}_x}{3} f_2 + \tilde{D} \right) - \frac{\tilde{C}_y}{\phi} \nu_x \tilde{w} f_1 + \tilde{D} \left[2\tilde{w} \tilde{w} - (\tilde{q}_s + 2\tilde{q}_t) \frac{1}{3} \cos(\pi \tilde{x}) \right] \\ & + \tilde{C}_x \left[\frac{1}{2} \tilde{w} \tilde{w} f_4 - \frac{\pi}{30} (\tilde{q}_s f_3 + 4\tilde{q}_t f_8) \cos(\pi \tilde{x}) \right] \\ & + \tilde{G} \left[\tilde{w} f_1 + \frac{4}{3\pi \phi} f_{10} (\tilde{q}_s - \tilde{q}_t) \cos(\pi \tilde{x}) - \frac{2\tilde{u}}{\phi} f_1 \right] = 0 \end{aligned} \quad (\text{A.15})$$

$$\begin{aligned}
 & \frac{8}{15} \tilde{G}(\tilde{q}_s - \tilde{q}_t) f_{11} + \frac{\tilde{q}_s \pi^2}{\phi} - \tilde{q}_s \tilde{G} \tilde{P} + \frac{\phi \pi^2}{1260} \left[70 \tilde{D}(\tilde{q}_s + 2\tilde{q}_t) + \tilde{C}_x(5\tilde{q}_s f_6 + 16\tilde{q}_t f_7) \right] \\
 & - \int_0^L \left[\frac{\phi \pi^2}{3} \left(\frac{\tilde{C}_x}{10} f_3 + \tilde{D} \right) \sin(\pi \tilde{x}) \left(\tilde{u} + \frac{\tilde{w}^2}{2} \right) - \frac{2\phi \pi}{3} \tilde{G} \cos(\pi \tilde{x}) \left(\tilde{w} - \frac{2\tilde{u}}{\phi} \right) f_{10} \right] dx = 0
 \end{aligned} \tag{A.16}$$

$$\begin{aligned}
 & \frac{8\tilde{G}}{15}(\tilde{q}_t - \tilde{q}_s) f_{11} + \phi \pi^2 \left[\frac{\tilde{D}}{9}(\tilde{q}_s + 2\tilde{q}_t) + \frac{\tilde{C}_x}{315}(4\tilde{q}_s f_7 + 17\tilde{q}_t f_9) \right] \\
 & - \int_0^L \left[\left(\frac{\tilde{D}}{3} + \frac{\tilde{C}_x}{15} f_8 \right) \phi \pi^2 \sin(\pi \tilde{x}) (2\tilde{u} + \tilde{w}^2) + \frac{2\phi \pi}{3} \tilde{G} \cos(\pi \tilde{x}) \left(\tilde{w} - \frac{2\tilde{u}}{\phi} \right) f_{10} \right] dx = 0
 \end{aligned} \tag{A.17}$$

$$\begin{aligned}
 & \Delta \left(2\tilde{D} + \tilde{C}_x f_1 - \nu_x^2 \tilde{C}_y f_1 \right) - \tilde{G} \tilde{P} \phi \\
 & - \int_0^L \left[\tilde{D} (2\tilde{u} + \tilde{w}^2) + \frac{1}{2} (\tilde{C}_x - \nu_x^2 \tilde{C}_y) \left(\tilde{u} f_1 + \frac{\tilde{w}^2}{3} f_2 \right) \right] dx = 0
 \end{aligned} \tag{A.18}$$

References

- Agusti, G. (1964). *Some problems in structural instability with special reference to beam of I-section.*, PhD thesis, University of Cambridge.
- Allen, H. G. (1969). *Analysis and design of structural sandwich panels*, Pergamon, Oxford.
- Amanda, S., Ichikawa, Y., Munekata, T., Nagase, V., and Shimizu, H. (1997). “Fiber texture and mechanical graded structure of bamboo..” *Composites Part B*, 28B, 13–20.
- Anderson, T. (2003). “A 3-d elasticity solution for a sandwich composite with functionally graded core subjected to transverse loading by rigid sphere..” *Composite Structures*, 60(3), 265 – 274.
- ANSYS, I. (2019). “Release 19.0 documentation.”.
- Apetre, N., Sankar, A., and Ambur, D. (2008). “Analytical modeling of sandwich beams with functionally graded core..” *Journal of Sandwich Structures & Materials*, 10(53), 53–74.
- Ashby, M. F. (1999). *Materials selection in mechanical design.*, Butterworth-Heinemann, Oxford.
- Ashby, M. (2006). “The properties of foams and lattices..” *Philosophical Transactions of the Royal Society A*, 364, 15–30.

- Ávila, A. (2007). “Failure mode investigation of sandwich beams with functionally graded core..” *Composite Structures*, 81(3), 323–330.
- Bannink, E., Hadcock, R., and Forsch, H. (1978). “Advance design composite material aircraft study..” *J. Aircraft*, 15(10), 661 – 669.
- Bao, L., Miura, Y., and Kemmochi, K. (2018). “Improving bending characteristics of frp sandwich structures with reinforcement webs..” *Advanced Composite Materials*, 27(2), 221 – 233.
- Bazant, Z. P. and Cedolin, L. (2010). *Stability of structures: Elastic, inelastic, fracture and damage theories.*, World Scientific., USA.
- Belytschko, T., Liu, W., and Moran, B. (2000). *Nonlinear finite elements for continua and structures*, Wiley, Chichester.
- Berggreen, C., Branner, K., Jensen, J. F., and Schultz, J. P. (2007). “Application and analysis of sandwich elements in the primary structure of large wind turbine blades..” *Journal of Sandwich Structures & Materials*, 9, 525 – 552.
- Birman, V. and Kardomateas, G. A. (2018). “Review of current trends in research and applications of sandwich structures..” *Composites Part B: Engineering*, 142, 221–240.
- Bowerman, H., Coyle, N., and Chapman, J. C. (2002). “An innovative steel/concrete construction system..” *The Structural Engineer*, 20(20), 33 – 38.
- Brischetto, S. (2009). “Classical and mixed advanced models for sandwich plates embedding functionally graded cores..” *Journal of Mechanics of Materials and Structures*, 4(1), 13–33.
- Brøndsted, P., Lilholt, H., and Lystrup, A. (2005). “Composite materials for

- wind power turbine blades.” *Annual Review of Materials Research*, 35(1), 505 – 538.
- Carrera, S., Brichetto, S., and Robaldo, A. (2008). “Variable kinematic model for the analysis of functionally graded material plates.” *AIAA Journal*, 46(1), 194–203.
- Cherniaev, A. and Telichev, I. (2017). “Weight-efficiency of conventional shielding systems in protecting unmanned spacecraft from orbital debris.” *Journal Spacecraft Rockets*, 54, 75 – 89.
- Cho, K., Bert, C., and Striz, A. (1991). “Free vibrations of laminated rectangular plates analyzed by higher order individual-layer theory.” *Journal of Sound and Vibration*, 145(3), 429–442.
- Chróscielewski, J., Miśkiewicz, M., Pyrzowski, L., and et al (2017). “A novel sandwich footbridge – practical application of laminated composites in bridge design and in situ measurements of static response.” *Composites Part B: Engineering*, 126, 153 – 161.
- Cook, D., Malkus, S. D., Plesha, E. M., and Witt, J. R. (2002). *Concepts and applications of finite element analysis.*, John Wiley & Sons, INC, USA, fourth edition.
- Crisfiels, A. M. and Wills, J. (1988). “Solution strategies and softening materials.” *Computer Methods in Applied Mechanics and Engineering*, 66(3), 267–289.
- Crisfiels, A. M. (1981). “A fast incremental / iterative solution procedure that handles snap trough.” *Computer and Structures*, 13, 55–62.
- Da Silva, L. S. and Hunt, G. W. (1990). “Interactive buckling in sandwich structures with core orthotropy.” *Mechanics of Structures and Machines*, 18(3), 353–372.

- de Boor, C. and Swartz, B. (1973). “Collocation at gaussian points..” *SIAM Journal on Numerical Analysis*, 10, 582 – 606.
- Doedel, E. J., Oldeman, B. E., et al. (2012). “Auto-07p: Continuation and bifurcation software for ordinary differential equations.” Department of computer science , Concordia University, Montreal, Canada. (Available by FTP from ftp.cs.concordia.ca in pub/doedel/auto).
- El-Hadek, M. and Tippur, H. (2003). “Dynamic fracture parameters and constraint effects in functionally graded syntactic epoxy foams..” *International Journal of Solids Structures*, 97, 1885–1906.
- Euler, L. (1744). “Methodus inveniendi lineas curvas maximi minimive proprietate gaudentes..” *Chap. Appendix: De curvis elasticis*.
- Fagerberg, L. (2004). “Wrinkling and compression failure transition in sandwich panels..” *Journal of Sandwich Structures and Materials*, 6(2), 129–144.
- Feldman, E. and Abudi, J. (1997). “End compression of sandwich columns..” *Composites Part A: Applied Science and Manufacturing*, 33, 353–359.
- Fleck, N. A. and Sridhar, I. (2002). “End compression of sandwich columns..” *Composites-Part A: Applied Science and Manufacturing*, 33(3), 353–359.
- Foo, C., Seah, L., and Chai, G. (2008). “Low-velocity impact failure of aluminium honeycomb sandwich panels..” *Composite Structures*, 85, 20 – 28.
- Fox, C. (1987). *An introduction to the calculus of variations.*, Dover, New York.
- Frostig, Y. and Baruch, M. (1990). “Bending of sandwich beams with transversely flexible core..” *AIAA Journal*, 28(3), 523 – 531.
- Frostig, Y. and Baruch, M. (1993). “High-order buckling analysis of sandwich beams with transversely flexible core..” *Journal of Engineering Mechanics*, 119(3), 476 – 495.

- Frostig, Y., Baruch, M., Vilnay, O., and Sheinman, I. (1992). “A high order theory for the bending of sandwich beams with flexible core..” *ASCE Journal of Engineering Mechanics*, 118(5), 1026–1043.
- Frostig, Y. (1992). “Behavior of delaminated sandwich beam with transversely flexible core - high order theory..” *Composite Structures*, 20(1), 1–16.
- Fukui, Y. (1991). “Fundamental investigation of functionally graded materials manufacturing system using centrifugal force..” *JSME International Journal Series III*, 34(1), 144–148.
- Garg, A., Belarbi, M. O., Chalak, H., and Chakrabarti, A. (2021). “A review of the analysis of sandwich fgm structures..” *Composite Structures*, 258, 113427.
- Gattas, J. and You, Z. (2015). “Geometric assembly of rigidfoldable morphing sandwich structures..” *Engineering Structures*, 94, 149 – 159.
- Georgiou, C. and Yiatros, S. (2021). “Advances in nonlinear buckling mode interaction modelling for sandwich struts with functionally graded cores.”.
- Glendinning, P. (1994). *Stability, instability and chaos: An introduction to the theory of nonlinear differential equations.*, Cambridge Texts in Applied Mathematics., Cambridge: Cambridge University Press.
- Goodier, J. N. and Hsu, C. S. (1954). “Nonsinusoidal buckling modes of sandwich plates..” *AIAA Journal*, 21(8), 525–523.
- Goodier, J. N. and Neou, I. M. (1951). “The evolution of theoretical critical compression in sandwich plates..” *J. Aeronaut. Sci.*, 18, 649–656.
- Goodier, J. N. (1946). “Cylindrical buckling of sandwich plates..” *ASME Journal of Applied Mechanics*, 13(4), A253–A260.
- Herman, A. S., Zahlen, P., and Zuardy, I. (2005). “Sandwich structures technology in commercial aviation..” *Thomsen, O.T., Bozhevolnaya, E., and*

-
- Lyckegaard, A. (eds), Sandwich structures 7: Advancing with sandwich structures and materials*, pages 13 – 26.
- Hexcel (1989). “Mechanical properties of hexcel honeycomb material..” Tech. rept. TSB120, HEXCEL.
- Hunt, G. W. and Da Silva, L. S. (1990). “Interactive bending behaviour of sandwich beams..” *ASME Journal of Applied Mechanics*, 57(1), 189–196.
- Hunt, G. W. and Wadee, M. A. (1998). “Localization and mode interaction in sandwich structures.” *Proceedings of the Royal Society A*, 454, 1197–1216.
- Hunt, G. W., Da Silva, L. S., and Manzacchi, G. M. E. (1988). “Interactive buckling in sandwich structures.” *Proceedings of the Royal Society A*, 417 (1852), 155–177.
- Hunt, G. W., Bolt, H. M., and Thompson, J. (1989). “Structural localization phenomena and the dynamical phase-space analogy..” *Proceedings of the Royal Society A*, 425, 245–267.
- Hunt, G., Peletier, M., Champneys, A., Woods, P., Wadee, M., Budd, C., and et al. (2000). “Cellular buckling in long structures..” *Nonlinear Dynamics*, 21(1), 3 – 29.
- Hunt, G. W. (1986). “Hidden (a)symmetries of elastic and plastic bifurcation..” *Applied Mechanics Reviews*, 39(8), 1165–1186.
- Hutchinson, J. W. and Koiter, W. T. (1970). “Postbuckling theory.” *Applied Mechanics Reviews*, 23, 1353–1366.
- Javaheri, R. and Eslami, M. (2002). “Thermal buckling of functionally graded plates..” *AIAA Journal*, 40(1), 162–169.
- Jha, D., Kant, T., and Singh, R. (2013). “A critical review of recent research on functionally graded plates..” *Composite Structures*, 96, 833 – 849.

- Karlsson, K. F. and Åström, B. T. (1997). “Manufacturing and applications of sandwich components.” *Composites Part A: Applied Science and Manufacturing*, 28(2), 97 – 111.
- Ke, L., Yang, J., and Kitipornchai, S. (2009). “Postbuckling analysis of edge cracked functionally graded timoshenko beams end shortening..” *Composite Structures*, 90, 152–160.
- Keller, H. (1977). *Numerical solution of bifurcation and nonlinear eigenvalue problems.*, Academic Press Inc., New York, USA.
- Kim, B. and Christensen, R. (2000). “Basic two-dimensional core types for sandwich structures..” *International Journal of Mechanical Sciences*, 42, 657 – 676.
- Kim, S. and Shridharan, S. (2005). “Analytical study of bifurcation and nonlinear behavior of sandwich columns.” *ASCE Journal of Engineering Mechanics*, 131(12), 1313–1321.
- Koizumi, M. (1997). “Fgm activities in japan.” *Composites Part B: Engineering*, 28B, 1–4.
- Kong, C., Nam, G., Jang, Y., and et.al (2014). “Experimental strength of composite sandwich panels with cores made of aluminium honeycomb and foam..” *Advanced Composite Materials*, 23(1), 43 – 52.
- Le Grogneq, P. and Saoud, K. (2015). “Elastoplastic buckling and post-buckling analysis of sandwich columns.” *International Journal of Non-Linear Mechanics*, 72, 67 – 79.
- Lee, C., Wei, X., Kysar, J. W., and Hone, J. (2008). “Measurement of the elastic properties and intrinsic strength of monolayer graphene.” *Science*, 321(5887), 385–388.

- Léotoing, L., Drapier, S., and Vautrin, A. (2002). “First applications of novel unified model for global and local buckling of sandwich columns..” *European Journal of Mechanics, A/Solids*, 21(4), 683–701.
- Léotoing, L., Drapier, S., and Vautrin, A. (2004). “Using new closed-form solutions to set up design rules and numerical investigations for global and local buckling of sandwich beams.” *Journal of Sandwich Structures and Materials*, 6(3), 263–289.
- Li, C. and Weng, G. (2002). “Antiplane crack problem in functionally graded piezoelectric materials..” *Journal of Applied Mechanics*, 69(4), 481–488.
- Liu, T., Hou, S., Nguyen, X., and et.al (2017). “Energy absorption characteristics of sandwich structures with composite sheets and bio cocounut core..” *Composites Part B: Engineering*, 114, 328 – 338.
- Marsh, G. (2005). “Airframers exploit composites in battle for supremacy..” *Reinforced Plastics*, 49(3), 26 – 32.
- Narayanan, R., Roberts, T. M., and Naji, F. J. (1994). “Design guide for steel-concrete-steel sandwich construction—volume 1..” Tech. rept. Steel Construction Institute, Ascot, Berkshire.
- Niu, K. and Talreja, R. (1999). “Modeling of wrinkling in sandwich panels under compression..” *Journal of Engineering Mechanics*, 125(8), 875–883.
- Noor, A., Burton, W. S., and Bert, C. (1996). “Computational models for sandwich panels and shells..” *Applied Mechanics Reviews*, 49, 155 – 199.
- Norlin, P. and Reutelöv, S. (2002). “The role of sandwich composites inturbine blades..” *Reinforced Plastics*, 46(3), 32 – 34.
- Østergaard, R. C. (2008). “Buckling driven debonding in sandwich columns..” *International Journal of Solids and Structures*, 45, 1264 – 1282.

- Park, J. and Kim, J. H. (2006). “Thermal postbuckling and vibration analyses of functionally graded plates..” *Journal of Sound and Vibration*, 289(1-2), 77–93.
- Plantema, F. J. (1966). *Sandwich construction: the bending and buckling of sandwich beams, plates, and shells.*, Wiley, New York.
- Prabhu, G., Katakam, V., Shankar, S., and et. al. (2019). “Uniaxial tensile failure of multi-core asymmetric sandwich composite structures with bonded repair..” *Composite Structures*, 224, 111025.
- Quanjin, M., Rejab, M., Siregar, J., and Zhongwei, G. (2021). “A review of the recent trends on core structures and impact response of sandwich panels..” *Journal of Composite Materials*, 55(18), 2513 – 2555.
- Rayjade, G. and Rao, G. (2015). “Study of composite sandwich structure and bending characteristics..” *International Journal of Current Engineering and Technology*, 5, 797 – 802.
- Reddy, J. N. (1984). “A simple higher order theory for laminated composite plates.” *Journal of Applied Mechanics*, 51, 745–752.
- Reddy, J. N. (1990). “A general non-linear third-order theory of plates with moderate thickness.” *International Journal of Non-Linear Mechanics*, 25(6), 677–686.
- Reissner, E. (1945). “The effects of transverse shear deformation on the bending of elastic plates..” *ASME Journal of Applied Mechanics*, 67, 69–77.
- Reissner, E. (1948). “Finite deflections of sandwich plates..” *Journal of Aeronautical Sciences*, 15, 435–440.
- Riks, E. (1972). “The application of newton’s method to the problem of elastic stability..” *Journal of Applied Mechanics*, 39(4), 1060–1065.

- Riks, E. (1979). “An incremental approach to the solution of snapping and buckling problems.” *International journal of solids and structures*, 15(7), 529–551.
- Rozvany, G. (2009). “A critical review of established methods of structural topology optimization..” *Structural and Multidisciplinary Optimization*, 37(3), 217 – 237.
- Samsam Shariat, B. and Eslami, M. (2007). “Buckling of thick functionally graded plates under mechanical and thermal loads..” *Composite Structures*, 78(3), 433–439.
- Samsam Shariat, B., Javaheri, R., and Eslami, M. (2005). “Buckling of imperfect functionally graded plates under in-plane compressive loading..” *Thin-walled structures*, 43, 1020–1036.
- Shen, H. and Li, S. (2008). “Postbuckling of sandwich plates fgm face sheets and temperature-dependent properties..” *Composites Part B: Engineering*, 39, 332–344.
- Sinur, F., Zizza, A., Kuhlmann, U., and Beg, D. (2012). “Buckling interaction of slender plates—experimental and numerical investigations.” *Thin-Walled Structures*, 61, 121–131. Recent research advances on thin-walled structures.
- Skarlatos, D. and Yiatros, S. (2016). “Deformation monitoring of materials under stress in laboratory experiments.” *ISPRS Annals of the Photogrammetry, Remote Sensing and Spatial Information Sciences*, III-5, 35–41.
- Sokolinsky, V. and Frostig, Y. (1999). “Nonlinear behavior of sandwich panels with transversely flexible core..” *AIAA J.*, 37, 1474–1482.
- Suzuki, T., Aoki, T., Ogasawara, T., and et al. (2017). “Nonablative lightweight thermal protection system for mars aerofly by sample collection mission..” *Acta Astronaut.*, 136, 407 – 420.

- Swaminathan, K., Naveenkumar, D., Zenkour, A., and Carrera, E. (2015). “Stress, vibration and buckling analyses of fgm plate - a state-of-the-art review..” *Composite Structures*, 120, 10 – 31.
- Tabatabaiefar, H., Mansoury, B., Khadivi Zand, M., and et al. (2017). “Mechanical properties of sandwich panels constructed from polystyrene/cement mixed cores and thin cement sheet facings..” *Journal of Sandwich Structures & Materials*, 19, 456 – 481.
- Takeda, N., Minakuchi, S., and Okabe, Y. (2007). “Smart composite sandwich structures for future aerospace application-damage detection and suppression: a review..” *Journal of Solid Mechanics and Materials Engineering*, 1, 3 – 17.
- Thompson, J. M. T. and Hunt, G. W. (1973). *A general theory of elastic stability*, Wiley, London.
- Timoshenko, P. S. and Gere, J. (1961). *Theory of elastic stability.*, USA: McGraw-Hill.
- Timoshenko, P. S. and Woinowsky-Krieger, S. (1959). *Theory of Plates and Shells*, McGraw-Hill Book Company, Inc.
- Venkataraman, S. and Sankar, B. (2003). “Elasticity solution for stresses in a sandwich beam with functionally graded core..” *AIAA Journal*, 41(12), 2501–2505.
- Vignjevic, R., Campbell, J., Hughes, K., and et al. (2019). “Soft body impact resistance of composite foam core sandwich panels with unidirectional corrugated and tubular reinforcements..” *International Journal of Impact Engineering*, 132, 103320.
- Vinson, R. J. (1999). *The Behavior of Sandwich Structures of Isotropic and Composite Materials*, Technomic Publishing, USA.

- Vinson, J. (2001). “Sandwich structures..” *Applied Mechanics Reviews*, 54, 201 – 214.
- Vinson, J. R. (2005). “Sandwich structures: past, present, and future.” In *Sandwich structures 7: advancing with sandwich structures and materials*, pages 3–12, Springer.
- Wadee, M. and Bai, L. (2014). “Cellular buckling in i-section struts..” *Thin-Walled Structures*, 81, 89 – 100.
- Wadee, M. and Farsi, M. (2014). “Cellular buckling in stiffened plates..” *Proceedings of the Royal Society A*, 470, 20140094.
- Wadee, M. and Garden, L. (2012). “Cellular buckling from mode interaction in i-beams under uniform bending..” *Proceedings of the Royal Society A*, 468(2137), 245 – 268.
- Wadee, M. A. and Hunt, W. G. (1998). “Interactively induced localized buckling in sandwich structures with core orthotropy.” *Journal of Applied Mechanics*, 65, 523–528.
- Wadee, M. A., Yiatros, S., and Theofanous, M. (2010). “Comparative studies of localized buckling in sandwich structures with different core bending models.” *International Journal of Non-Linear Mechanics*, 45(2), 111–120.
- Wadee, M. A. (1999). “Experimental evaluation of interactive buckle localization in compression sandwich panels.” *Journal of Sandwich Structures & Materials*, 1(3), 230–254.
- Wadee, M. A. (2000). “Effects of periodic and localized imperfections on struts on nonlinear foundations and compression sandwich panels..” *International Journal of Solids and Structures*, 37(8), 1191–11209.
- Wadee, M. A. (2007). “Nonlinear mathematics in structural engineering.” *Mathematics Today*, 43, 104–108.

- Williams, D., Leggett, D., and Hopkins, H. (1941). “Flat sandwich panels under compressive end loads, aeronautical research committee reports and memoranda no. 1987..” Tech. Rep., Ministry of Aircraft Production, London.
- Xiong, J., Du, Y., Mousanezhad, D., and et al. (2019). “Sandwich structures with prismatic and foam cores: a review..” *Advanced Engineering Materials*, 21, 1800036.
- Yang, J., Liew, K. M., and Kitipornchai, S. (2006). “Imperfection sensitivity of the post-buckling behavior of high order shear deformable functionally graded plates..” *International Journal of Solids and Structures*, 43, 5247–5266.
- Yiatros, S. and Wadee, M. A. (2011). “Interactive buckling in sandwich beam-columns.” *IMA Journal of Applied Mathematics*, 76, 146–168.
- Yiatros, S., Wadee, M. A., and Völlmecke, C. (2013). “Modelling of interactive buckling in sandwich struts with functionally graded cores.” *Journal of Engineering Mechanics-ASCE*, 139, 952–960.
- Yiatros, S., Marangos, O., Wadee, M. A., and Georgiou, C. (2015). “Localized buckling in sandwich struts with inhomogeneous deformations in both face plates..” *Composite Structures*, 133, 630–641.
- Zenkert, D. (1995). *An Introduction to Sandwich Construction*, Engineering Materials Advisory Services Ltd, London.
- Zenkour, A. (2005). “A comprehensive analysis of functionally graded sandwich plate: Part 1-deflection and stresses..” *International Journal of Solids and Structures*, 42(18-19), 5224–5242.
- Zhang, X., Zhou, H., Shi, W., and et al. (2018). “Vibration tests of 3d printed satellite structure made of lattice sandwich panels..” *AIAA Journal*, 56, 4213–4217.

Zhu, H. and Sankar, B. (2007). “Analysis of sandwich tps panel with functionally graded foam core by galerkin method..” *Composite Structures*, 77(3), 280–287.

Zhu, F., Lu, G., Ruan, D., and Wang, Z. (2010). “Plastic deformation, failure and energy absorption of sandwich structures with metallic cellular cores..” *International Journal of Protective Structures*, 1, 507–541.

Zhu, L., Li, N., and Childs, P. (2018). “Light-weighting in aerospace component and system design..” *Propulsion and Power Research*, 7, 103 – 119.